Tuning of granulopoietic signaling by *de novo* designed agonists

Timo Ullrich[1,5], Christoph Pollmann[2], Malte Ritter[3], Jérémy Haaf[3], Narges Aghaallaei[3,4], Ivan Tesakov[3], Maya El-Riz[2], Kateryna Maksymenko[1,5], Valeriia Hatskovska[1,3], Sergey Kandabarau[3], Maksim Klimiankou[3], Claudia Lengerke[3], Karl Welte[3,7], Birte Hernandez-Alvarez[1], Patrick Müller[5,6], Andrei Lupas[1], Jacob Piehler[2], Julia Skokowa[3,*,#], Mohammad ElGamacy[1,3,*,#]

[1] Max Planck Institute for Biology, Department Protein Evolution, 72076 Tübingen, Germany
[2] Department of Biology/Chemistry and Center for Cellular Nanoanalytics, Osnabrück University, 49076 Osnabrück, Germany
[3] Internal Medicine II, University Hospital Tübingen, 72076 Tübingen, Germany
[4] Present address: Ludwig Boltzmann Institute for Hematology and Oncology, Medical University of Vienna, 1090 Vienna, Austria
[5] Friedrich Miescher Laboratory of the Max Planck Society, 72076 Tübingen, Germany
[6] Present address: Systems Biology of Development and Disease, University of Konstanz, 78464 Konstanz, Germany
[7] University Children's Hospital Tübingen, 72076 Tübingen, Germany
*equal contribution as senior authors
#corresponding authors: julia.skokowa@med.uni-tuebingen.de, mohammad.elgamacy@med.uni-tuebingen.de

Graphical abstract

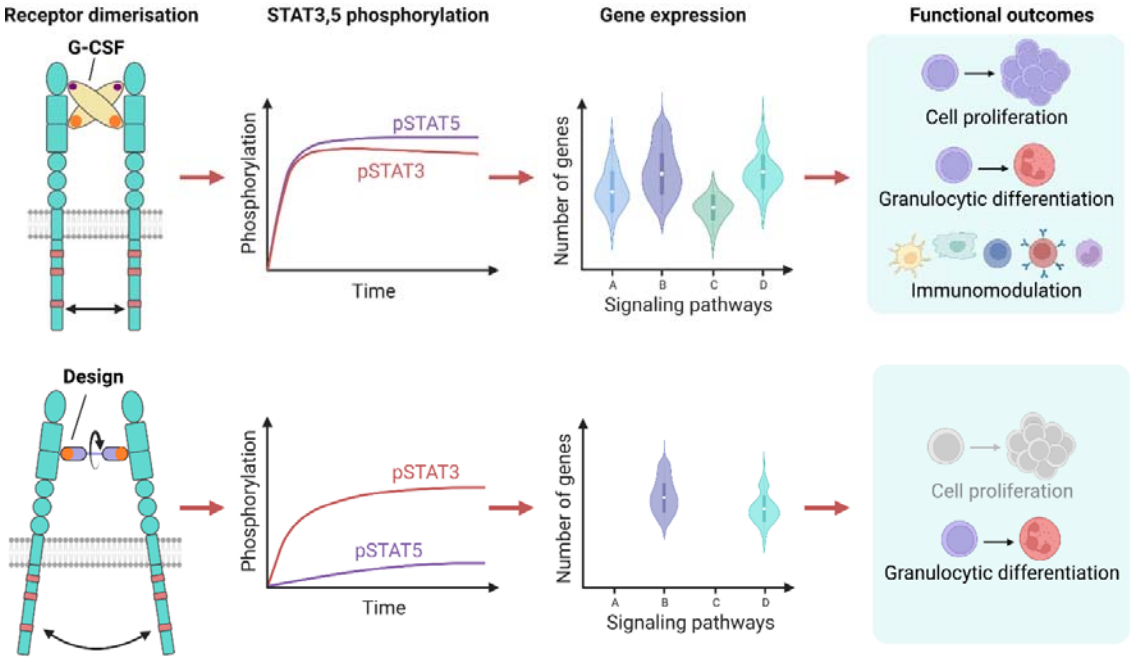

Abstract

Enhancing the efficacy of cytokine-based therapies by systematically tuning how an agonist associates its receptor is emerging as a powerful new concept in drug discovery. *De novo* protein design can serve an excellent tool for tailoring novel cytokine receptor agonists with altered binding affinities and geometries. Here, we report the design and characterization of agonists that tune the granulocyte-colony stimulating factor receptor (G-CSFR) activity, which is central for the proliferation and granulocytic differentiation of hematopoietic stem cells. Selected design agonists were deployed to study the impact of varying the binding affinity and dimerization geometry on receptor association, downstream signaling, and cellular response. Hence, we achieved design agonists with altered signaling specificities that are hyper-thermostable, engage the receptor with tight affinity, and bias granulopoietic differentiation over triggering proliferation. Furthermore, the design agonists modulate the kinetics and amplitudes of signal transduction pathways, yielding differential gene expression patterns. Thus, unlike G-CSF, the design agonists could achieve selective activation of hematopoietic stem cell functions with minimal undesired immunomodulatory effects. These findings demonstrate the potential of dissecting the complexity of G-CSFR signaling, outcompeting the native ligand, and therefore open ways for more specific therapeutic applications.

Introduction

Cytokines are secreted growth factors that canonically function by associating with the ectodomains of their cognate receptor subunits, which leads to the activation of downstream signaling pathways that steer the fate and function of hematopoietic or immune cells [1, 2]. Receptor activation by its native cytokine ligand triggers a complex pattern of different signaling pathways that results in different cellular responses depending on the type and stage of the target cell [3, 4]. Synthetic ligands, purpose-built to engage the cytokine receptors in non-native ways, provide ideal tools to selectively bias these signaling outcomes [5]. Such approaches have proven particularly attractive for the class I/II cytokine receptor families, which signal via non-covalently associated Janus family tyrosine kinases (JAKs). These receptors must dimerize for activating downstream signal activation, which is most prominently mediated by signal transducer and activators of transcription (STAT) proteins [6-9]. Controlling activation of class I/II cytokine receptors is of considerable interest for therapeutic intervention, yet hampered by the often broad and pleiotropic responses [10]. Decomposing these signaling outcomes can unlock previously untapped therapeutic outcomes and applications of cytokine receptor agonists [11].

Cases of differential cytokine receptor signaling by natural ligands [12] have inspired efforts to systematically bias signaling specificity by steering receptor dimerization with design agonists [11]. These ligands can be further engineered to possess optimal pharmaceutical properties, offering a means to reversible, extracellular correction of pathologic cellular behavior, or enhanced activity in physiological settings [11, 13]. For instance, engineered ligands with enhanced binding affinity to the IL-2R β-subunit and attenuated affinities to the γ-subunit induce immunomodulatory outcomes distinct from the native ligands (i.e. IL-2) while outcompeting endogenous IL-2 [14]. Another notable study reported the affinity-engineering of IL-22-mimetics that not only could induce altered intracellular signaling but also exhibited altered tissue-targeting specificity compared to the native ligand [15]. These examples and others highlight the effect of the ligand's receptor-binding affinity on various aspects of complex association and signaling [16, 17]. In addition to affinity, the receptors' association geometry can provide another layer of control over downstream signaling [18-21]. Only recently, ligand-based tuning of cytokine receptors has been demonstrated for three receptor types. Specifically, diabodies and DARPins dimerizing the erythropoietin receptor (EPOR) in diverse, non-native orientations could induce a range of graded or differential signaling through different association geometries [22, 23]. Using bispecific variable antibody fragment fusions (i.e. VHH or scFv), signal tuning or decomposition could be demonstrated for heterodimeric receptor complexes of the IL-2 receptor (IL-2Rβ:γ_c) and the type I interferon receptor (IFNAR1:IFNAR2) [24].

In this study, we aim to explore the possibility of tuning signaling via designed agonists of the granulocyte-colony stimulating factor receptor (G-CSFR), which has not been investigated to date. The granulocyte-colony stimulating factor (G-CSF) induces downstream signaling by homodimerizing its cognate receptor (G-CSFR) in a 2:2 cross-over assembly [2, 25-30]. This signaling is a crucial driver of granulopoiesis and plays diverse roles on hematopoietic stem cells, more mature myeloid progenitors, and mature immune cells, primarily acting on proliferation, differentiation, and mobilization of stem cells, but also regulating the functions of immune cells [31]. The therapeutic importance of G-CSF has thus led to the wide adoption of its recombinant human form, rhG-CSF, in the clinic for treating acquired or congenital neutropenia, in addition to the mobilization of hematopoietic stem cells for transplantation [32, 33]. The therapeutic application of rhG-CSF is however still limited since G-CSFR is also expressed in several subtypes of immune cells, osteoclasts and tumor cells. Inducing specific, e.g., granulopoietic, activity of G-CSF while suppressing its unintended action on cell proliferation and activation of immune cells, osteoclasts or cancer cells can broaden its clinical use. To achieve this, we must distinguish between signal transduction pathways that trigger differentiation over proliferation or immune cell activation. The key effectors of G-CSFR signaling are STAT3 and STAT5 proteins [34], among others. STATs are

activated by tyrosine phosphorylation (pSTAT) through Janus Kinase 2 (JAK2) upon G-CSFR dimerization whereby STAT3 phosphorylation occurs at the membrane-distal regions of the intracellular segments of the receptor [35]. At the same time, STAT5 is phosphorylated at the membrane-proximal receptor region. The sequential activation of STAT3 and STAT5 may dictate their functional outcomes where pSTAT3 mostly transduces differentiation signals to the cell while retaining some proliferative activity, and pSTAT5 predominantly induces proliferation [36-39]. The balance between STAT3 and STAT5 phosphorylation is decisive for cellular outcomes upon G-CSF stimulation [40, 41]. Thus, by dissecting the activation kinetics of STAT3 and STAT5, specific G-CSF activity might be achieved.

Leveraging these differences in STAT3/STAT5 recruitment and activation, we here aimed to systematically bias pSTAT3/pSTAT5 kinetics and amplitudes by designing G-CSFR agonists with altered receptor orientations in the signaling complex. We achieved this by focusing on highly optimized G-CSFR binding modules, which were subsequently harnessed to design G-CSFR agonists imposing diverse receptor orientations. Based on characterizing their biophysical properties and investigating their impact on receptor dimerization in the plasma membrane, in conjunction with intracellular signal activation, and cellular activation *in vitro* and *in vivo*, we highlight the potential to tune G-CSFR signaling towards differentiation, while avoiding its undesired non-hematopoietic effects.

Results

Computationally-guided screening identifies higher-affinity G-CSFR binders

G-CSF dimerizes G-CSFR in a 2:2 stoichiometry with each ligand cross-linking the two receptor subunits by binding via high and low affinity binding sites in a reciprocal manner (Fig. 1A). Previously, we have designed an artificial ligand *de novo*, Boskar4, that encodes one G-CSFR-binding site. When two copies of Boskar4 were tandemly linked by a short flexible linker (i.e. Boskar4 short tandem of 2 domains; B4_st2), it could dimerize and activate G-CSFR (Fig. 1B) [42]. G-CSF engages G-CSFR through its two high- and low-affinity binding sites; site II and site III (located on the ligand) the CRH and Ig-Like domains of the receptor, respectively. In contrast, Boskar4 encodes only the high-affinity binding site (a site II-like epitope) that engages the CRH domain through a relatively large interface surface area (Fig. 1C).

We first sought to enhance the receptor-binding affinity of Boskar4 (Fig. 1D), with the dual aim of achieving more efficient receptor dimerizers (Fig. 1E), and evaluating the impact of affinity change on receptor signaling. Hence, we needed to design additional mutations at the Boskar4:G-CSFR binding interface in order to improve its binding affinity. We thus modelled the Boskar4:G-CSFR complex (Fig. 1C) using all conformations from our previously compiled NMR ensemble (PDB: 7NY0). These models were used as input for the multi-model, single-point mutagenesis application from the Damietta protein design software [43]. We set six amino acid positions on the Boskar4 surface as mutation target sites at the binding interface with G-CSFR (Fig. S1A), which were selected based on their proximity to the G-CSFR surface, while avoiding previously described critical binding residues [44]. We included the top five mutations at each position with the joint lowest energy at the binding interface across all models (as well as wild-type identities) for library generation. Finally, we built two site-directed mutagenesis libraries based on either the designed sequences or site-saturation mutagenesis (as a random control) of the same positions (Fig. S1C, D). The control library contained on average 12 mutations per position, in contrast to an average of 6 mutations per position for the designed library. The resulting amino acid diversity of the designed library was 3.9×10^4 and a final diversity of 2.3×10^5 variants after PCR mutagenesis, in comparison to the saturation library, which encompassed 3.1×10^6 variants. We used a bacterial display screening system [45] in which the ligand is presented as an extracellular Intimin fusion on the surface of the bacterial particles. Upon adding fluorescently-labelled G-CSFR, we sorted the bacterial particles for receptor binding using

fluorescence-activated sorting (FACS) (Materials and Methods). We ran both libraries (saturation and designed) through five cycles of FACS enrichment under the same conditions, where shifts in the fluorescence of both populations were observed across the enrichment cycles (Fig. 2A). Forty-eight single clones were picked from either library after the third and fifth FACS cycles, amounting to a total of 192 clones. Using on-plate fluorescence- and luminescence-based assays we quantified the relative binding of these clones to the receptor under the same conditions (Fig. S2).

The sequences of the top 40 clones picked from both libraries after Sanger sequencing yielded 16 unique Boskar4 variants (Fig. S2D). A focused FACS-based analysis for these ligands' expression level and binding affinity on the surface of *Escherichia coli* (*E. coli)* (Fig. S3) showed the expression-normalized binding affinities to range from 3- to 37-fold increase, when compared to the starting Boskar4 clone. To narrow down the number of candidates for subsequent investigations, while keeping diversity, we chose six variants based on their estimated affinity, frequency in the screen, or the respective mutation composition (Fig. S2D and S3B). The most frequent variant was bv1, while the highest affinity variant was bv2. Four additional variants, bv6, bv8, bv15 and bv16 were chosen based on their middle- or lower- binding affinity profiles. Specifically, variants with polar and charged residues were included with the goal of selecting the most soluble and specific binders.

In order to create efficient G-CSFR agonists, the six selected variants were incorporated into short tandem repeats of two domain copies connected by a G_4S_2 sequence (Fig. S4). The generated st2 variants were readily purified using immobilized metal affinity chromatography (IMAC) from the soluble fraction of *E. coli* cell lysate, where preparative size exclusion chromatography and SDS-PAGE analysis indicated that they have the expected molecular weight of approximately 29 kDa (Fig. S5). Using surface plasmon resonance (SPR), the binding affinity and kinetic parameters of the designs to G-CSFR were obtained. The SPR results showed that all the six tested variants in their tandem form bind to G-CSFR within the sub-nanomolar affinity range, with up to 7-fold enhanced affinity compared to the starting template B4_st2 (S6 and Table 1). The observed affinity improvement was also higher when evaluated for single-domain Boskar4 variants. For instance, the single-domain form of the most biologically active variant (bv6) exhibited a K_D of 14 ± 2 nM, in comparison to the single-domain Boskar4 template, with K_D of 173 ± 43 nM (Fig. 2B, S7B). Notably, circular dichroism (CD) measurements of bv6 showed the expected strong alpha-helical signal, and nanoscale differential scanning fluorimetry (nanoDSF) measurements demonstrated that bv6 exhibited uncompromised thermostability when compared to Boskar4 (Fig. S7C, D).

Affinity enhancement yields highly potent G-CSFR agonists with uncompromised thermostability

Given the tight binding affinities, we expected our bivalent constructs to function as more efficient G-CSFR agonists compared to the not affinity-enhanced designs, which we evaluated using the G-CSF-dependent cell line NFS-60 [46, 47]. These results showed that all of the affinity-enhanced variants were more potent in inducing the proliferation of NFS-60 cells when compared to the starting template (B4_st2). Remarkably, the most active design, bv6_st2 had an EC_{50} of 2.9 ±1.3 pM compared to 33 ±23.6 pM for B4_st2 and 2.6 ±1.8 pM for rhG-CSF (Fig. 2C, S8 and Table 1) while no differences in the maximum response of proliferative activity were noticed (Fig. S8E). The observed difference between the mean EC_{50} values of the most active variant (bv6_st2) and rhG-CSF was statistically insignificant (*p-value* = 0.9). The observed range of affinities and activities of the studied variants showed no strong correlations between the proliferative activity (EC_{50}) and the binding affinity (K_D; $R_{pearson}$ = 0.15), the association rate constant (k_a; $R_{pearson}$ = 0.01), or the dissociation rate constant (k_d; $R_{pearson}$ = 0.12) (Fig. S9). We therefore expect that the activity of variants within this narrow range of affinities might be influenced by other factors such as their relative stabilities and binding specificity in the complex environment of cell culture-based assays, in comparison with SPR-derived affinities which were measured between reconstituted proteins.

To assess the structural stability of our designs, circular dichroism (CD) measurements were performed for all selected variants which showed the expected strong alpha-helical signal (Fig. S10A). Additionally, the thermostability was measured using nanoscale differential scanning fluorimetry (nanoDSF) to inspect if the included mutations destabilized the proteins. Half of the tested variants (bv1_st2, bv6_st2 and bv8_st2) exhibited no detectable melting transitions up to 110 °C, while the other three (bv2_st2, bv15_st2 and bv16_st2) exhibited a melting onset at around 100 °C. No scattering (i.e. precipitation) was observed for any of the proteins over the full temperature range (Fig. S10B-H). Similar results were observed for the single-domain form of the variants, where bv6 displayed tighter receptor-binding affinity compared to the parent single-domain Boskar4, while preserving the hyper-thermostability of the latter (Fig. S7D).

These results indicate, that the affinity-driven functional enhancement did not alter the biophysical properties of the designs, which are far superior to rhG-CSF. Therefore, we further sought to test whether the design agonists exhibit similarly enhanced activity *in vivo*.

Boskar4 variants induce neutrophil production in zebrafish embryos and mice

We tested the effects of two optimized variants, bv6_st2 and bv8_st2 on the induction of granulopoiesis *in vivo* using two model organisms, zebrafish and mice. We used a fluorescent neutrophil reporter zebrafish transgenic line, *Tg(mpx:GFP)* [48], and C57BL/6 mice. For zebrafish experiments, equal volumes of rhG-CSF and Boskar4 variants were injected into the cardinal vein of *Tg(mpx:GFP)* larvae at 1.5 days post-fertilization (dpf). As negative control, Moevan_control (a design protein not capable of binding and activating G-CSFR, but expressed and purified under the same conditions as Boskar4 variants [49]) was injected. Interestingly, the increased number of GFP^+ neutrophils localized near the caudal hematopoietic tissue (tail region) was comparable between larvae treated with rhG-CSF or Boskar4 variants 24 h post-injection (Fig. 2D). The number of neutrophils was almost unchanged in the Moevan_control-injected larvae.

We additionally treated C57BL/6 Ly5.1 mice with 300 μg/kg of rhG-CSF or the two most active Boskar4 variants bv6_st2 and bv8_st2 by intraperitoneal (i.p.) injection every second day with five injections in total. One day after the fifth injection, the number of $Ly6G^+Ly6C^+$ neutrophils and $Ly6G^-Ly6C^+$ monocytes in the bone marrow of treated mice was evaluated. Indeed, treatment of mice with bv6_st2 or bv8_st2 induced the production of neutrophils and monocytes at a comparable level to rhG-CSF (Fig. 2E). These results highlight the ability of optimized Boscar4 variants to potently activate G-CSFR *in vivo*.

Design of agonists altering the relative orientation of G-CSFR

After identifying the most active G-CSFR binders, our next step was to build geometry-tuning agonists to evaluate the sensitivity of G-CSFR signaling to non-native receptor orientations. In order to dimerize G-CSFR subunits at bespoke angles, we sought to create rigidly juxtaposed bv6 modules, where two modules share one continuous common helix (Fig. 1E). By varying the length of an inserted helical segment, and splicing the N-terminal and C-terminal helices of two binding modules, different inter-domain rotations could be modelled (Fig. S11A, B). Using epitope-alignment and AlphaFold2 [50] we modelled the predicted full-length assemblies of resulting 2:1 complexes (Fig. 3A). The templates named ori0 through ori4 (orientation-rigging designs) were initially sculpted with poly-alanine splicing helical segments that were sequence-designed using the combinatorial sampler application of Damietta [43]. We then ran molecular dynamics simulations of the lowest energy candidates in order to validate the putative conformation for each ori design, and estimate the degree of conformational deviation from the AlphaFold2-predicted models (Fig. S11C, D). The oris were predicted to impose discrete distances across the receptor transmembrane domains (TMDs; d_0 = 78 ±32 Å, d_1= 206 ±14 Å, d_2 = 287 ±6 Å, d_3= 155 ±35 Å, and d_4 = 143 ±37 Å, for ori0, ori1, ori2, ori3, and ori4, respectively), whereas the 2:2 native complex (PDB: 2D9Q) model exhibited a relatively short distance of d_g = 57 Å (Fig. 3A, B).

The generated designs ori0-4 were purified from *E. coli* and analyzed by size exclusion chromatography, which confirmed the expected size of around 29 kDa. With the exception of ori1, which showed a clear monomer-dimer equilibrium, all the other designs were purely monomeric in solution (Fig. S12). CD and nanoDSF measurements confirmed the helical secondary structure and the hyperstability of the design agonists, similar to their template, bv6 (Fig. S13). In all cases, no precipitation (increased scattering) was observed for any of the designs over the full temperature course. All the designs bound to G-CSFR as expected, where their apparent binding affinities ranged from 0.44 nM to 0.73 nM (Fig. S14 and Table 1). These values are comparable with those observed for bv6_st2, which exhibits an average K_D of 0.67 nM.

The geometric modulation of the G-CSFR by design agonists differentially affects cell proliferation

The designed geometric modulators possessed varying proliferative activities, as tested in the NFS-60 cell line. The EC_{50} values of these ranged from 36 ±19.8 pM down to 2.8 ± 1.4 pM, and exhibited a reproducible pattern (Table 1 and Fig. S15), being comparable to Boskar4_st2 designs. For ori1, we observed a reduction in the maximum proliferation level (E_{max}) by about 20 %, while no significant differences were observed for all other designs compared to rhG-CSF (Fig. S15H). The proliferative EC_{50} values of these design agonists correlated with the modelled distances across the receptor TMD for these designs (R^2 = 0.92; Fig. 3C). Highest potency was observed for ori0, which dimerizes G-CSFR with a very similar TMD spacing as native G-CSF ($d_0 \approx d_g$). On the other hand, the design agonists inducing the farthest distance between the TMD, ori1 and ori2, showed the lowest potency. While these results clearly underline inter-TMD spacing as a key parameter defining signaling activity, imposing these non-native geometries across two-dimensionally arranged receptors may result in significant conformational strain that reduces for some geometries the effective binding affinity to the cell surface receptor.

Design agonists impose distinct complexes with G-CSFR and can override the native ligand

The above results thus point towards a clear sensitivity of receptor activation towards the differential geometries of the design agonists. These differences stand out despite the fact that the designs (ori0-4) and the flexible tandem (bv6_st2) all share the same binding interface and possess very similar affinity values (Table 1). To query the properties of these complexes in a cellular environment, we explored G-CSFR assembly in the plasma membrane by live cell single-molecule fluorescence imaging. To this end, G-CSFR fused to an N-terminal ALFA-tag was expressed in HeLa cells and labeled selectively at the cell surface by applying a mixture of anti-ALFA nanobodies conjugated with Cy3B and AT643, respectively (Fig. 4A) [51]. Since it has been shown, that associated JAK2 energetically contributes to cytokine receptor complex formation, we additionally transfected JAK2 C-terminally fused to mEGFP [8]. This construct lacks the Tyrosine kinase domain (TK) to ensure that the experiments are not biased by activated downstream pathways while maintaining its contribution to dimerization. Simultaneous dual-color single molecule imaging by total internal reflection fluorescence microscopy enabled identifying individual G-CSFR dimers by co-localization and co-tracking analysis (Supplementary Movie S1, Fig. 4B and S16A). As expected, G-CSFR dimerization was negligible in the resting state, but strongly stimulated by G-CSF and all design agonists (Fig. 4C). While similar dimerization levels were observed for most design agonists, dimerization induced by ori2 and ori3 was significantly lower. Importantly, similar receptor cell surface densities were used in all experiments (Fig. S16B), thus ensuring that dimerization levels were not biased by the two-dimensional (2D) receptor concentration governing agonist-mediated crosslinking of G-CSFR into dimers (cf. Fig. 1A). Since the three-dimensional (3D) binding affinity of all design agonists is identical, the distinct differences in dimerization potencies of different design agonist can be ascribed by different two-dimensional (2D) binding affinity (cf. Fig. 4A). This can be rationalized by changes in the 2D association rate constant k_a^{2D}, but not the complex stability k_d^{2D} due to geometrical constraints imposed by the orientation of the receptor ectodomains at the cell surface. With the formation of 1:1 G-CSFR:agonist complexes competing with G-CSFR dimerization,

reduction in 2D binding affinity is accompanied by a lower maximum of the bell-shaped concentration-dimerization relationship of homomeric dimerizers [52]. Changes in dimerization efficiency can explain differences in the EC_{50} values, as the overall receptor binding affinity depends on dimerization efficiency [53, 54]. Similar effects have been observed for design agonists for geometric control of the EPOR [22, 23]. However, different G-CSFR dimerization levels induced by different design agonists did not directly correlate with their activity. Thus, ori1 showed substantially higher dimerization levels as compared to ori2, yet their NFS-60 proliferation activity was similar. Additionally, ori1 and ori0 had similar dimerization levels, but ori0 had about ten times higher proliferation activity compared to ori1 (Table 1). These results therefore confirm that biased signaling observed for design agonists is related to the altered geometry of the signaling complex rather than weakened dimerization.

We furthermore analyzed the diffusion properties of agonist-induced G-CSFR dimers as compared to unstimulated monomers. Diffusion constants as determined by mean squared displacement analysis were very similar for all G-CSFR dimers independent of the nature of the agonist, showing a decrease by ~45% compared to G-CSFR monomers (Fig. 4D). Similarly, the fraction of immobile G-CSFR increased by a factor of ~2, with ori3 showing surprisingly higher immobilization by a factor of ~3 (Fig. 4E). Receptor immobilization is very likely caused by endocytosis, and therefore differences for different design agonist may indicate changes in endocytic uptake for different design agonists [55]. Effective competition of design agonists with the native ligand was confirmed by co-tracking analysis in the presence of G-CSF and ori2 at equimolar concentrations. Under these conditions, very similarly reduced dimerization levels were observed as for ori2 alone (Fig. 4F and S16C, D). Taken together, these results corroborate that our design agonists potently induce G-CSFR dimerization at the cell surface and that biased signaling can be explained by systematically altered complex geometries.

Different design agonists tune G-CSFR signaling amplitudes, kinetics and cellular response patterns

To pinpoint biased G-CSFR signaling by designed agonists at the level of downstream signal propagation, we quantified the phosphorylation of STAT3 and STAT5 proteins in NFS-60 cells treated with rhG-CSF or designed agonists. Since STAT3 phosphorylation occurs at the membrane-distal regions of the intracellular segments of the receptor , while STAT5 is phosphorylated at the membrane-proximal receptor region [56], we reasoned that the relative ratio of pSTAT3/5 might be altered by different design agonists. We therefore aimed to investigate whether design proteins can affect STATs phosphorylation dependent on the engagement geometry of two G-CSFR receptor subunits. Western blot analysis after stimulating cells for 5 and 30 min confirmed increased phospho-STAT3 (pSTAT3, Tyr705) levels for bv6_st2 as compared to B4_st2, validating that our strategy increases potency by enhancing the affinity (Fig. 5A, C and S17). For the oris, however, striking differences were observed: while after 5 and 30 minutes ori0 and ori2 reached similar pSTAT3 levels and activation kinetics as bv6_st2, markedly lower pSTAT3 levels were found for ori1 for 5 min of stimulation (Fig. S17). As expected, designed proteins showed substantially lower and prolonged STAT5 phosphorylation (pSTAT5, Tyr694) as compared to rhG-CSF (Fig. 5B, D). Again, bv6_st2 and ori0 phosphorylated STAT5 more efficiently than B4_st2, ori2 or ori1, but the magnitude of STAT5 phosphorylation was markedly weaker for all variants, as compared to rhG-CSF. An increase of pSTAT5 levels from 5 min to 30 min stimulation was observed for all design agonists, while pSTAT5 levels remained largely constant upon stimulation with rhG-CSF. These results highlight that amplitudes and kinetics of STAT3 and STAT5 phosphorylation by G-CSFR can be tuned by its dimerization with altered geometry.

G-CSF induces proliferation and granulocytic differentiation of hematopoietic stem cells, and until now it is impossible to dissect these two cellular outcomes intentionally. It has been demonstrated that different magnitudes and kinetics of STAT3 vs STAT5 phosphorylation have different outcomes on hematopoietic stem cell functions, where the shift towards elevated activation of STAT3 triggers

myeloid differentiation, while extensive STAT5 phosphorylation is rather responsible for cell proliferation [57]. Observing different activation kinetics of STAT3 and STAT5 by the designed agonists, we thought to achieve dissociation of proliferation from differentiation outcomes on hematopoietic stem cells. Indeed, as expected, we found that the designed proteins alone failed to trigger proliferation of hematopoietic stem and progenitor cells (HSPCs) compared to G-CSF (Fig. 5E). Proliferative activity of agonists was slightly induced in the presence of hematopoietic cytokines, IL-3 and SCF (Fig. 5F). In line with previous observations, ori0 has the strongest potential, as compared to other designs, but was still weaker, as G-CSF.

However, ori0 was as active as native G-CSF in inducing granulocytic differentiation of HSPCs when combined with IL-3 and SCF - stimulation with ori0 yielded substantially higher levels of granulocyte colony-forming units (CFU-G) in comparison to the flexibly connected bv6_st2 (Fig. 5G). G-CSF and ori0 also had a comparable effect in stimulating granulocyte-macrophages CFUs (CFU-GM) (Fig. 5H). Meanwhile, the other design agonists (ori1, ori2 and bv6_st2) did not significantly induce CFU-Gs in comparison with untreated cells. Interestingly, all the design agonists had a weak effect on the formation of monocytic colonies (CFU-M) (Fig. 5I), suggesting selective activation of granulocytic differentiation by then, when compared to native G-CSF. These results highlight the capacity of the design agonists to specifically induce granulocyte differentiation over the proliferation of HSPCs, with differential potencies.

Taken together, modeling the geometry of G-CSFR agonists allows fine-tuning of STAT3,5 phosphorylation that ultimately results in the dissection of proliferation from granulocytic differentiation of HSPCs.

Designed G-CSFR agonists modulate intracellular transcriptional programs with hematopoietic bias

For a more detailed picture of the intracellular response pattern initiated by different design agonists, we assessed their transcriptomic footprints. We carried out RNA-Seq of NFS-60 cells undergoing 8-h treatment with 1 nM of the selected agonists, thus ensuring saturated response for all variants. In the rhG-CSF group, we identified 1950 differentially expressed genes compared to the PBS-treated control group (log FC 1, FDR less than 0.05). The number of differentially regulated genes was lower (1292 genes) in the group treated with the most active design agonist with the shortest inter-TMD distance, ori0. This number was even lower (524 genes) in the ori2-treated group, the design agonist imposing the longest inter-TMD spacing (Fig. 6A). Stimulation of cells with bv6_st2 led to the differential expression of 1115 genes. Genes differentially regulated by the design agonists overlapped across all design agonists and were clearly subsets of rhG-CSF-regulated genes (Fig. 6B, C). The general trend revealed a gradual decrease in the expression of the regulated genes across the treatment groups, with the order of rhG-CSF > ori0 > bv6_st2 > B4_st2 > ori2 > ori1 > PBS (Fig. 6C and Fig. S18). Gene set enrichment analysis showed similar enrichment patterns, particularly in the regulation of hematopoiesis/myelopoiesis-related gene sets among rhG-CSF and the design agonists (Fig. 6D and Fig. S19). As with individual genes, the degree of regulation of the enriched gene sets was either the same as in the rhG-CSF group, or gradually reduced (Fig. S20).

A closer look at the transcription patterns identified subsets of genes to be either exclusively regulated by rhG-CSF, or by the design agonists (Supplementary data). Thus, rhG-CSF, but not design agonists regulated the expression of genes involved in immunomodulation of T lymphocytes, MDSCs, monocytes/macrophages, dendritic cells and basophils such as IL18R1, Lilrb4, Gp49a, Inhba, Ifitm6, Stfa1, Slfn2, Osm, Ly6i, Il19, Oas1g, Apol9b, Tarm1, Ifit3, CCR5, Trem1, Irg1, NLRRP12, MX2, and IL17c. These data argue for the possible specificity of the designs toward HSPCs. Chemokine receptors, CXCR2, CXCR4, CX3CR1, CCR5 were also regulated by G-CSF, but not design proteins. Additionally, VEGFR/ Kdr, transcription factors HOXA1, HOXB3, Klf3, Junb, MEIS3, Egr1, HOXC4; cell cycle regulators CDKN1A/P21 and CDKL2 and adhesion molecules AMIGO2, Adgre1,

Tns1, Trio, and Pcdhga6, were affected in the rhG-CSF group only. Simultaneously, a small set of genes was regulated by the design agonists, but not by rhG-CSF, with different degrees of regulation between different designs (Fig. 6B). In line with these observations, gene ontology (GO) analysis of signaling pathways showed a gradual reduction of the number of regulated genes in the categories "signaling receptor activity", "molecular transducer activity", "transmembrane signaling receptor activity" with a slight overlap in "immune receptor activity", and "cell adhesion molecule binding" (Fig. 6D).

Discussion

Chimeras of natural cytokines or variable antibody domains have demonstrated the potential of developing new therapeutic approaches by targeting cytokine receptors [24, 58-67]. However, *de novo*-design agonists based on stable protein scaffolds can overcome several shortcomings. First, the compactness of these binding modules allows for constructing functional fusions with smaller increments of molecular weight. Second, starting from a highly stable template gives room for affinity maturation and functional enhancements, which typically erode structural stability [68]. Finally, sufficiently affine binding modules capable of outcompeting the native ligand at its binding site can impose the desired receptor induction mode, allowing it to override the natural cytokine's signaling.

As a proof-of-concept, here we have leveraged the *de novo*-designed G-CSFR binder (Boskar4) [42] to create functionally diverse agonists capable of tuning intracellular signaling and cellular responses. Our goal was to explore agonists that bind and dimerize G-CSFR with varying affinities and geometries inducing specific signaling patterns and thus distinct cellular activity. To ensure efficient dimerization even at non-native receptor orientations, we generated Boskar4 interface mutants with increased G-CSFR affinity by means of computationally-guided screening. Tandemly-linked agonists based on the affinity-optimized Boskar4 showed increased potency in inducing G-CSFR-triggered cell activation *in vitro* and *in vivo*. Despite the order-of-magnitude of enhancement in both affinity and cellular activity, the designs remained hyper-thermostable. In contrast, all previous studies aiming to improve the stability of rhG-CSF have yielded variants with only marginal improvements in biophysical properties [69-71]. This emphasizes the value of developing therapeutics starting from idealized *de novo* templates, which allows for a large room of stability erosion during functional optimization [68]. The high residual stability and the diverse binding site sequences of the described design variants are invaluable for de-risking further optimization to cloak any immune epitopes; an essential step towards clinical development.

This observed affinity-activity relationship for the agonists indicates that more stable ligand:receptor complexes lead to stronger signaling, despite their reliance on a flexible linker. Therefore, we sought to design rigid rotameric fusions (oris) that can probe the geometric determinants of G-CSFR activation. Proliferation assays along with signal transduction evaluations in NFS-60 cells have set forth the inter-TMD spacing of the resulting ori:G-CSFR complexes as a key parameter controlling the overall signaling amplitude. The analysis of the phosphorylation of the main secondary messengers (STAT3 and STAT5) revealed that both, higher affinity, and shorter inter-TMD spacing selectively increase the intracellular level of pSTAT3 while only minimally inducing pSTAT5. This might relate to the different localization and mechanisms by which STAT3 and STAT5 are phosphorylated along the intracellular segment of G-CSFR [37, 56, 72] and the effect of the inter-TMD spacing on the balance between these two processes. Broadly speaking, pSTAT3 primarily guides differentiation, while pSTAT5 mainly drives proliferation [36-39]. Corresponding results were obtained through granulocyte-colony formation assays in primary human HSPCs, where more affine and shorter-spacing designs led to more selective formation of granulocytic colonies, in comparison to G-CSF.

Single molecule fluorescence imaging confirmed the ability of most design agonists to potently dimerize G-CSFR in the plasma membrane of living cells, reaching similarly high levels as observed

for G-CSF. The reduced dimerization levels observed for ori2 and ori3 indicate that manipulating the geometry of G-CSFR dimers is accompanied by a loss of 2D association kinetics. Changes in signaling activity and specificity, however, cannot be attributed to changes in dimerization. These experiments therefore clearly support the idea that design agonists assemble G-CSFR dimers with altered geometry. The very similar diffusion constants of all agonist-induced dimers, however, suggest more subtle changes in orientation as compared to the predicted structures, which should significantly reduce mobility. This could be explained by the additional strain imposed by membrane anchoring and additional interactions involving associated JAKs. Nonetheless, the distinct rise in the immobile fraction observed for ori3 points towards changes in endocytic uptake for that particular agonist. This warrants further investigation, as endocytic trafficking of cytokine receptor signaling complexes is emerging as a complex determinant regulating potency and kinetics of signal activation and the specificity of cellular responses [55, 73, 74]. Indeed, we observe distinctly reduced STAT5 phosphorylation magnitude for the different design agonists, which could be related to altered endocytic trafficking. Therefore, manipulating trafficking kinetics by design agonists may be an additional parameter for biasing cytokine signaling.

By looking at the gene expression footprints induced by various design agonists, we could identify differential degrees of activity on downstream signal transduction pathways. Through our different design:receptor constellations, we observed varying degrees of tuning of the G-CSFR-triggered intracellular signaling activation or inhibition. Moreover, the design agonists minimally affect the expression of genes that are not regulated by rhG-CSF. Thus, we could fine-tune G-CSFR signaling without major unexpected transcriptional outcomes that are not linked to physiological G-CSFR activation. This information is important for at least two aspects – first, it gives significant insights into the signal transduction through G-CSFR using *de novo*-designed agonists. Second, it opens up an entirely new perspective in designing hematopoietic and granulopoietic proteins with specific activity and less undesired functions, when compared to native or recombinant cytokines. To date, designed IL-2 and and IL-4 mimics, that bind a subset of the natural cytokine's heteromeric receptor subunits, could achieve more selective biological responses [75, 76]. Alternatively, ligand-based tuning of homodimeric receptors, could rather be achieved through synthetic agonists with varying affinities and geometries for EPOR [22, 23] and TPOR [77, 78]. These synthetic agonists could impose different modes of receptor regulation, ranging from activation to total inhibition. Our results are first to establish the tunable modulation potential for G-CSFR, opening the way for selective modulation of its hematopoietic and non-hematopoietic functions through the described design strategy. Notably, this strategy may be extended to several other cytokine receptors to fine-tune cellular responses and thus, potentially facilitate novel therapeutic applications.

These findings demonstrate the potential for tailoring G-CSFR agonists to achieve more specific therapies for hematopoietic stem cell disorders, particularly given that G-CSFR activation by rhG-CSF can lead to diverse functional outcomes. The main function of G-CSF is to induce proliferation, migration and myeloid differentiation of hematopoietic stem cells. However, G-CSF can also protect from cell death and have immunomodulatory activity [31, 56, 79, 80]. For instance, rhG-CSF's widest use is to treat neutropenia acquired as a result of cytotoxic anti-cancer therapy [32]. In some cases, rhG-CSF treatment may inadvertently influence cancer treatment by directly activating G-CSFR-expressing tumor cells or dysregulating anti-cancer immune control by G-CSFR-expressing monocytes/macrophages, myeloid-derived suppressor cells (MDSC), T-lymphocyte subsets, dendritic cells or natural killer cells. These outcomes can negatively influence the course of treatment, and motivate the discovery of G-CSFR ligands capable of selective induction of specific granulopoietic signaling on hematopoietic stem cells without affecting proliferation or immune cell functions. The signaling footprint by our design agonists that are triggered by specific observed STAT3/STAT5 phosphorylation kinetics suggests that alteration in the dynamics of STAT phosphorylation can selectively activate hematopoietic and granulopoietic responses with only minimally inducing

proliferation and immunomodulatory side effects. This study thus paves the way for the further development of potent, hyperstable, and selective sub-agonists of G-CSFR.

Material and Methods

Computationally-guided library generation for affinity maturation

Two libraries of mutants of 6 amino acid positions on the Boskar4 receptor-binding sites were generated using either site-saturation mutagenesis or computational design. The mutated positions on the Boskar4 surface were chosen based on two criteria (Fig. S1A). First, the positions in Boskar4 were determined which had the smallest average distance to G-CSFR in a modeled complex between the Boskar4 ensemble (PDB: 7NY0, [42]) and G-CSFR (PBD:2D9Q, [30]). Second, residues known to be critical for G-CSF activity were excluded from the final choice [44]. For the saturation library, high diversity degenerated codons were chosen which contained the original amino acid and other random amino acids constructing a library of a theoretical diversity (number of distinct gene variants) of 4.0×10^6 and an amino-acid diversity (number of distinct protein variants) of 3.2×10^6. Finally, the library was generated by PCR (Table S1 and S2) using one pair of primers (primer 3 and 4), each containing 3 degenerated sites to linearize an *E. coli* display system plasmid [45] encoding a fusion between the N-terminal part of Intimin and Boskar4 (pNB4, Table S3, Fig. S1B, C). The obtained PCR product was purified with the Wizard® SV Gel and PCR Clean-Up System (A928, Promega) and blunt end ligation was performed followed by electroporation of freshly made competent cells [81] to yield 3.6×10^7 total transformants. The *E. coli* strain DH10B $T1^R$ (C640003, Invitrogen) was used for all display experiments.

In more detail, prior to transformation, 0.4 U/µL T4 polynucleotide kinase (EK0031, Thermo Scientific™) was incubated with 5 ng/µL of linearized PCR product for 30 min at 37 °C, according to manufacturer instructions. After that, 0.25 U/µL T4 DNA ligase (EL0011, Thermo Scientific™) was added and incubated overnight at 16 °C. The ligation product was purified with the same PCR Clean-Up System mentioned above and eluted into 20 µL filtered ddH_2O. The complete 20 µL were transformed into electrocompetent *E. coli* as described in Tu *et al.* with the following changes [81]. In short, 50 mL of freshly grown *E. coli* exhibiting an optical density at 600 nm (OD_{600}) of ~ 0.6 were washed two times with 35 mL filtered H_2O. After washing, the bacterial pellet was resuspended with the purified ligation mix. The electroporation was performed at 1250 V and 5 ms. The cells were grown in 1 mL SOC Outgrowth Medium (B9020, NEB) for 2 h in a standard glass tube at 30 °C with 160 rpm. A 10-fold dilution series of the cells was made in SOC-medium, and they were plated on agar plates containing 34 µg/mL chloramphenicol and 2 % (w/v) D-glucose to estimate the total number of transformants. The rest of the sample was plated on five agar plates of the same type and incubated at 30 °C for about 20 h. The bacterial lawn was scraped from the plates and well mixed in 10 mL lysogeny broth (LB) medium. From 500 µL of bacterial suspension, the display plasmid containing the Boskar4 library was isolated and analyzed by Sanger sequencing with primers 19 and 20.

For the designed library, Damietta spl application [43] was used to estimate the free energy change of each single mutants of the same positions and same amino acids per position as the control library in a non-combinatorial manner. For each of the six positions, five amino acids with the lowest free energy change plus the original amino acid of Boskar4 at the corresponding position were used to define the designed, size-reduced library with a theoretical diversity of 3.89×10^4. The library was generated by PCR the same way as the original one but using three pairs of primers (primer 5 to 10, Table S1) such that the final library contained 15.6% of desired amino acids. The primer composition was designed by using the online tool of SwiftLib [82]. The designed library had a final theoretical diversity of 2.5×10^5, an amino-acid diversity of 2.3×10^5 and 2.7×10^7 total transformants were yielded.

Screening procedure for enhanced binders

The FACS-based screening of bacterially-displayed Boskar4 variants followed a slightly adapted procedure from that described by Salema *et al.* [45]. In brief, G-CSFR was first fluorescently labelled. This was done by incubating 100 µg of recombinant human G-CSFR (381-GR/CF, R&D Systems) in 950 µL PBS for 2 h at room temperature (RT) with Biotin-NHS (H1759, Sigma) in a 1:20 molar ratio (G-CSFR:Biotin-NHS). The reaction was stopped with 50 µL Tris (1 M pH 7.5). After 1 h of incubation on ice, the product was purified with a desalting column (Sephadex G25 PD-10, GE Healthcare), and the elution fractions were concentrated with Amicon Ultra centrifugal filter units (3 kDa, UFC800324, Merck) to a concentration of 0.24 mg/mL (3.6 µM). Aliquots of the biotinylated protein (herein referred to as BioGCSFR) were stored at -20 °C until use.

For the first sorting, DH10B T1^{R} *E. coli* cells were transformed with the display-vector pN containing a Boskar4 library. The bacteria were freshly grown on LB agar plates containing 34 µg/mL chloramphenicol and 2% (w/v) D-glucose at 30 °C yielding ~3.0×10^{8} total transformants. Following the harvesting of bacteria from the agar plates, 1 mL of resuspended bacterial culture exhibiting an OD_{600} of 3.3 was subjected to two successive washes, each involving 1 mL of LB medium. Subsequently, the culture was diluted to an initial OD_{600} of 0.33 by adding it to 10 mL of LB medium containing 34 µg/mL of chloramphenicol. The cells were cultivated at a temperature of 30 °C and an agitation rate of 160 rpm. After a duration of 1 h, 50 µM of isopropyl β-D-1-thiogalactopyranoside (IPTG) was introduced into the culture, and the cultivation was continued for an additional 3 h under the same growth conditions. Cells equivalent to 1 mL of a cell resuspension possessing an OD_{600} of 1 were collected, subjected to two washes with 1000 µL of phosphate-buffered saline (PBS), and eventually resuspended in 400 µL of PBS. 190 µL of this cell suspension was incubated with 10 nM BioGCSFR for 1 h at room temperature, followed by one wash with 1000 µL PBS. The washed cells were resuspended in 200 µL PBS containing 0.375 µL PE-Streptavidin (405203, BioLegend) and were subsequently incubated for 30 min at 4 °C. Finally, the sample was washed one more time with 1000 µL PBS and resuspended in 1000 µL PBS. FACS was performed with a BD FACSMelody™ Cell Sorter having set the PTM voltage for PE to 517 V, SSC to 426 V and a SSC threshold to 673 V. No gating was applied. All flow cytometry results were analyzed using FlowJo™ v10.1 Software (BD Life Sciences). 300 µL of the sample was mixed with 4 mL ice cold PBS and the flow rate was adjusted to end up with an event rate of ~8000 events/sec. 100,000 events were recorded per sample. The top ~0.1 % of the total population depending on a SSC-A/PE-A plot were sorted into a 1.5 mL tube provided with 200 µL LB medium and cooled to 5 °C. The sorting was continued until at least 20-fold more processed events were screened than the theoretical diversity of the correspondent library was. All sorted cells were plated on appropriate LB agar plates and incubated for about 20 h at 30 °C. Those plates were harvested and grown over night in LB medium containing 34 µg/mL chloramphenicol and 2% (w/v) D-glucose at 30 °C under static conditions. From this culture, 1 mL of resuspended bacteria with an OD_{600} of 3.3 used for the next selection cycle performed in the same way as the first one.

This was followed by evaluating the relative binding of the top clones using plate-based assays. At this stage, single colonies of bacteria pools which were enriched for 3 or 5 cycles of FACS-based sorting (as described in the section above) were grown overnight in 100 µL LB (supplemented with 34 µg/mL chloramphenicol and 50 µM IPTG) in a 96-well plate sealed with Breathe-Easy ® sealing membrane (Z380059, Sigma-Aldrich) at 30 °C with 1100 rpm on a table top shaker (Thermomixer comfort, Eppendorf) covered with aluminum foil. On the next day, the cells were centrifuged at 3200 g for 5 min, the supernatant was decanted, and the cells were resuspended in 150 µL PBS. The washing was repeated the same way one more time, and the cells were resuspended in 50 µL PBS containing 10 nM BioGCSFR. After the plate was incubated for 1 h at RT, the cells were washed once with 200 µL PBS and resuspended in 50 µL PBS. To visualize the binding activity of each displayed Boskar4 variant to BioGCSFR, two separate secondary stainings, one fluorescent and one chemiluminescent, were performed as follows:

For the fluorescent staining, 25 µL of the cells were mixed with 25 µL PBS containing 0.094 µL PE-streptavidin followed by a 30 min incubation at 4 °C in the dark. After washing the cells one more time with PBS, the OD_{600} and the fluorescence (excitation wavelength = 495 nm, emission wavelength = 574 nm) were measured on a plate reader (Synergy H4 Hybrid Microplate Reader, BioTek).

For the chemiluminescence stain, 25 µL of the cells were mixed with 25 µL PBS containing 1.25 µg/mL Avidin-HRP conjugate (Invitrogen, 434423) followed by a 30 min incubation at 4 °C in the dark. Afterwards the cells were washed once with 200 µL PBS and resuspended in 100 µL PBS. The OD_{600} of each well was measured with the plate reader. In a separate dark plate (655097, Greiner Bio One) 12.5 µL cell suspension was added to 75 µL PBS. Then 12.5 µL ECL-substrate-solution (1705061, Bio-Rad) was pipetted quickly into each well, the plate was sealed with parafilm and mixed vigorously for 10 seconds on a vortex orbital shaker. Then the luminescence of each well was measured on the plate reader (Synergy H4 Hybrid Microplate Reader, Agilent BioTek) set to an integration time of 1 second, a gain of 135, normal read speed and a 100-millisecond delay, and a read height of 1 mm.

Both readouts were analyzed by normalizing to the corresponding cell density and calculating a z-score for each sample over all wells of the same condition. From the top 5 variants of each condition, plasmids were isolated with a plasmid preparation kit (740588, Macherey-Nagel) from a 3 mL overnight culture grown at 30 °C with 160 rpm in LB with 34 µg/mL chloramphenicol and 2% (w/v) D-glucose.

Finally, to obtain the expression-normalized binding of the top clones with unique sequences another FACS experiment was carried out. The individual bacteria clones carrying the display vector pN with Intimin fused either to Boskar4 or enhanced Boskar4 variant (bv1 to bv16) were grown over night at 30 °C with 160 rpm in 3 mL LB with the addition of 34 µg/mL chloramphenicol and 50 µM IPTG. The cells were pelleted at 4000 g for 3 min, the supernatant was discarded and the sample was resuspended in 1000 µL filtered PBS. This washing step was repeated one more time and the cells were resuspended in 1000 µL PBS. 45 µL of cells suspension were incubated for 90 min at RT in a total volume of 55 µL with 10 nM BioGCSFR and 1:200 Myc-Tag (9B11) Mouse mAb (2276, Cell Signaling Technology). After one wash with 500 µL PBS, the cells were resuspended in 200 µL of PBS containing 0.375 µL PE-Streptavidin (405203, BioLegend) and 0.5 µL of anti-mouse-IgG1 conjugated to Alexa 488 Fluor (A-21202, Invitrogen) and incubated for 30 min at 4 °C in the dark. Finally, the sample was washed one more time with 500 µL PBS, resuspended in 1000 µL PBS, and 100000 events were measured by FACS.

Protein expression and purification

First, a set of affinity-enhanced Boskar4 (B4) variant genes (bv1, bv2, bv6, bv8, bv15, and to bv16), which were identified from the affinity maturation screens, were used to generate short tandem fusions (st2, compare Fig. S4). In more detail, a single Boskar4 variant gene was amplified by PCR from pN separately using two different primer pairs (15 and 16, or 17 and 18; Table S1). The two obtained PCR fragments were assembled by NEBuilder® HiFi DNA Assembly Master Mix (E2621, New England BioLabs) into a pET28a backbone generated by PCR with primers 13 and 14. Additionally, the monomer of bv6 was cloned from pN to pET28a.

E. coli BL21(DE3) carrying a certain expression construct were grown to an OD_{600} of ~0.6 in LB medium containing 40 µg/mL kanamycin at 37 °C and 160 rpm. Cells were induced with 0.5 mM IPTG and the protein expression was performed at 25 °C and 160 rpm for about 16 h. The cells were harvested at 8000 g for 30 min, the supernatant was decanted, and the pellet was lysed by sonication in lysis buffer (50 mM Tris pH8, 100 mM (for st2 designs) or 1 M NaCl (for ori designs), 20 µg/mL DNase (#A3778, ITW Reagents) and protease inhibitor cocktail (04693132001, Roche)). The lysate was centrifuged at 16000 g for 50 min, and the supernatant was used to perform Nickel Immobilized Metal Affinity Chromatography (IMAC). Finally, size exclusion chromatography (SEC) was

performed with PBS on the concentrated sample with a HiLoad 16/600, Superdex 200 pg (GE28-9893-35, Merck) column or other if mentioned in the corresponding legend description. Fractions that were supposed to contain the protein of the expected size were concentrated by ultrafiltration (10 kDa, UFC9010, Millipore), and aliquots were frozen at -20 °C until use.

Analysis of folding and thermal stability

Circular dichroism (CD) spectra were recorded using a JASCO J-810 spectrometer with 0.3 mL samples at a protein concentration of 0.1 mg/mL in PBS buffer (pH 7.1) placed in 2 mm path length cuvettes. The spectral scans of the mean residual ellipticity of three accumulations were measured at a resolution of at least 0.5 nm over a range of 250-190 nm. Nano differential scanning fluorimetry (nanoDSF) was conducted using a Prometheus NT.48 (Nanotemper) and standard Prometheus capillaries (Nanotemper, PR-C002). A temperature ramp of 1 °C/min from 20 °C to 110 °C to 20 °C was applied for melting and cooling, using 1 mg/mL protein samples in PBS (unless otherwise specified in the corresponding figure legend).

Affinity determination with surface plasmon resonance

To determine the receptor-binding affinity of Boskar4 variants, multi-cycle kinetics experiments were performed on a Biacore X100 system (GE Healthcare Life Sciences). Recombinant human G-CSFR (381-GR/CF, R&D Systems) was diluted to 50 µg/mL in 10 mM acetate buffer at pH 5.0 and immobilized on the surface of a CM5 sensor chip (GE Healthcare 29149604) using amine coupling chemistry. The protein samples were diluted in a running buffer (PBS with 0.05% v/v Tween-20). The measurements were performed at 25°C at a flow rate of 30 µL/min. Four sequential concentrations of the sample solution were used as follows: for Boskar4; 5000 nM, 2500 nM, 625 nM and 156.3 nM, for bv6; 125 nM, 63.5 nM, 31.3 nM, 15.6 nM; for all st2 variants (bv1_st2 to bv16_st2) and oris (ori0 to ori4); 20 nM, 10 nM, 5 nM and 2.5 nM). These samples were injected over the functionalized sensor chip surface for 180 s, followed by a 600 s dissociation phase with running buffer. At the end of each run, the sensor surface was regenerated with a 60 s injection of 50 mM NaOH. The reference responses and zero-concentration sensograms were subtracted from each dataset (double-referencing). Association rate constant (k_a), dissociation rate constant (k_d), and apparent equilibrium dissociation constants (K_D) were obtained using the Biacore X100 Evaluation Software following a 1:1 binding kinetic.

Generation of orientation-rigging designs

To generate preliminary constructs of the orientation-rigging designs (oris) containing a ridged helix-linker fusing two binding protein monomers, two bv6 monomers were connected N- to C-terminally (helix 4 of monomer 1 to helix 1 of monomer 2) with variable lengths of poly-alanine-stretches. The obtained sequences were modeled by AF2, and four constructs (ori1, ori2, ori3 and ori4) with an increasing number of connecting alanines were settled as a starting set of designs. The obtained AF2 structures were used as input to optimize the sequence of the helix-linker region with Damietta. Depending on the construct, up to 14 positions (compare Supplementary Methods) were mutated utilizing the few-to-many-to-few combinatorial sampler of Damietta (v0.32, [43]). Analysis of the designs' structural stability was done using a tempering molecular dynamics routine, and candidates ranked by their conformational homogeneity score, as previously described in [42]. This molecular dynamics analysis was performed for all unique variants that were generated by Damietta and the most stable variant of each construct was considered as the final design. To generate a binding protein in the same fashion that minimizes the distance of the two transmembrane domains of the bound G-CSFRs, hypothetical complexes of ridged tandem-fusions with varying poly-alanine-helix-stretches and two bound G-CSFRs were created manually. Based on the expected distance, possible steric hindrances and overall length of the ridged helix-linker, ori0 was selected and a final design was obtained as described above.

The ori expression constructs were generated the same way as explained for the short tandem fusions (compare Material and Methods section "Protein expression and purification"). In more detail, the two fragments (fr1 and fr2) encoding each one bv6 monomer and the corresponding ridged helix-linker were amplified and assembled together with the pET28a-backbone. The first fragment was generated with primer 15 plus the corresponding primer for each construct (primers 21, 23, 25, 27 or 29) and the second fragment with primer 18 plus the corresponding primer (primers 22, 24, 26, 28 or 30, Table S1).

NFS-60 cell proliferation assays

NFS-60 cells [46, 47] were maintained at 5% CO_2 and 37 °C in NFS-60-medium (RPMI 1640 medium with additional 1 mM L-glutamine, 1 mM Na-pyruvate, 10% FCS, 1% Antibiotic-Antimycotic (15240062, Gibco™) and 12.5% KMG-2: 5637-CM (Conditioned Medium from CLS Cell Lines Service)). Prior to the proliferation assay, the cells were washed 3 times with NFS-60-medium without KMG-2. The assay was performed in black 96-well plates (6005660, Perkin Elmer). For this purpose, 45.000 cells per well in a total volume of 150 µL NFS-60-medium without KMG-2 were cultured under maintenance conditions with different concentrations of designs or rhG-CSF for 48 h. Then, 30 µL of CellTiter-Blue® Reagent (G808, Promega) was added to each well and cells were further cultivated for approximately 90 min under maintenance conditions. Subsequently, the fluorescence of each well was recorded with a plate reader (Synergy H4 Hybrid Microplate Reader, Agilent BioTek) with an excitation wavelength of 560 nm and emission at 590 nm. The half-maximal effective concentration (EC_{50}) of each design or rhG-CSF was determined by fitting the obtained fluorescence values to their corresponding concentrations using a four-parameter sigmoidal function and the Nelder-Mead Simplex algorithm from the Python module SciPy [83]. For the analysis of the maximum response of proliferative activity (E_{max}), the mean of the three highest concentrations was estimated for each sample, such that all values considered for the analysis were in the activity plateau. These means were normalized to the maximum response within each experiment to account for the general variability of cell activity between the independent replicates. For statistical analysis, an ordinary one-way ANOVA followed by a Tukey HSD test was performed.

Testing of granulopoietic activity of designed proteins in vivo

To test the effect of the designs on zebrafish granulopoiesis, equal volumes (4 nL) of Moevan_control (4 mg/mL), rhG-CSF (2 mg/mL), Boskar4 variants, bv6_st2 (2 mg/mL) and bv8_st2 (2 mg/mL) were injected into the cardinal vein of transgenic *Tg(mpx:GFP)* [48] larvae at 1.5-day post-fertilization (dpf). Injected larvae were incubated at 28 °C. To quantify neutrophils 24 hours upon injection, larvae were positioned and orientated laterally within cavities formed in 1% agarose on a 96-well plate and then imaged using an SMZ18 Nikon fluorescence stereomicroscope. The number of GFP-expressing neutrophils was automatically determined by Imaris software using the spot detection tool. Fold change of the neutrophils was calculated by normalizing to the average of uninjected mpx:*gfp* counterparts at the same developmental stage. Zebrafish lines were maintained according to standard protocols and handled in accordance with European Union animal protection directive 2010/63/EU and approved by the local government (Tierschutzgesetz §11, Abs. 1, Nr. 1, husbandry permit 35/9185.46/Uni TÜ). All experiments described in the present study were conducted on larvae younger than 5 dpf.

For the mouse treatment experiments, B6.SJL-PtprcaPepcb/BoyCrl (Ly5.1) mice, aged between 6 to 8 weeks, were treated with intraperitoneal injections (i.p.) of rhG-CSF, or Boskar4 variants, bv6_st2 and bv8_st2. A concentration of 300 µg/kg was used for each protein injecting mice every second day for a total of five injections. Bone marrow cells of treated mice were isolated by flushing with a 22G syringe and subsequent filtering through a 45 µm cell strainer. After that, cells were counted and used for flow cytometry analyses on a FACS Canto II (BD) and using FlowJo (BD). Cells were stained with DAPI (#D9542, Sigma), anti-mouse CD45.1 PerCP (#110725, Biolegend), anti-mouse Ly6C AF488 (#128022, Biolegend), and anti-mouse Ly6G APC (#127614, Biolegend) antibody. Gates were

set according to fluorescence minus one (FMO) control. Mice were maintained under pathogen-free conditions in the research animal facility of the University of Tübingen, according to German federal and state regulations (Regierungspräsidium Tübingen, M 05-20 G).

Single molecule imaging and analysis

For cell surface labelling, G-CSFR was N-terminally fused to the ALFA-tag. Additionally, to assess the co-expression of JAK2ΔTK it was C-terminally fused to mEGFP. Both proteins were encoded on pSems vectors including the signal sequence of Igκ (pSems-leader) [84]. HeLa cells (ACC 57, DSMZ Germany) were cultured as previously described [85]. For transient transfection, cells were incubated for 4-6 h with a mixture of 150 mM NaCl, 10 µL of 1 mg/mL polyethylenimine (PEI MAX®, Polysciences 24765) and 1500 ng (ALFAtag-G-CSFR) and 2500 ng (JAK2ΔTK-mEGFP) of the desired constructs. Labeling, washing and subsequent imaging were performed after mounting the coverslips into custom-made incubation chambers with a volume of 1 ml. Cells were equilibrated in medium with FBS but lacking phenol red supplemented with an oxygen scavenger and a redox-active photoprotectant (0.5 mg/mL glucose oxidase (Sigma-Aldrich), 0.04 mg/mL catalase (Roche), 5% w/v glucose, 1 µM ascorbic acid and 1 µM methylviologene) to minimize photobleaching [86].

Selective cell surface receptor labeling was achieved by using anti-ALFAtag NBs, which were site-specifically labeled by maleimide chemistry via a single cysteine residue at their C-termini [86]. NBs labeled with Cy3B (DOL: 1.0) and ATTO 643 (DOL: 1.0) were added at concentrations of 3 nM each, at least 10 min before imaging. Coverslips were precoated with poly-l-lysine-graft-poly(ethylene glycol) to minimize unspecific binding of NBs and functionalized with RGD peptide for efficient cell adhesion [87].

Single-molecule imaging was carried out by dual-color total internal reflection fluorescence microscopy using an inverted microscope (IX71, Olympus) equipped with a spectral image splitter (DualView, Optical Insight) and a back-illuminated electron multiplied CCD camera (iXon DU897D, Andor Technology). Fluorophores were excited by simultaneous illumination with a 561-nm laser (CrystaLaser; approximately 32 $W \cdot cm^{-2}$) and a 642-nm laser (Omicron: approximately 22 $W \cdot cm^{-2}$). Image stacks of 150 frames were recorded for each cell at a time resolution of 32 ms per frame, with at least 10 cells recorded in each experiment. Ligands were incubated for 10 min before imaging. All imaging experiments were carried out at room temperature. Prior to image acquisition, the presence of JAK2ΔTK-mEGFP was confirmed through emission with a 488-nm laser (Sapphire LP, Coherent)

Dual-color time-lapse images were evaluated using an in-house developed MATLAB software (SLIMfast4C, https://zenodo.org/record/5712332) as previously described in detail [86]. After channel registration based on calibration with fiducial markers, molecules were localized using the multi-target tracking algorithm [88]. Immobile emitters were filtered out by spatiotemporal cluster analysis [89]. For co-tracking, frame-by-frame co-localization within a cut-off radius of 100 nm was applied followed by tracking of co-localized emitters using the utrack algorithm [90]. Molecules co-diffusing for 10 frames or more were identified as co-localized. Relative levels of co-localization were determined based on the fraction of co-localized particles [87]. Diffusion properties were determined from pooled single trajectories using mean squared displacement analysis for all trajectories with a lifetime greater than 10 frames. Diffusion constants were determined from the mean squared displacement by linear regression.

Analysis of STAT3/5 phosphorylation by Western Blot

NFS-60 cells were washed two times with NFS-60-medium (RPMI 1640 medium with additional 1 mM L-glutamine, 1 mM Na-pyruvate, 10% FCS, 1% Antibiotic-Antimycotic (15240062, Gibco™)) and starved at 300,000 cells/mL for 16 h at 5 % CO_2 and 37 °C. Subsequently, the starved cells were treated with 1 nM of rhG-CSF or the selected design for 5 min or 30 min.

Following the treatment, the cells were consistently maintained at low temperatures on ice. They were harvested using a refrigerated centrifuge operating at 4 °C at 300 g for 2 min. The cells were washed once with ice-cold PBS and the dry pellets were frozen at – 70 °C until further use. Whole-cell lysates were obtained by lysing 1×10^6 cells in 200 µL Laemmli buffer (30% glycerol, 6% SDS, 7.5% β-Mercaptoethanol, 0.75% Bromphenol blue in 200 nM Tris-HCL [pH 6.8]), which were subsequently heated at 95 °C for 5 min and spun down. Proteins were separated by dodecyl-sulfate polyacrylamide gel electrophoresis and transferred to Amersham™ Protran® nitrocellulose membranes or PVDF membranes (Invitrogen). The membranes were blocked with 5% non-fat dry milk-TBST (10 mM Tris-HCL [pH 8.0], 150 mM NaCl, 0.1% Tween® 20) for 1 h at room temperature and subsequently incubated with primary antibodies in 8 mL milk-TBST buffer overnight at 4 °C or for 2 h at room temperature (RT). After washing 4 times for 5 min with TBST, membranes were incubated with secondary antibodies in 8 mL milk-TBST buffer for 1 h at RT and then again washed 4 times for 5 min with TBST. The protein bands were detected using Pierce (Thermo Fisher Scientific) or Clarity (BioRad) ECL western blotting substrate kits, and imaged using Fusion FX (Vilber) or Sapphire™ (Azure Biosystems) imagers. The following antibodies and corresponding dilutions were used: primary rabbit polyclonal antibodies against: STAT5 1:500 (Cell Signaling, #9363S), phosphorylated STAT5 (Tyr694) 1:750 (Cell Signaling, #9351S), STAT3 1:200 (SantaCruz, # SC-482), alpha-tubulin 1:1000 (Cell Signaling, #2144S), primary rabbit monoclonal antibodies against: STAT5 1:1000 (Cell Signaling, #94205S), STAT3 1:1000 (Cell Signaling, #12640S), phosphorylated STAT3 (Tyr705) 1:1000 (Cell Signaling, #9145L), and GAPDH 1:1000 (Cell Signaling #2118S), and secondary horseradish peroxidase-conjugated anti-rabbit antibodies 1:3000 (Cell Signaling, #7074, or Jackson ImmunoResearch, #111-035-003). Gel images were exported for analysis as .tiff files and processed using FIJI software [91]. Following brightness/contrast adjustments, the bands of interest were isolated with the rectangle tool, and the peaks of band intensity were plotted. The peaks were individually separated using the line tool, and the areas under each peak were measured to determine the signal intensities of the immuno-detected proteins. Subsequently, these signal intensities were normalized by the corresponding signal of the housekeeping protein.

Colony-forming unit (CFU) assay with human HSPCs

Human $CD34^+$ cells were isolated from the bone marrow mononuclear cell fraction of two healthy donors by Ficoll density gradient centrifugation with subsequent magnetic bead separation using the Human CD34 Progenitor Cell Isolation Kit (Miltenyi Biotech Germany; #130-046-703). Isolated cells were frozen until further analysis. $CD34^+$ HSPCs at a concentration of 1×10^4 cells/mL were plated in 35 mm cell culture dishes in 1 mL Methocult H4230 medium (Stemcell Technologies) supplemented with 2% FBS, 10 µg/mL 100x Antibiotic-Antimycotic Solution (Sigma) 50 ng/mL SCF, 20 ng/mL IL-3 and 20 ng/mL rhG-CSF, or 100 ng/mL designed agonists. Cells were cultured at 37 °C and 5% CO_2. Colonies were counted on day 14.

Evaluation of time-dependent effects of the designed agonists on the proliferation of CD34+ HSPCs

$CD34^+$ HSPCs were isolated and processed as described above. Cells were incubated in poly-L-lysine–coated 96-well plates (2 × 104 cells/well) in Stemline II Hematopoietic Stem Cell Expansion medium (Sigma Aldrich; #50192) supplemented with 10% FBS, 1% penicillin/streptomycin, 1% L-glutamine and 50 ng/mL SCF, 20 ng/mL IL-3 and 10 ng/mL rhG-CSF, or designed agonists at different concentrations. using an IncuCyte S3 Live-Cell Analysis System (Essen Bio) with a 10 x objective at 37 °C and 5% CO_2. Cell proliferation over time was analyzed using IncuCyte S3 Software. Experiments in this study involving human samples were conducted according to Helsinki's declaration, and study approval was obtained from the Ethical Review Board of the Medical Faculty, University of Tübingen (012/2021BO2).

RNA-sequencing analysis

NFS-60 cells were washed two times with NFS-60-medium (RPMI 1640 medium with additional 1 mM L-glutamine, 1 mM Na-pyruvate, 10% FCS, 1% Antibiotic-Antimycotic (15240062, Gibco™)) and starved at 300,000 cells/mL for 16 h at 5% CO_2 and 37 °C. 1.5 million cells per sample in a T25 cell-culture flask were stimulated with 1 nM of the selected design or rhG-CSF for 8 h. Subsequently, the cells were washed twice with PBS, lysed in 350 µL RTL buffer and stored at -70 °C until RNA extraction. At least 500 ng of RNA per sample was used to prepare libraries for RNA sequencing. The RNA Integrity Number (RIN) for RNA quality assessment was measured using a 2100 Bioanalyzer (Agilent). All RNA samples showed RIN > 9,6 (max = 10), demonstrating high quality of the RNA samples. Directional mRNA library preparation (poly A enrichment) and sequencing were done by Novogene (https://www.novogene.com). The libraries were sequenced on an Illumina NovaSeq 6000 using paired-end 150 bp sequencing mode with a minimum of 6 Gb of raw data per sample. For data analysis, nf-core/rnaseq (https://nf-co.re/rnaseq, [92]) was used, an RNA sequencing analysis pipeline that takes a sample sheet and FASTQ files as input, performs quality assessment, trimming, alignment, and produces a gene count table and extensive QC report. Nf-core/rnaseq pipeline was run with the following parameters: --profile 'docker,' --genome 'GRCm38,' --aligner 'star_salmon,' pipeline version 3.10. Raw sequencing read counts were analyzed with the R package edgeR v3.42.2 [93]. 11,801 of initial 45,706 transcripts showed sufficient level of expression. Normalized log2 cpm values were used for PCA and descriptive part of the analysis. Differential expression was determined by fitting a quasi-likelihood negative binomial generalized log-linear model to count data. Resulting candidate genes that passed thresholds of absolute log2 fold change > 1 and FDR < 0.05 were tested for gene set enrichment using the R package clusterProfiler v4.8.1 [94]. Two gene set collections were used: GO terms and MSigDB m2 mouse collection v2022.1.

Acknowledgements

This project has received funding from the IMPRS (TU, KM), the European Research Council under the European Union's Horizon 2020 research and innovation program (grant agreement No 863952 (ACE-OF-SPACE)) (PM), the M. Schickedanz Kinderkrebsstiftung (ME, JS, PM, NA), "German Universities Excellence Initiative" of the Tübingen University (JS), Deutsche Forschungsgemeinschaft (DFG; No 500215849; ME, BHA, JS, VH), (DFG; PI 405/15-2 – 326558201 and SFB; 1557, P13 – 467522186; JP). The authors would also like to thank Luis Ángel Fernández for providing the bacterial display system plasmid, and Regine Bernhard, Gabriele Hikade and Hella Kenneweg for technical assistance.

References

1. Rochman, Y., R. Spolski, and W.J. Leonard, *New insights into the regulation of T cells by gamma(c) family cytokines*. Nature reviews. Immunology, 2009. **9**(7): p. 480–490.
2. Spangler, J.B., et al., *Insights into cytokine-receptor interactions from cytokine engineering.* Annual review of immunology, 2015. **33**: p. 139–167.
3. Leonard, W.J. and J.X. Lin, *Cytokine receptor signaling pathways.* J Allergy Clin Immunol, 2000. **105**(5): p. 877-88.
4. Bezbradica, J.S. and R. Medzhitov, *Integration of cytokine and heterologous receptor signaling pathways.* Nature Immunology, 2009. **10**(4): p. 333-339.
5. Leonard, W.J. and J.X. Lin, *Strategies to therapeutically modulate cytokine action.* Nat Rev Drug Discov, 2023. **22**(10): p. 827-854.
6. Stroud, R.M. and J.A. Wells, *Mechanistic Diversity of Cytokine Receptor Signaling Across Cell Membranes.* Science's STKE, 2004. **2004**(231): p. re7.
7. Spangler, J.B., et al., *Insights into Cytokine–Receptor Interactions from Cytokine Engineering.* Annual Review of Immunology, 2015. **33**(1): p. 139-167.
8. Wilmes, S., et al., *Mechanism of homodimeric cytokine receptor activation and dysregulation by oncogenic mutations.* Science, 2020. **367**(6478): p. 643-652.
9. Glassman, C.R., et al., *Structure of a Janus kinase cytokine receptor complex reveals the basis for dimeric activation.* Science, 2022. **376**(6589): p. 163-169.
10. Schreiber, G. and M.R. Walter, *Cytokine-receptor interactions as drug targets.* Curr Opin Chem Biol, 2010. **14**(4): p. 511-9.
11. Saxton, R.A., C.R. Glassman, and K.C. Garcia, *Emerging principles of cytokine pharmacology and therapeutics.* Nature reviews. Drug discovery, 2022.
12. Schreiber, G. and J. Piehler, *The molecular basis for functional plasticity in type I interferon signaling.* Trends Immunol, 2015. **36**(3): p. 139-149.
13. Heike, T. and T. Nakahata, *Ex vivo expansion of hematopoietic stem cells by cytokines.* Biochimica et Biophysica Acta (BBA) - Molecular Cell Research, 2002. **1592**(3): p. 313-321.
14. Mitra, S., et al., *Interleukin-2 Activity Can Be Fine Tuned with Engineered Receptor Signaling Clamps.* Immunity, 2015. **42**(5): p. 826-838.
15. Saxton, R.A., et al., *The tissue protective functions of interleukin-22 can be decoupled from pro-inflammatory actions through structure-based design.* Immunity, 2021. **54**(4): p. 660-672.e9.
16. Wilmes, S., et al., *Receptor dimerization dynamics as a regulatory valve for plasticity of type I interferon signaling.* Journal of Cell Biology, 2015. **209**(4): p. 579-593.
17. Moraga, I., et al., *Multifarious determinants of cytokine receptor signaling specificity.* Adv Immunol, 2014. **121**: p. 1-39.
18. Syed, R.S., et al., *Efficiency of signalling through cytokine receptors depends critically on receptor orientation.* Nature, 1998. **395**(6701): p. 511-516.
19. Staerk, J., et al., *Orientation-specific signalling by thrombopoietin receptor dimers.* The EMBO Journal, 2011. **30**(21): p. 4398-4413.
20. Wilson, I.A. and L.K. Jolliffe, *The structure, organization, activation and plasticity of the erythropoietin receptor.* Current Opinion in Structural Biology, 1999. **9**(6): p. 696-704.
21. Ballinger, M.D. and J.A. Wells, *Will any dimer do?* Nature Structural Biology, 1998. **5**(11): p. 938-940.
22. Mohan, K., et al., *Topological control of cytokine receptor signaling induces differential effects in hematopoiesis.* Science, 2019. **364**(6442).
23. Moraga, I., et al., *Tuning cytokine receptor signaling by re-orienting dimer geometry with surrogate ligands.* Cell, 2015. **160**(6): p. 1196–1208.
24. Yen, M., et al., *Facile discovery of surrogate cytokine agonists.* Cell, 2022. **185**(8): p. 1414-1430.e19.
25. Dwivedi, P. and K.D. Greis, *Granulocyte colony-stimulating factor receptor signaling in severe congenital neutropenia, chronic neutrophilic leukemia, and related malignancies.* Experimental hematology, 2017. **46**: p. 9–20.

26. O'Shea, J.J. and R. Plenge, *JAK and STAT signaling molecules in immunoregulation and immune-mediated disease.* Immunity, 2012. **36**(4): p. 542–550.
27. Palande, K., et al., *Scratching the surface: signaling and routing dynamics of the CSF3 receptor.* Frontiers in bioscience (Landmark edition), 2013. **18**(1): p. 91–105.
28. Aritomi, M., et al., *Atomic structure of the GCSF-receptor complex showing a new cytokine-receptor recognition scheme.* Nature, 1999. **401**(6754): p. 713–717.
29. Mine, S., et al., *Thermodynamic analysis of the activation mechanism of the GCSF receptor induced by ligand binding.* Biochemistry, 2004. **43**(9): p. 2458–2464.
30. Tamada, T., et al., *Homodimeric cross-over structure of the human granulocyte colony-stimulating factor (GCSF) receptor signaling complex.* Proceedings of the National Academy of Sciences of the United States of America, 2006. **103**(9): p. 3135–3140.
31. Franzke, A., *The role of G-CSF in adaptive immunity.* Cytokine & growth factor reviews, 2006. **17**(4): p. 235-244.
32. Welte, K., et al., *Filgrastim (r-metHuG-CSF): The First 10 Years.* Blood The Journal of The American Society of Hematology, 1996. **88**(6): p. 1907–1929.
33. Welte, K., et al., *Purification and biochemical characterization of human pluripotent hematopoietic colony-stimulating factor.* Proceedings of the National Academy of Sciences of the United States of America, 1985. **82**(5): p. 1526–1530.
34. Morris, R., N.J. Kershaw, and J.J. Babon, *The molecular details of cytokine signaling via the JAK/STAT pathway.* Protein science : a publication of the Protein Society, 2018. **27**(12): p. 1984–2009.
35. Tian, S.-S., et al., *Multiple signaling pathways induced by granulocyte colony-stimulating factor involving activation of JAKs, STAT5, and/or STAT3 are required for regulation of three distinct classes of immediate early genes.* 1996.
36. Shimozaki, K., et al., *Involvement of STAT3 in the granulocyte colony-stimulating factor-induced differentiation of myeloid cells.* Journal of Biological Chemistry, 1997. **272**(40): p. 25184-25189.
37. Dong, F., et al., *Stimulation of Stat5 by granulocyte colony-stimulating factor (G-CSF) is modulated by two distinct cytoplasmic regions of the G-CSF receptor.* The Journal of Immunology, 1998. **161**(12): p. 6503-6509.
38. Ward, A.C., et al., *Multiple signals mediate proliferation, differentiation, and survival from the granulocyte colony-stimulating factor receptor in myeloid 32D cells.* Journal of Biological Chemistry, 1999. **274**(21): p. 14956-14962.
39. Chakraborty, A. and D.J. Tweardyabc, *Stat3 and G-CSF-induced myeloid differentiation.* Leukemia & lymphoma, 1998. **30**(5-6): p. 433-442.
40. Ward, A.C., et al., *Defective internalization and sustained activation of truncated granulocyte colony-stimulating factor receptor found in severe congenital neutropenia/acute myeloid leukemia.* Blood, The Journal of the American Society of Hematology, 1999. **93**(2): p. 447-458.
41. Ward, A.C., et al., *Novel point mutation in the extracellular domain of the granulocyte colony-stimulating factor (G-CSF) receptor in a case of severe congenital neutropenia hyporesponsive to G-CSF treatment.* The Journal of experimental medicine, 1999. **190**(4): p. 497-508.
42. Skokowa, J., et al., *A topological refactoring design strategy yields highly stable granulopoietic proteins.* Nature communications, 2022. **13**(1): p. 2948.
43. Maksymenko, K., et al., *The design of functional proteins using tensorized energy calculations.* Cell Reports Methods, 2023. **3**(8): p. 100560.
44. Young, D.C., et al., *Characterization of the receptor binding determinants of granulocyte colony stimulating factor.* Protein Science, 1997. **6**(6): p. 1228-1236.
45. Salema, V., et al., *Selection of single domain antibodies from immune libraries displayed on the surface of E. coli cells with two β-domains of opposite topologies.* PloS one, 2013. **8**(9): p. e75126.
46. Weinstein, Y., et al., *Truncation of the c-myb gene by a retroviral integration in an interleukin 3-dependent myeloid leukemia cell line.* Proceedings of the National Academy of Sciences, 1986. **83**(14): p. 5010-5014.

47. Nakoinz, I., et al., *Differentiation of the IL-3-dependent NFS-60 cell line and adaption to growth in macrophage colony-stimulating factor.* Journal of immunology (Baltimore, Md.: 1950), 1990. **145**(3): p. 860-864.
48. Renshaw, S.A., et al., *A transgenic zebrafish model of neutrophilic inflammation.* Blood, 2006. **108**(13): p. 3976-8.
49. Hernandez Alvarez, B., et al., *Design of novel granulopoietic proteins by topological rescaffolding.* PLOS Biology, 2020. **18**(12): p. e3000919.
50. Jumper, J., et al., *Highly accurate protein structure prediction with AlphaFold.* Nature, 2021. **596**(7873): p. 583-589.
51. Tsirigotaki, A., et al., *Mechanism of receptor assembly via the pleiotropic adipokine Leptin.* Nat Struct Mol Biol, 2023. **30**(4): p. 551-563.
52. Whitty, A. and C.W. Borysenko, *Small molecule cytokine mimetics.* Chem Biol, 1999. **6**(4): p. R107-18.
53. Lamken, P., et al., *Ligand-induced assembling of the type I interferon receptor on supported lipid bilayers.* J Mol Biol, 2004. **341**(1): p. 303-18.
54. Whitty, A., et al., *Interaction affinity between cytokine receptor components on the cell surface.* Proc Natl Acad Sci U S A, 1998. **95**(22): p. 13165-70.
55. Salavessa, L., et al., *Cytokine receptor cluster size impacts its endocytosis and signaling.* Proc Natl Acad Sci U S A, 2021. **118**(37).
56. Park, S.D., et al., *A review of granulocyte colony-stimulating factor receptor signaling and regulation with implications for cancer.* Frontiers in Oncology, 2022. **12**: p. 932608.
57. Touw, I.P. and G.-J.M. van de Geijn, *Granulocyte colony-stimulating factor and its receptor in normal myeloid cell development, leukemia and related blood cell disorders.* Frontiers in Bioscience, 2007. **12**(1): p. 800–815.
58. Acres, B., et al., *Fusokine interleukin-2/interleukin-18, a novel potent innate and adaptive immune stimulator with decreased toxicity.* Cancer Res, 2005. **65**(20): p. 9536-46.
59. Bhatt, S., et al., *Anti-CD20-interleukin-21 fusokine targets malignant B cells via direct apoptosis and NK-cell-dependent cytotoxicity.* Blood, 2017. **129**(16): p. 2246-2256.
60. Deng, J., et al., *GM-CSF and IL-4 Fusion Cytokine Induces B Cell-Dependent Hematopoietic Regeneration.* Mol Ther, 2017. **25**(2): p. 416-426.
61. Deng, J., et al., *GIFT4 fusokine converts leukemic B cells into immune helper cells.* J Transl Med, 2016. **14**(1): p. 106.
62. Deng, J., et al., *Engineered fusokine GIFT4 licenses the ability of B cells to trigger a tumoricidal T-cell response.* Cancer Res, 2014. **74**(15): p. 4133-44.
63. Rafei, M., et al., *Selective inhibition of CCR2 expressing lymphomyeloid cells in experimental autoimmune encephalomyelitis by a GM-CSF-MCP1 fusokine.* J Immunol, 2009. **182**(5): p. 2620-7.
64. Rafei, M., et al., *A granulocyte-macrophage colony-stimulating factor and interleukin-15 fusokine induces a regulatory B cell population with immune suppressive properties.* Nat Med, 2009. **15**(9): p. 1038-45.
65. Rafei, M., et al., *A GMCSF and IL-15 fusokine leads to paradoxical immunosuppression in vivo via asymmetrical JAK/STAT signaling through the IL-15 receptor complex.* Blood, 2007. **109**(5): p. 2234-42.
66. Van der Jeught, K., et al., *Intratumoral administration of mRNA encoding a fusokine consisting of IFN-β and the ectodomain of the TGF-β receptor II potentiates antitumor immunity.* Oncotarget, 2014. **5**(20): p. 10100-13.
67. Moraga, I., et al., *Synthekines are surrogate cytokine and growth factor agonists that compel signaling through non-natural receptor dimers.* eLife, 2017. **6**: p. e22882.
68. ElGamacy, M., *Accelerating therapeutic protein design.* Adv Protein Chem Struct Biol, 2022. **130**: p. 85-118.
69. Bishop, B., et al., *Reengineering granulocyte colony-stimulating factor for enhanced stability.* J Biol Chem, 2001. **276**(36): p. 33465-70.
70. Shibuya, R., T. Miyafusa, and S. Honda, *Stabilization of backbone-circularized protein is attained by synergistic gains in enthalpy of folded structure and entropy of unfolded structure.* The FEBS Journal, 2020. **287**(8): p. 1554-1575.

71. Wood, V.E., et al., *Protein Engineering and HDX Identify Structural Regions of G-CSF Critical to Its Stability and Aggregation.* Mol Pharm, 2022. **19**(2): p. 616-629.
72. Ward, A.C., et al., *Tyrosine-dependent and-independent mechanisms of STAT3 activation by the human granulocyte colony-stimulating factor (G-CSF) receptor are differentially utilized depending on G-CSF concentration.* Blood, The Journal of the American Society of Hematology, 1999. **93**(1): p. 113-124.
73. Gonnord, P., C.M. Blouin, and C. Lamaze, *Membrane trafficking and signaling: two sides of the same coin.* Semin Cell Dev Biol, 2012. **23**(2): p. 154-64.
74. Cendrowski, J., A. Maminska, and M. Miaczynska, *Endocytic regulation of cytokine receptor signaling.* Cytokine Growth Factor Rev, 2016. **32**: p. 63-73.
75. Silva, D.A., et al., *De novo design of potent and selective mimics of IL-2 and IL-15.* Nature, 2019. **565**(7738): p. 186-191.
76. Yang, H., et al., *Design of cell-type-specific hyperstable IL-4 mimetics via modular de novo scaffolds.* Nat Chem Biol, 2023. **19**(9): p. 1127-1137.
77. Cui, L., et al., *Tuning MPL signaling to influence hematopoietic stem cell differentiation and inhibit essential thrombocythemia progenitors.* Proceedings of the National Academy of Sciences, 2021. **118**(2): p. e2017849118.
78. Tsutsumi, N., et al., *Structure of the thrombopoietin-MPL receptor complex is a blueprint for biasing hematopoiesis.* Cell.
79. Franzke, A., et al., *G-CSF as immune regulator in T cells expressing the G-CSF receptor: implications for transplantation and autoimmune diseases.* Blood, 2003. **102**(2): p. 734-739.
80. Karagiannidis, I., et al., *G-CSF in tumors: Aggressiveness, tumor microenvironment and immune cell regulation.* Cytokine, 2021. **142**: p. 155479.
81. Tu, Q., et al., *Room temperature electrocompetent bacterial cells improve DNA transformation and recombineering efficiency.* Scientific reports, 2016. **6**(1): p. 1-8.
82. Jacobs, T.M., et al., *SwiftLib: rapid degenerate-codon-library optimization through dynamic programming.* Nucleic acids research, 2015. **43**(5): p. e34-e34.
83. Virtanen, P., et al., *SciPy 1.0: fundamental algorithms for scientific computing in Python.* Nature methods, 2020. **17**(3): p. 261-272.
84. Gotzke, H., et al., *The ALFA-tag is a highly versatile tool for nanobody-based bioscience applications.* Nat Commun, 2019. **10**(1): p. 4403.
85. Wilmes, S., et al., *Receptor dimerization dynamics as a regulatory valve for plasticity of type I interferon signaling.* J Cell Biol, 2015. **209**(4): p. 579-93.
86. Sotolongo Bellon, J., et al., *Four-color single-molecule imaging with engineered tags resolves the molecular architecture of signaling complexes in the plasma membrane.* Cell reports methods, 2022. **2**(2): p. 100165.
87. You, C., et al., *Dynamic submicroscopic signaling zones revealed by pair correlation tracking and localization microscopy.* Anal Chem, 2014. **86**(17): p. 8593-602.
88. Serge, A., et al., *Dynamic multiple-target tracing to probe spatiotemporal cartography of cell membranes.* Nature methods, 2008. **5**(8): p. 687-94.
89. Niewidok, B., et al., *Single-molecule imaging reveals dynamic biphasic partition of RNA-binding proteins in stress granules.* The Journal of cell biology, 2018. **217**(4): p. 1303-1318.
90. Jaqaman, K., et al., *Robust single-particle tracking in live-cell time-lapse sequences.* Nature methods, 2008. **5**(8): p. 695-702.
91. Schindelin, J., et al., *Fiji: an open-source platform for biological-image analysis.* Nature methods, 2012. **9**(7): p. 676-682.
92. Ewels, P.A., et al., *The nf-core framework for community-curated bioinformatics pipelines.* Nat Biotechnol, 2020. **38**(3): p. 276-278.
93. Chen, Y., A.T. Lun, and G.K. Smyth, *From reads to genes to pathways: differential expression analysis of RNA-Seq experiments using Rsubread and the edgeR quasi-likelihood pipeline.* F1000Res, 2016. **5**: p. 1438.
94. Yu, G., et al., *clusterProfiler: an R Package for Comparing Biological Themes Among Gene Clusters.* OMICS: A Journal of Integrative Biology, 2012. **16**(5): p. 284-287.
95. Nguyen-Jackson, H.T., H. Zhang, and S.S. Watowich, *G-CSF Receptor Structure, Function, and Intracellular Signal Transduction*, in *Twenty Years of G-CSF: Clinical and Nonclinical*

Discoveries, G. Molineux, M. Foote, and T. Arvedson, Editors. 2012, Springer Basel: Basel. p. 83-105.

Figures

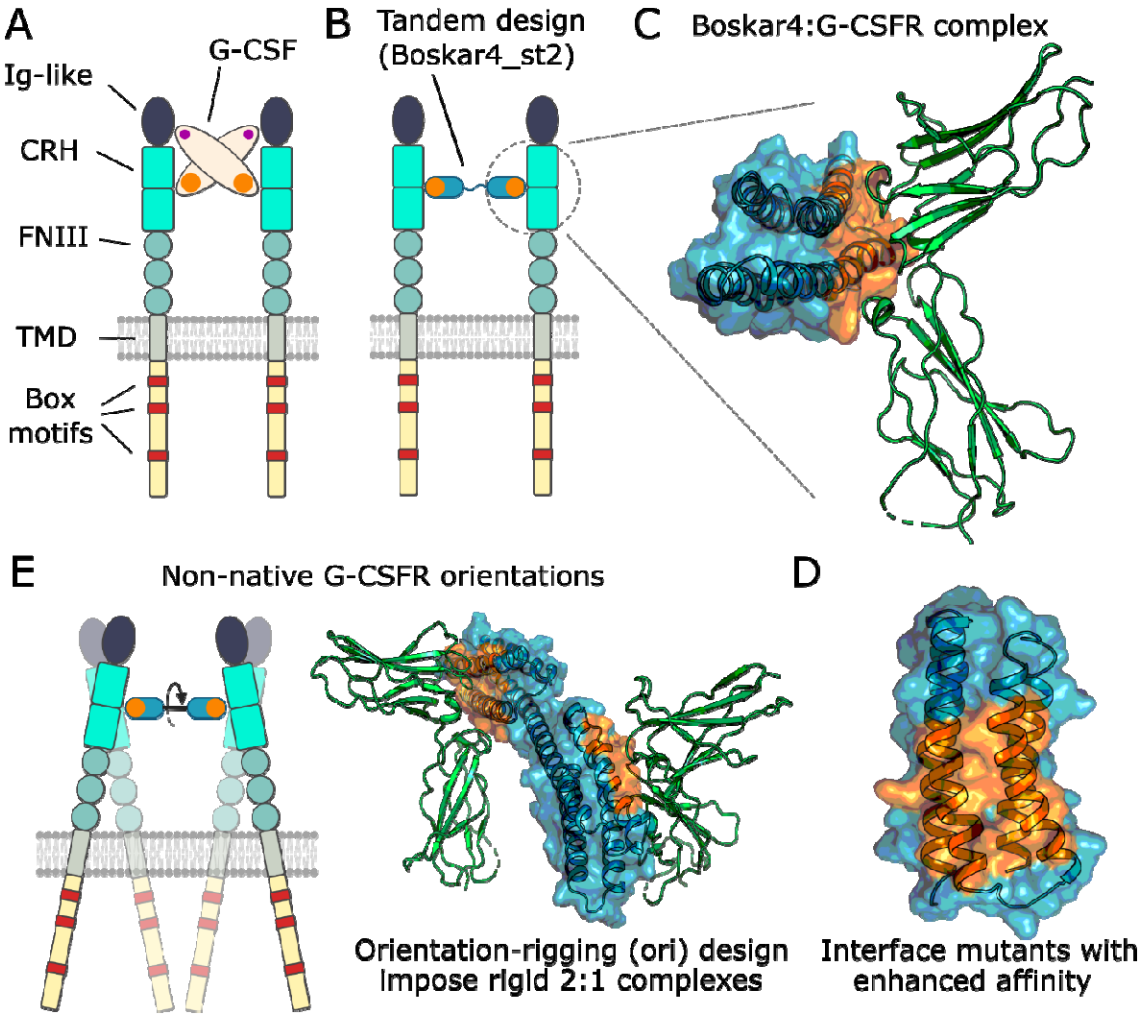

Figure 1. Overall strategy to generate novel G-CSFR modulators with varying affinities and geometries. (A) G-CSF (beige oval) activates G-CSFR by dimerizing the Ig-like and CRH domains (dark blue and cyan) through two distinct receptor-binding sites (orange and purple) [95]. **(B)** In contrast, the *de novo*-designed Boskar4_st2 agonist consists of two tandemly repeated Boskar4 domains, which **(C)** possess minimal architecture and encode a single high-affinity, receptor-binding site (blue domain and orange surface patch). **(D)** On the Boskar4 module, the residues forming the receptor-binding entity were diversified in order to identify affinity-enhanced variants. **(E)** The improved Boskar4 module was fused into rigid, orientation-rigging designs (oris) that can dimerize and activate G-CSFR in non-native geometries. The purple box shows a modeled structure of one example ori binding to two G-CSFR.

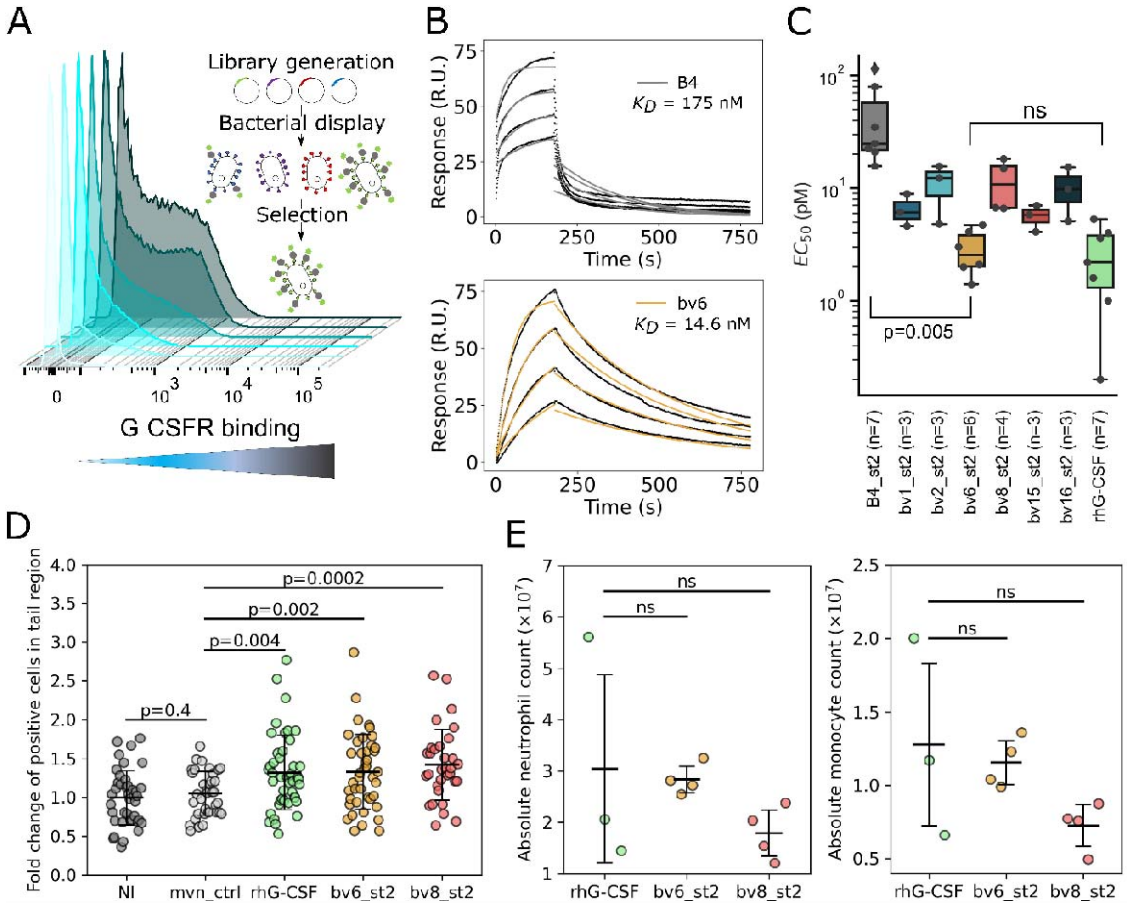

Figure 2. Affinity-enhanced binders exhibit improved granulopoietic activity *in vitro* and *in vivo*. **(A)** Cell sorting of bacterially-displayed Boskar4 mutants bound to fluorescently labeled G-CSFR was conducted over 5 steps of enrichment. Successive fluorescence shifts are shown as light cyan to dark gray distributions. **(B)** SPR titrations show single-domain bv6 to bind 12-fold tighter than its Boskar4 counterpart (Fig. S7D and Table 1). **(C)** Proliferative activity assays in NFS-60 cells showed the enhanced activity (EC_{50}) of all variants in comparison to Boskar4_st2, where the most active variant bv6_st2 was not significantly different in activity compared to the native ligand (rhG-CSF; lightgreen box). For statistical analysis a one-way ANOVA over all samples was performed followed by a Tukey HSD test. Proliferation assays were conducted in at least three ( ) independent experiments per variant or rhG-CSF (Table 1 and Fig. S8). **(D)** Interval plots of the fluorescent neutrophils in transgenic *Tg:mpxGFP* zebrafish larvae that were either not injected (NI), injected with the inactive protein Moevan_control (mvn_ctrl) [49], rhG-CSF, or indicated Boskar4 variants (bv6_st2 or bv8_st2) after 24 h of treatment. Data shows mean ± standard deviation, where each circle represents one zebrafish larva (NI n=40, mvn_ctr n=35, rhG-CSF n=44, bv6_st2 n=42, bv8_st2 n=32). Statistical analysis was carried out by ordinary one-way ANOVA followed by a Tukey HSD test. **(E)** C57BL/6 Ly5.1 mice were treated (i.p.) with rhG-CSF, bv6_st2, or bv8_st2 (each circle indicates one mouse). Absolute cell counts of mouse neutrophils ($DAPI^-CD45^+Ly6G^+Ly6C^+$, left image) and monocytes ($DAPI^-CD45^+CD19^-CD3^-CD11b^+Ly6C^+Ly6G^-$, right image) in the bone marrow of treated mice are shown. Statistical analysis was carried out by ordinary one-way ANOVA with a multiple comparisons test of all experimental drugs to the G-CSF as a positive control (rhG-CSF, bv6_st2 n=4, bv8_st2 n=4; ns: not significant).

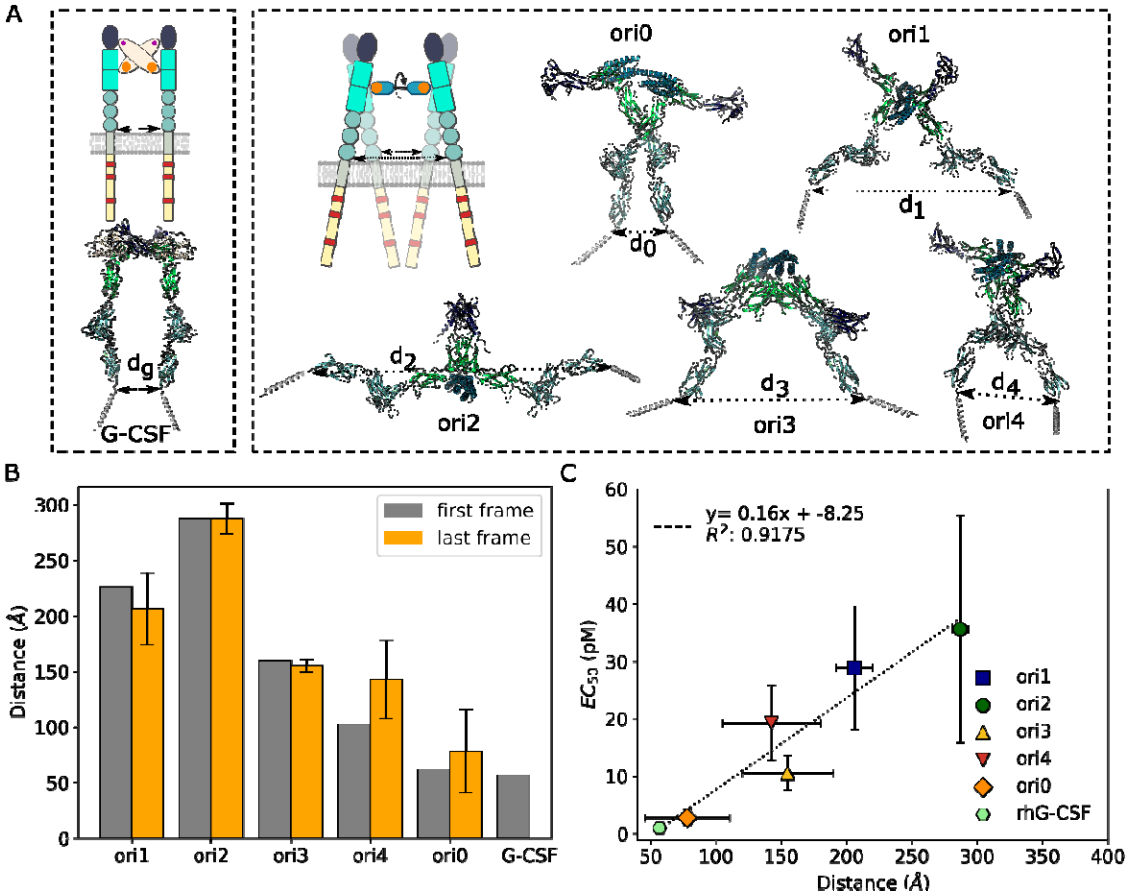

Figure 3. Agonists designed to associate G-CSFR in non-native dimeric geometries yield distinct cell activation potencies. (A) Unlike the native 2:2 ligand-receptor assembly induced by G-CSF (PDB: 2D9Q), we developed a range of novel ligands by rigidly connecting two copies of the affinity-enhanced bv6 module (Materials and Methods; Fig. S11) that form 1:2 ligand-receptor complexes. Modeled complexes of these orientation-rigging designs (ori0 through ori4) and G-CSFR indicate varying transmembrane domain spacings (d_x). Ori0 was designed to closely mimic this distance parameter to that of G-CSF (i.e., $d_0 \approx d_g$). **(B)** Molecular dynamics simulations performed on a selected set of designed ori candidates confirmed the rigidity of the design linkers. Orange bars represent the mean spacing and its standard deviation from 5 simulation replicas. **(C)** Proliferation assays in NFS-60 cells of the five selected ori designs and rhG-CSF (Lenograstim) showed the proliferative EC_{50} (mean and standard deviation of at least 5 independent experiments) to strongly correlate to the modelled transmembrane domain spacing (d_x) for the different proteins. The dotted line represents the linear fit between the obtained EC_{50} and the distances of the last frame (where the d_g of G-CSF was obtained as a single value from the crystal structure (PDB:2D9Q).

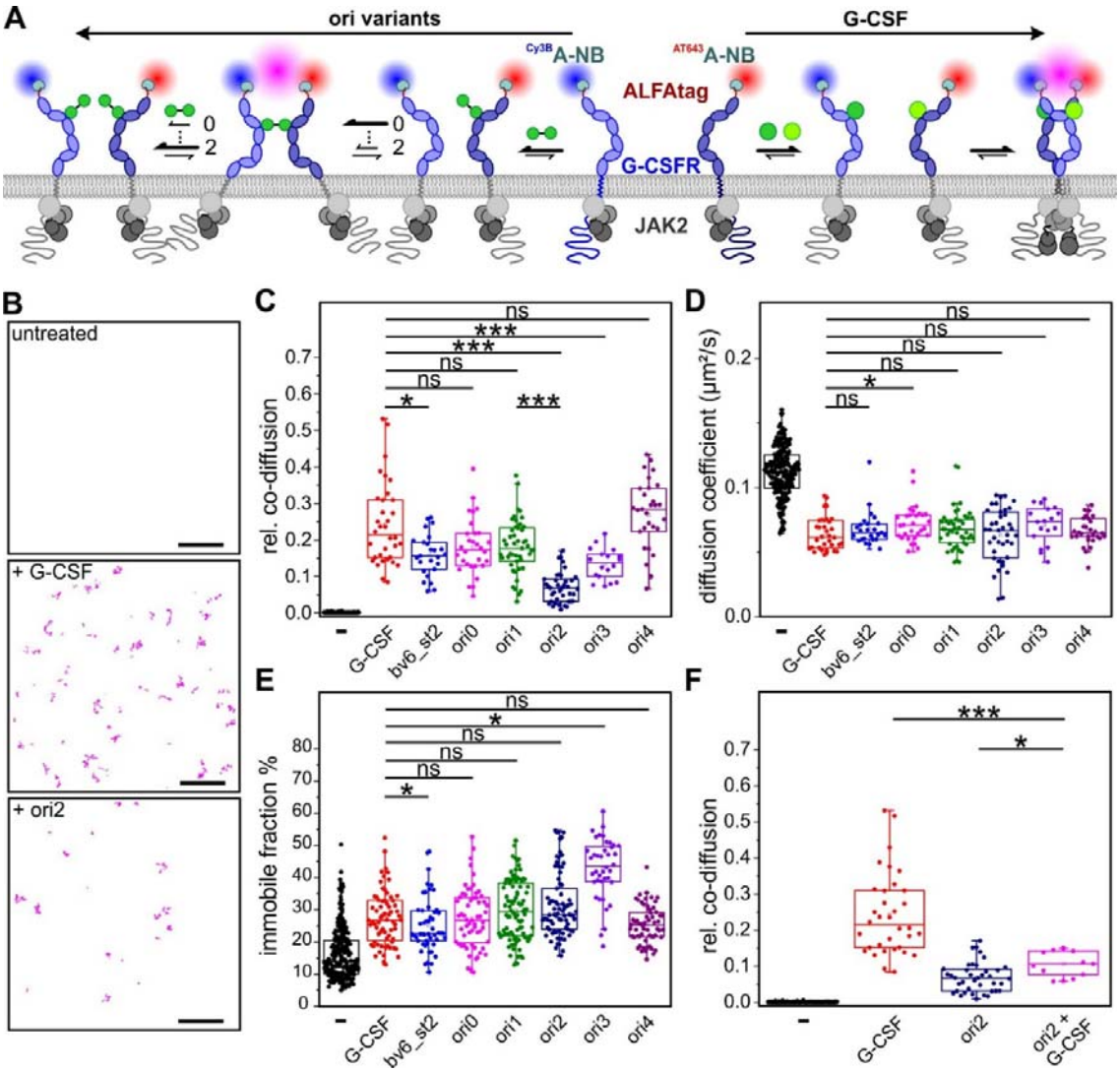

Figure 4. The design agonists differentially dimerize G-CSFR subunits in live cells. (A, B) Dual-color single molecule co-tracking for quantifying G-CSFR dimerization in live cells. **(A)** G-CSFR labeled via an N-terminal ALFA-tag using a mixture of nanobodies conjugated with Cy3B and AT643, respectively. The G-CSFR monomer-dimer equilibrium probed by dual-color single molecule co-tracking depends on the two-dimensional and three-dimensional binding affinities of the respective design agonist. Different dimerization principles by G-CSF (arrow to the right) and design agonists arrow to the left), as well as the consequences of altered orientation on the assembly kinetics are schematically outlined. (numbers on arrows indicate expected impact of ori0 (0) or ori2 (2) **(B)** Typical single molecule co-trajectories of G-CSFR in the absence of agonist and presence of G-CSF and ori0, respectively. A ROI from a single cell is shown. Scale bar: 5 µm. **(C)** Relative dimerization levels of G-CSFR in the absence of ligand and in the presence of G-CSF and design agonists. **(D)** Diffusion constants of G-CSFR monomers in the absence of ligand compared to G-CSFR dimers in the presence of G-CSF and design agonists identified by co-tracking analysis. **(E)** Comparison of the immobile fraction of G-CSFR in the absence of ligand and in the presence of G-CSF and design agonists. **(F)** Comparison of G-CSFR dimerization by G-CSFR by G-CSF, ori2 and an equimolar mixture of both. Box plots in C-F were obtained from analysis of multiple cells (For C-E; Numbers of cells and experiments, respectively, are 124 and 17, 34 and 3, 25 and 2, 30 and 2, 47 and 3, 39 and 3, 18 and 2, 30 and 2 for each column, going from left to right. For F; Numbers of cells and experiments, respectively, are 124 and 17, 34 and 3, 39 and 3, 10 and 1 for each column, going from left to right), with each dot representing the result from one cell. Box plots indicate data distribution of the second

and third quartiles (box), median (line), mean (square) and 1.5× interquartile range (whiskers). Statistics were performed using two sided two-sample Kolmogorov-Smirnov test (not significant: ns;*$P \leq 0.05$***$P \leq 0.001$)

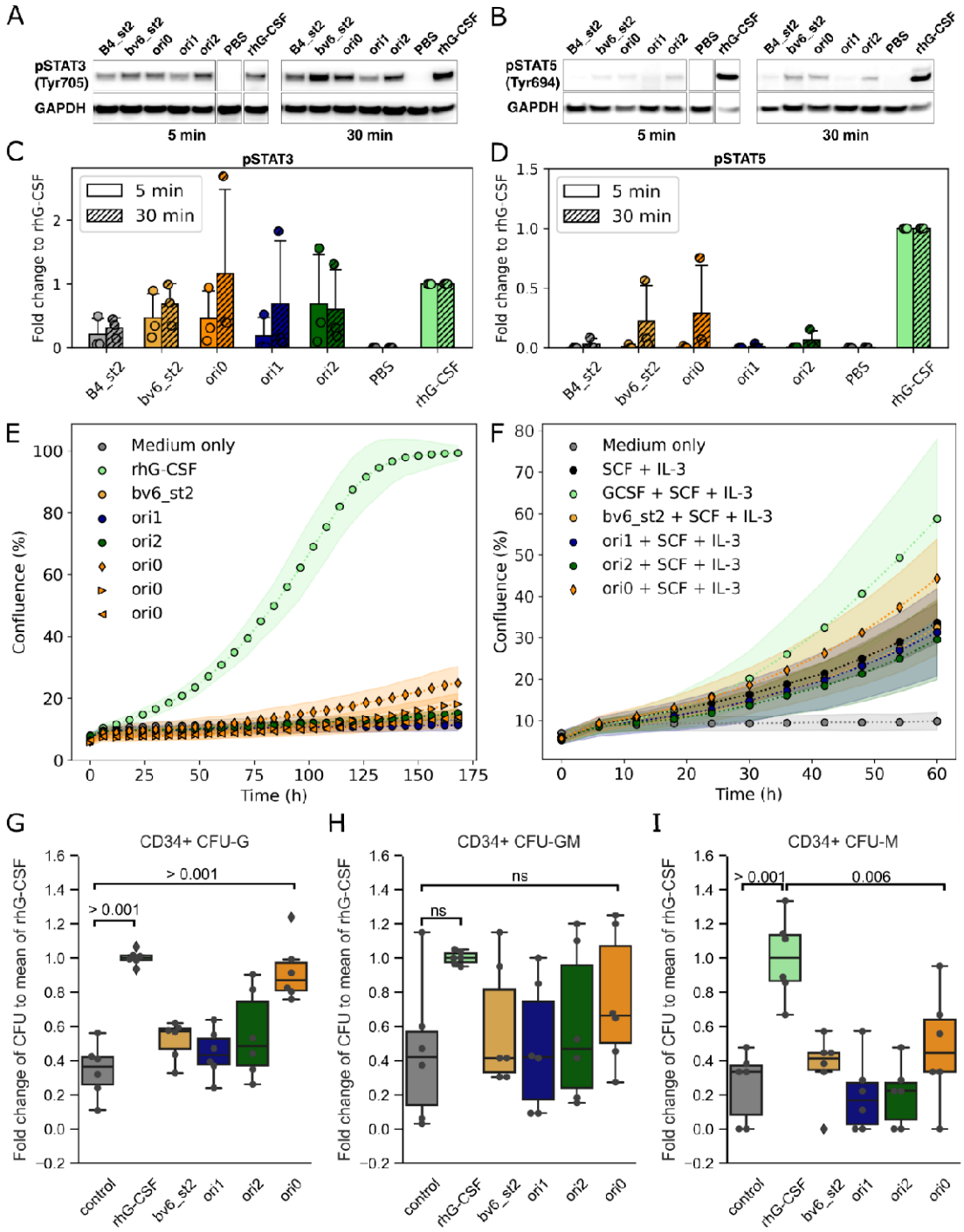

Figure 5. The affinity and geometry of the design agonists bias intracellular signaling and primary stem cell differentiation. (A, B) Representative western blot images of intracellular levels of phospho-STAT3 (Tyr705) and STAT3 (A) and phospho-STAT5 (Tyr694) and STAT5 (B) proteins after treatment of NFS-60 cells with 1 nM of different designs (saturating conditions) for 5 min (left pane) or 30 min (right pane). Glyceraldehyde 3-phosphate dehydrogenase (GAPDH) staining was used as a loading control. Three biological replicates of this experiment showed the same trend (Fig. S17). **(C, D)** The pSTAT3 and pSTAT5 levels were quantified after 5 min and 30 min from those replicates and are represented in (C) and (D), respectively. Shown is the fold change to the GAPDH normalized rhG-CSF signal. **(E, F)** To probe the effect of the agonist designs (100 ng/ml) and rhG-

CSF (10 ng/ml) on healthy donor´s $CD34^+$ HSPCs, proliferation assays were performed without (E) or with the addition of 50 ng/mL SCF and 20 ng/mL IL-3 (F). Ori0 without SCF and IL-3 was tested at three concentrations 100 ng/mL (diamond), 10 ng/mL (triangle-right), and 1 ng/mL (triangle-left). Shown is the mean (points) and standard deviation (shades) of three parallel replicates. **(G, H, I)** Additionally, we performed CFU assays of healthy donor´s $CD34^+$ HSPCs incubated on semi-solid medium supplemented with corresponding cytokines and design agonists. Shown is the fold change to rhG-CSF of the quantified colony-forming units (CFU) of granulocytes (G-CFU) (G), granulocyte-macrophages (GM-CFU) (H), and macrophages (M-CFU) (I). The circles represent the obtained values for each condition of three independent experiments with two parallel replicates each. The indicated p-values were estimated by an ordinary one-way ANOVA followed by a Tukey HSD test.

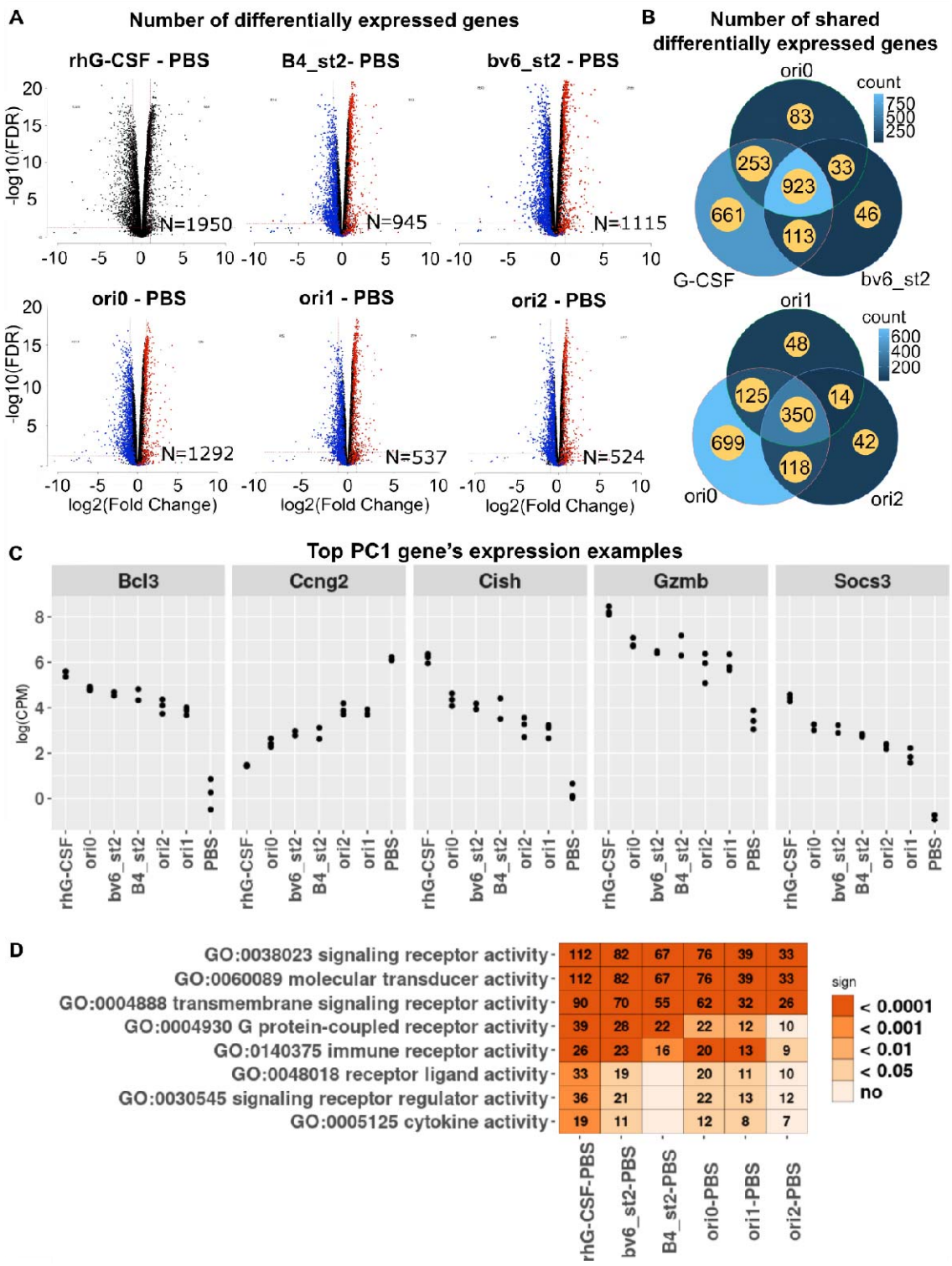

Figure 6. The design agonists regulate the key target genes to varying degrees. (A) The number (N) of differentially expressed genes in NFS-60 cells after treatment with rhG-CSF or different designs compared to PBS treated control. Blue (downregulated genes) and red (upregulated genes) dots in the volcano plots indicate genes that are shared between the corresponding design and rhG-CSF. **(B)** The Venn diagrams show the numbers of shared and design-specific regulated genes. **(C)** Examples of the top 20 differentially expressed hematopoiesis-related genes in the first principal

component (PC1) of the principal component analysis (PCA). **(D)** Gene Ontology (GO) analysis of significantly regulated signaling pathways in the indicated groups. Each number indicates the number of differentially expressed genes related to the corresponding pathway.

Tables

Table 1. Binding affinity and activity parameters determined for G-CSFR modulators. The association rate constant (k_a), the dissociation rate constant (k_d) and the apparent equilibrium dissociation constant (K_D) were obtained by surface plasmon resonance (SPR) against immobilized hG-CSF receptor (compare Fig. S6, S7, and S14). The mean and standard deviation (sd) of the half-maximal effective concentration EC_{50} (pM) was obtained from NFS-60 activity assays of at least 3 biological replicates (compare Fig. S8 and S15). * The SPR parameters of rhG-CSF (self-made purified from *E. coli*) were taken from Skokowa *et al.* 2022 [42].

	k_a (M^{-1} s^{-1})	k_d (s^{-1})	Apparent K_D (M)	Chi² (RU²)	EC_{50} (pM) mean ± sd
Boskar4	$(3.4 \pm 1.7) \times 10^{4}$	$(5.4 \pm 1.4) \times 10^{-3}$	$(1.7 \pm 0.4) \times 10^{-7}$	13.9	NA
bv6	$(2.4 \pm 0.7) \times 10^{5}$	$(3.3 \pm 0.4) \times 10^{-3}$	$(1.4 \pm 0.2) \times 10^{-8}$	2.51	NA
Boskar4_st2	$(2.3 \pm 1.0) \times 10^{6}$	$(3.3 \pm 0.7) \times 10^{-3}$	$(1.6 \pm 0.3) \times 10^{-9}$	0.678	33.1 ± 23.6
bv1_st2	$(9.7 \pm 2.0) \times 10^{5}$	$(2.2 \pm 0.2) \times 10^{-4}$	$(2.4 \pm 0.6) \times 10^{-10}$	1.44	6.5 ± 2.2
bv2_st2	$(3.5 \pm 1.3) \times 10^{5}$	$(1.7 \pm 0.1) \times 10^{-4}$	$(5.3 \pm 1.8) \times 10^{-10}$	0.371	10.9 ± 5.5
bv6_st2	$(4.9 \pm 0.9) \times 10^{5}$	$(5.9 \pm 0.5) \times 10^{-4}$	$(6.4 \pm 1.0) \times 10^{-10}$	1.16	2.9 ± 1.3
bv8_st2	$(1.8 \pm 0.4) \times 10^{6}$	$(1.5 \pm 0.1) \times 10^{-3}$	$(8.3 \pm 1.6) \times 10^{-10}$	1.36	11.6 ± 5.9
bv15_st2	$(7.4 \pm 5.0) \times 10^{5}$	$(4.0 \pm 0.1) \times 10^{-4}$	$(6.5 \pm 2.1) \times 10^{-10}$	0.982	5.6 ± 1.5
bv16_st2	$(8.1 \pm 0.1) \times 10^{5}$	$(7.1 \pm 0.8) \times 10^{-4}$	$(8.8 \pm 1.2) \times 10^{-10}$	0.473	10.1 ± 5.1
rhG-CSF (self-made from *E. coli*)*	$(3.0 \pm 0.3) \times 10^{5}$	$(4.9 \pm 2.8) \times 10^{-4}$	$(1.1 \pm 1.6) \times 10^{-9}$	4.9	2.6 ± 1.8
Lenograstim (Glycosylated, commercial rhG-CSF)	NA	NA	NA	NA	1.0 ± 0.7
ori0	$(6.5 \pm 6.6) \times 10^{5}$	$(2.5 \pm 0.8) \times 10^{-4}$	$(5.6 \pm 2.4) \times 10^{-10}$	1.11	2.8 ± 1.4
ori1	$(1.4 \pm 2.1) \times 10^{6}$	$(1.2 \pm 0.3) \times 10^{-4}$	$(3.6 \pm 2.8) \times 10^{-10}$	0.779	28.9 ± 0.7
ori2	$(1.1 \pm 0.8) \times 10^{5}$	$(4.6 \pm 1.3) \times 10^{-5}$	$(3.4 \pm 1.6) \times 10^{-10}$	2.83	35.6 ± 19.8
ori3	$(8.7 \pm 5.9) \times 10^{5}$	$(2.5 \pm 0.1) \times 10^{-4}$	$(4.1 \pm 0.1) \times 10^{-10}$	2.36	10.6 ± 3.0
ori4	$(1.2 \pm 0.1) \times 10^{5}$	$(7.6 \pm 1.4) \times 10^{-5}$	$(6.4 \pm 1.14) \times 10^{-10}$	1.37	19.3 ± 6.5

Supplementary Figures

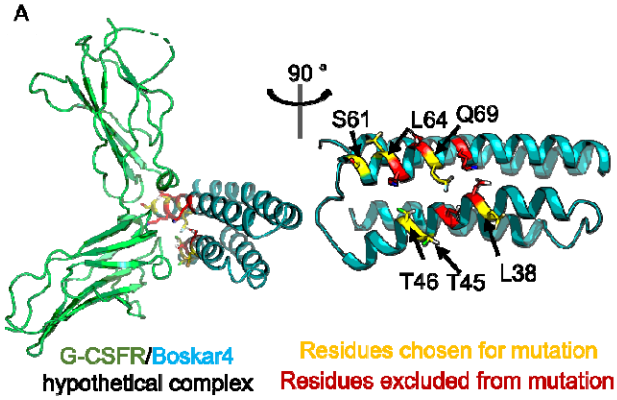

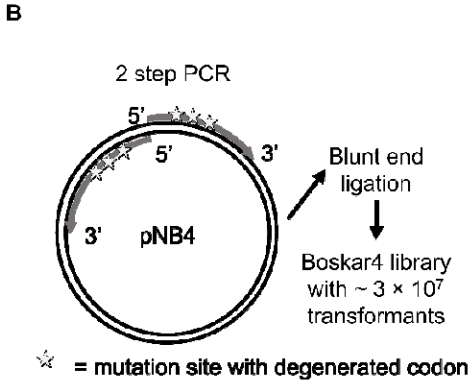

C

Boskar4 saturation library

Position (in 7NY0)	Codons (reverse complement)	Coded amino acids
L38	NDT (AHN)	F, L, I, V, Y, H, N, D, C, R, S, G
T45	NNT (ANN)	F, L, I, V, S, P, T, A, Y, H, N, D, C, R, G
T46	NNT (ANN)	F, L, I, V, S, P, T, A, Y, H, N, D, C, R, G
S61	NDT	F, L, I, V, Y, H, N, D, C, R, S, G
L64	NDT	F, L, I, V, Y, H, N, D, C, R, S, G
Q69	VDG	L, M, V, Q, K, E, R, G

Theoretical diversity	4.0E+06
Amino-acid diversity	3.1E+06
Total transformants	3.5E+07

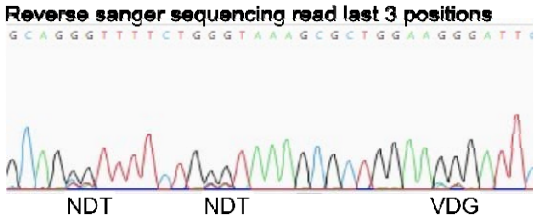

D

Boskar4 library designed with Damletta

Position (in 7NY0)	aa lowest energy change	Codons (reverse complement)	Present
L38	R, F, L, N, I	CKA, WWC (TMG, GWW)	F(*) I(*) L(*) N(*) R(*) Y(0)
T45	Y, F, R, N, H	HNC (GND)	C(0) F(*) H(*) I(0) L(0) N(*) P(0) R(*) S(0) T(*) Y(*)
T46	N, L, D, I, S	RAC, WYA (GTY, TRW)	D(*) I(*) L(*) N(*) S(*) T(*)
S61	F, Y, R, D, N	NDC	C(0) D(*) F(*) G(0) H(0) I(0) L(0) N(*) R(*) S(*) V(0) Y(*)
L64	Y, F, R, H, S	YNC	C(0) F(*) H(*) L(*) P(0) R(*) S(*) Y(*)
Q69	M, K, L, V, I	MWA, RTG	I(*) K(*) L(*) M(*) Q(*) V(*)

Theoretical diversity	2.5E+05
Amino-acid diversity	2.3E+05
Total transformants	2.7E+07

(*) = wanted aa (top 5 aa at the given positions or "wt"-aa) (over all 15.63 %)
(0) = unwanted aa (aa added because of used degeneration)

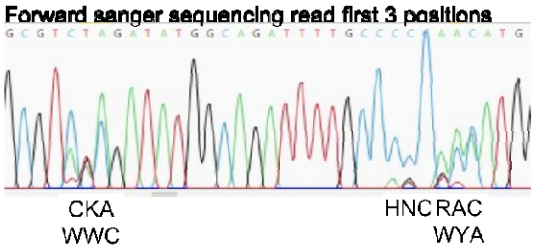

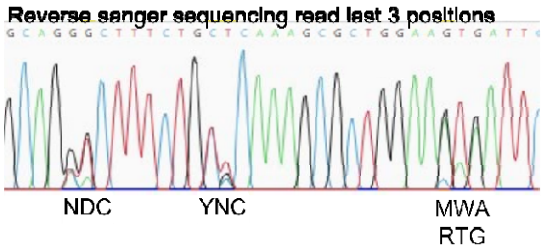

Supplementary Figure 1. (A) Side view on Boskar4 (cyan) in a modeled complex with G-CSFR (green) and detailed view on Boskar4 with marked residues based on 7NY0 considered for mutagenesis (yellow) based on the minimal distance to G-CSFR residues. Residues that were thought

to be critical for G-CSF activity (red) regarding to Young *et al. [44]* were excluded from mutagenesis also if they fulfilled the distance criteria. **(B)** Overview of library generation via degenerated codons and blunt end ligation. **(C)** Overview of the saturation library of Boskar4 for affinity maturation. **(D)** Overview of the Damietta *in silico* designed library of Boskar4 which was estimated from a reduced set of the same residues as the saturation library.

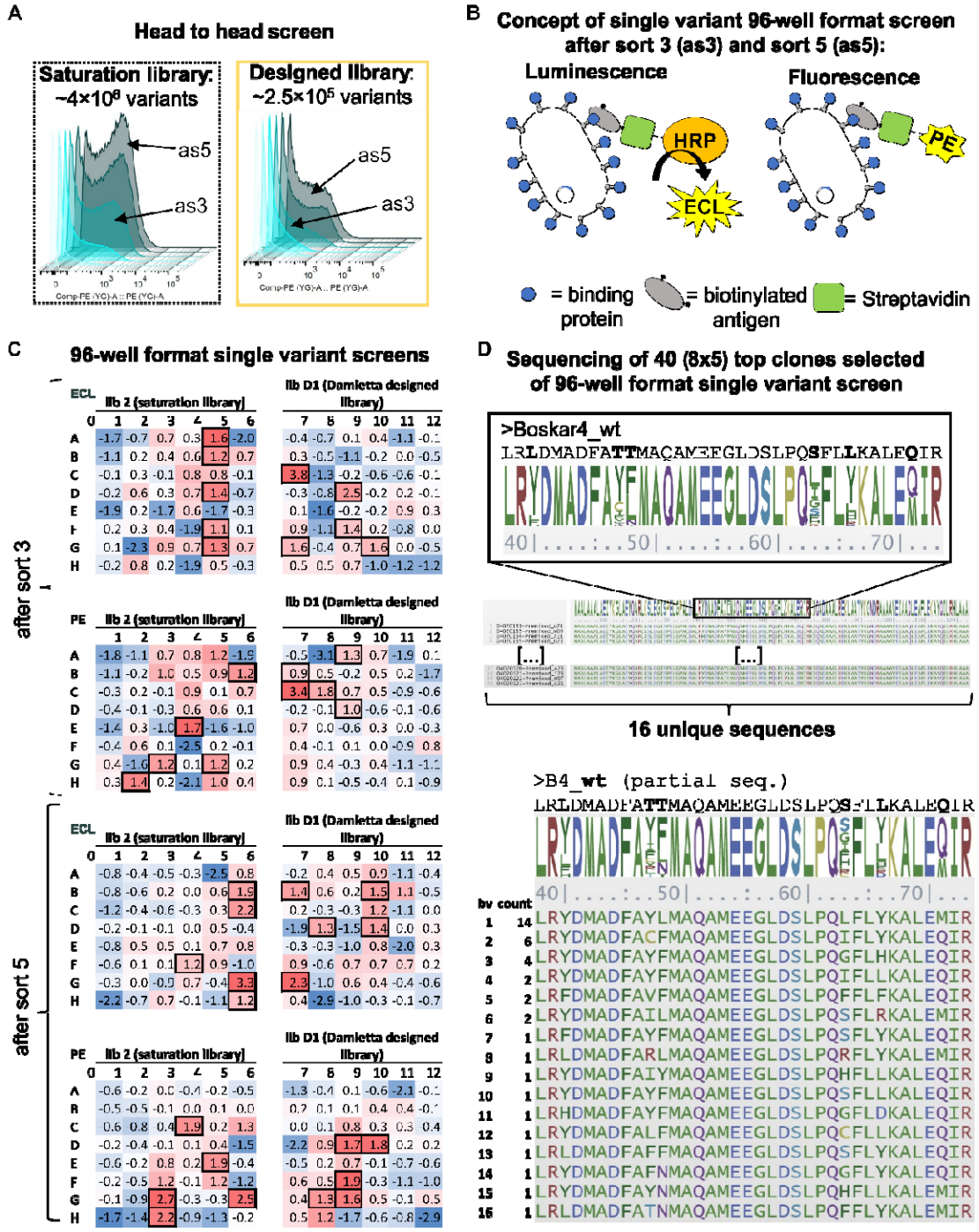

Supplementary Figure 2. (A) Fluorescence measured with FACS of bacteria carrying either the saturation library (dotted line) or the Damietta designed library (light orange) over 5 steps of enrichment (light cyan to dark gray) in a head-to-head screening experiment. **(B)** Concept of single variant 96-well format screen after sort 3 (as3) and sort 5 (as5). Two different readout methods were utilized to estimate the relative binding activity of each variant. Luminescence was applied by a horse radish peroxidase (HRP) avidin conjugate with enhanced chemiluminescence substrate (ECL), and fluorescence was measured by streptavidin phycoerythrin (PE) conjugate. **(C)** Results of the 96-well format single variant screens after enrichment of the library with FACS. Each value corresponds to the z-score given by a single variant (single well on the plate) to all other variants from the same

condition. In total, 8 such screens were made under different conditions (PE or ECL, after sort 3 or after sort 5, saturation or designed library), and top 5 clones of each condition were picked and sequenced. **(D)** Sixteen unique Boskar4 variants (bv1 to bv16) were identified among the 40 analyzed.

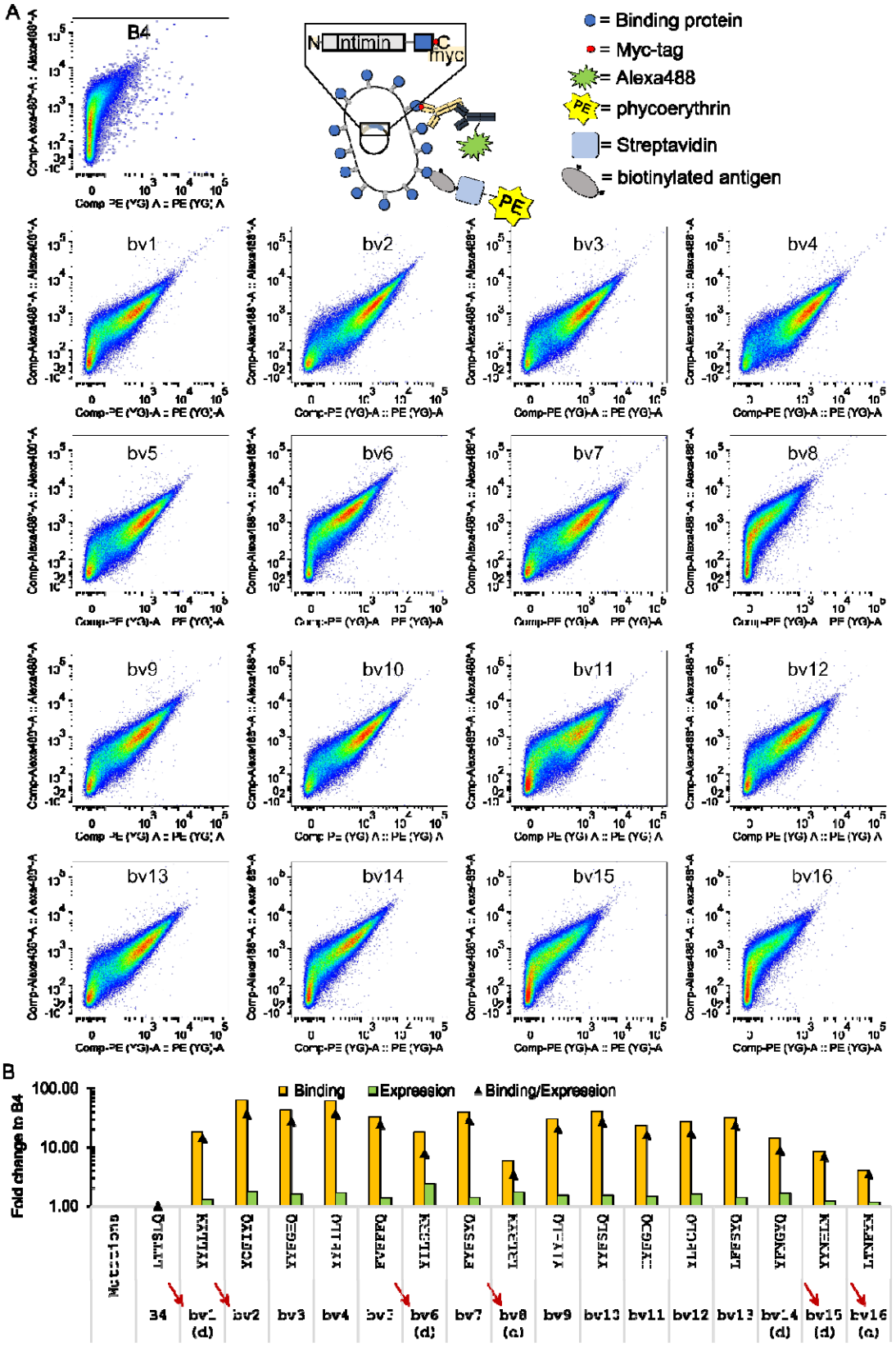
A
B4
N
Intimin
C
myc
= Binding protein
= Myc-tag
= Alexa488
= phycoerythrin
= Streptavidin
= biotinylated antigen
PE
bv1
bv2
bv3
bv4
bv5
bv6
bv7
bv8
bv9
bv10
bv11
bv12
bv13
bv14
bv15
bv16
B
Binding
Expression
Binding/Expression
Fold change to B4
100.00
10.00
1.00
B4
bv1 (d)
bv2
bv3
bv4
bv5
bv6 (d)
bv7
bv8 (c)
bv9
bv10
bv11
bv12
bv13
bv14 (d)
bv15 (d)
bv16 (c)

Supplementary Figure 3. (A) The 16 new affinity-enhanced Boskar4 variants (bv1 to bv16) and Boskar4 (B4) were analyzed on the surface of *E. coli* by FACS for their binding activity to BioGCSFR (10 nM, PE channel) and the expression level of the corresponding variant (anti-myc labeling, Alexa488 channel). **(B)** Based on the measurements in (A) the binding to G-CSFR (orange bars), expression of the binder (green bars), and expression-normalized binding to G-CSFR (black triangles) of the affinity-enhanced Boskar4 variants normalized to Boskar4 was analyzed. Sequences selected for further characterization are marked with dark red arrows. The small "d" in parentheses (d) indicates that the variant was selected from the designed library. Additionally, the corresponding mutation set of each enhanced variant is indicated in comparison to Boskar4.

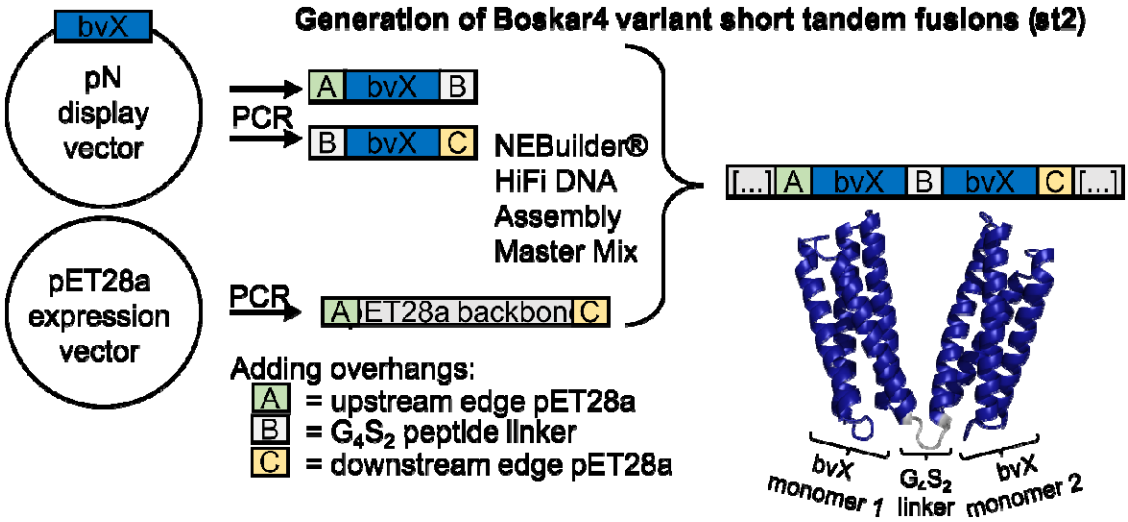

Supplementary Figure 4. The Boskar4 variant short tandem fusions (st2) were generated by the assembly of three fragments consisting of the expression vector, two copies of a Boskar4 variant (bvX) and an overlap including the G_4S_2 peptide linker. The same approach was also used to generate the rigid tandem fusions (ori0 to ori4) by encoding a rigid helix linker instead of a flexible GS-peptide-linker.

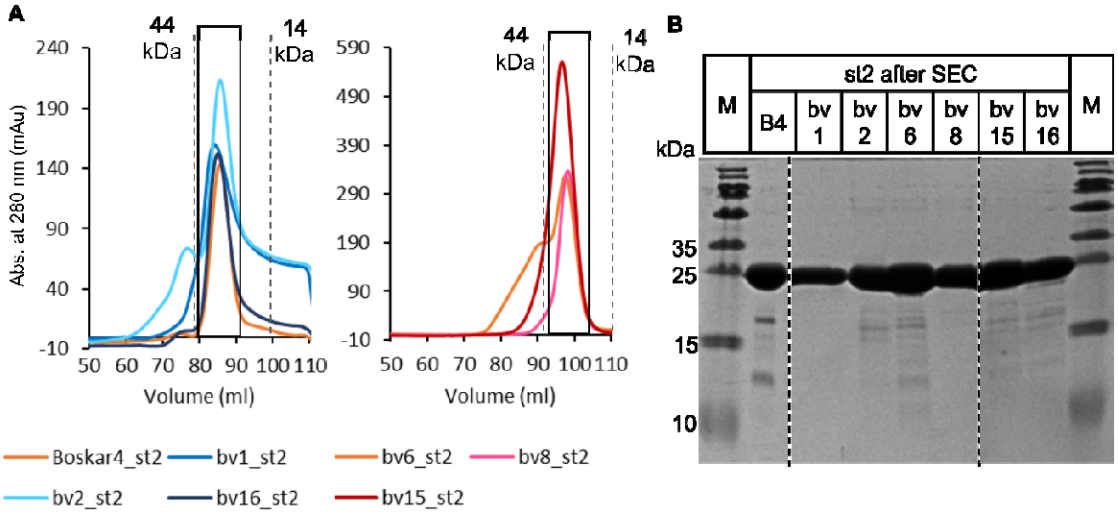

Supplementary Figure 5. (A) Preparative size exclusion chromatography of Boskar4 short tandem fusion (st2) variants after Nickel IMAC on two separate SEC-columns of the same type (HiLoad 16/600, Superdex 200 pg). Dotted lines mark the molecular weight standard for the corresponding column. All fractions of the main peak (black box) were collected and concentrated by ultrafiltration (10 kDa cut-off). **(B)** A representative sample of each protein and a protein molecular weight marker (M) (11852124, Thermo Fisher Scientific) was loaded on a SDS-PAGE (18% PA, 150 V, 1 h) which was subsequently stained with Coomassie. The expected molecular weight of Boskar4_st2 and variants (with not cleaved TEV-cleavage site and His-tag) is ~29 kDa.

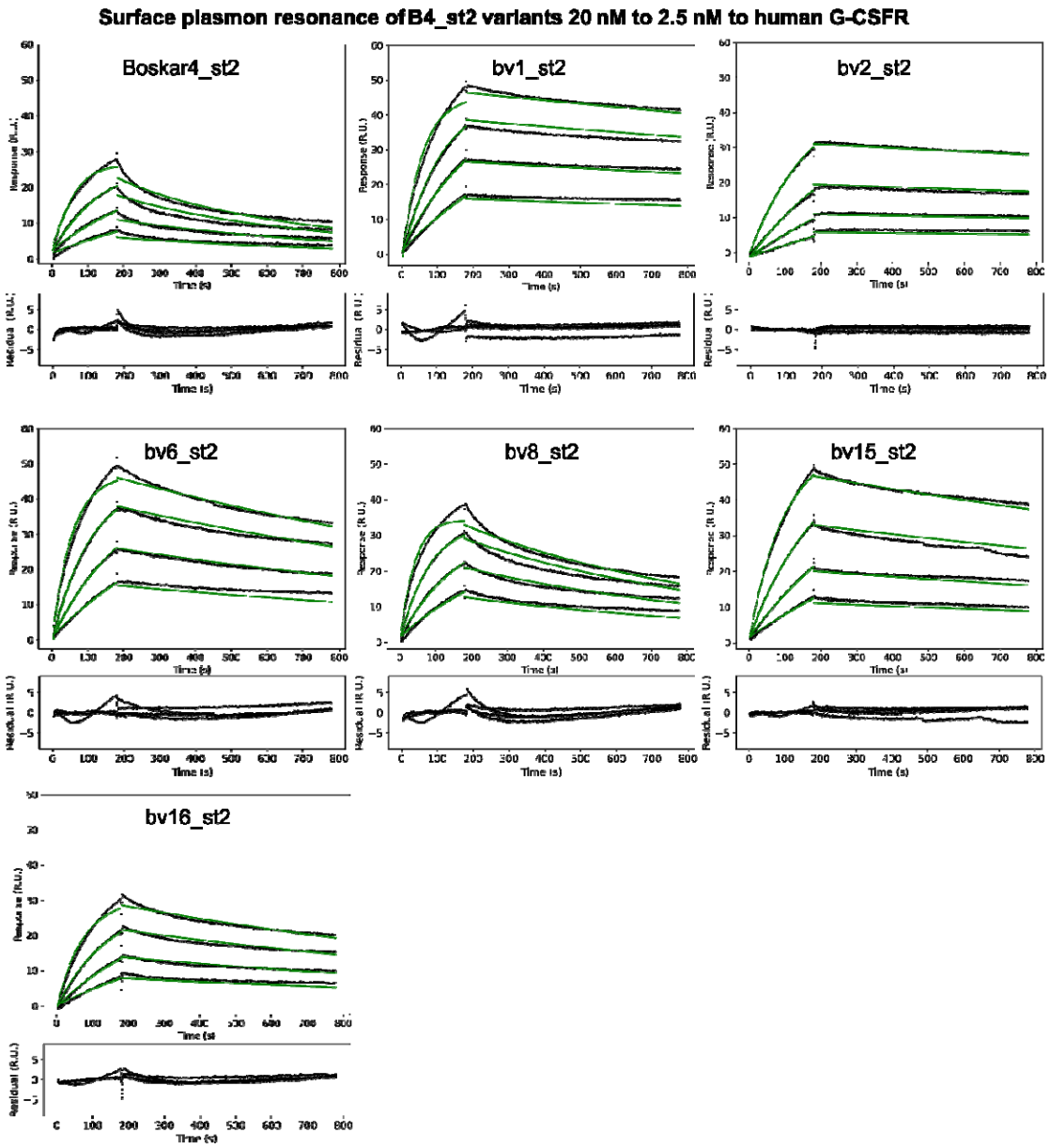

Supplementary Figure 6. Six of the enhanced variants and Boskar4 itself (B4) were chosen to generate short tandem fusions (st2) and measured with surface plasmon resonance (SPR) against immobilized hG-CSFR. The association rate constant (k_a), the dissociation rate constant (k_d), and the apparent equilibrium dissociation constant (K_D) were estimated from the corresponding fits (green lines) of a two-fold titration series from 20 nM to 2.5 nM (compare Table 1).

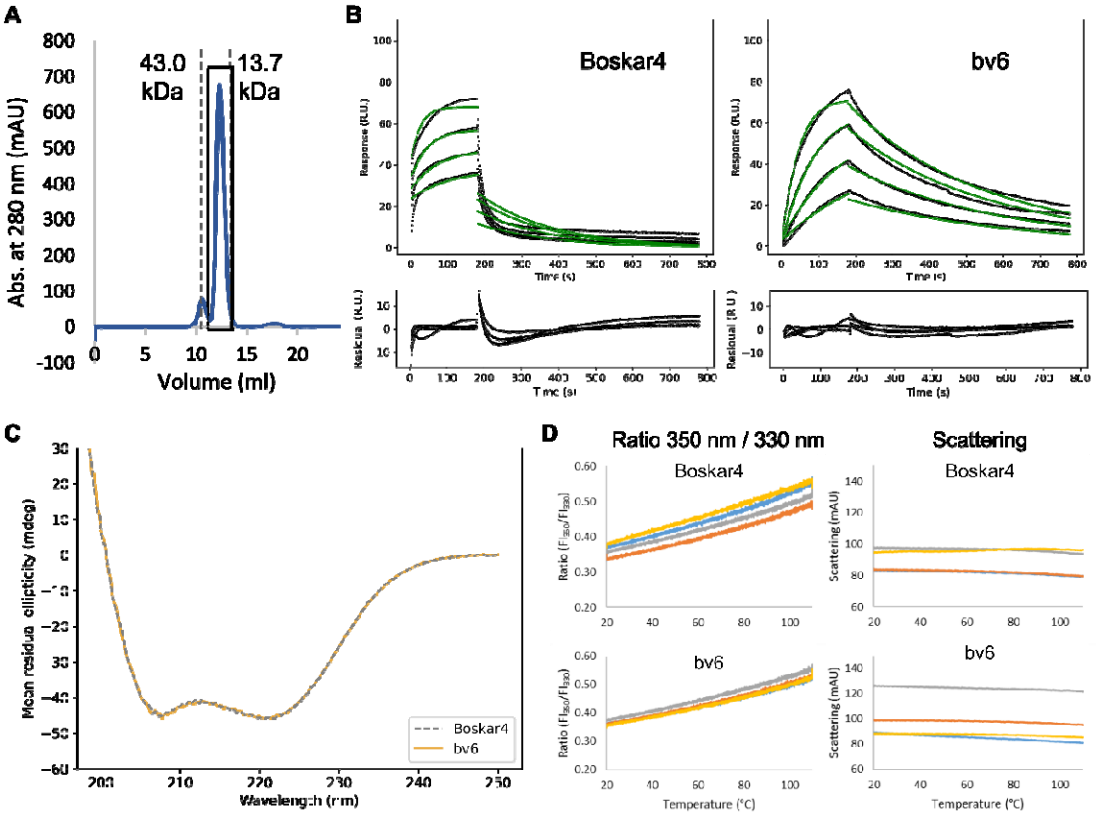

Supplementary Figure 7. **(A)** Preparative size exclusion chromatography of monomeric bv6 on a Superdex® 75 10/300 GL with an expected size of ~15 kDa. Dotted lines mark the molecular weight standard for the corresponding column. All fractions of the main peak (black box) were collected and concentrated by ultrafiltration (10 kDa cut-off). **(B)** Surface plasmon resonance measurement (black line) and the corresponding fit (green lines) of a two-fold dilution series of monomeric Boskar4 and the variant bv6. The highest concentration used for Boskar4 was 1250 nM and for bv6 125 nM. The obtained binding parameters are listed in Table 1. **(C)** The single-domain Boskar4 (B4; gray) and an example variant (bv6; orange) were analyzed with circular dichroism and show strong helical signal. **(D)** Thermostability measurement with nanoDSF of 1 mg/mL of monomeric Boskar4 and bv6 with 4 technical replicates, each indicating the proteins to be stable to at least 110 °C.

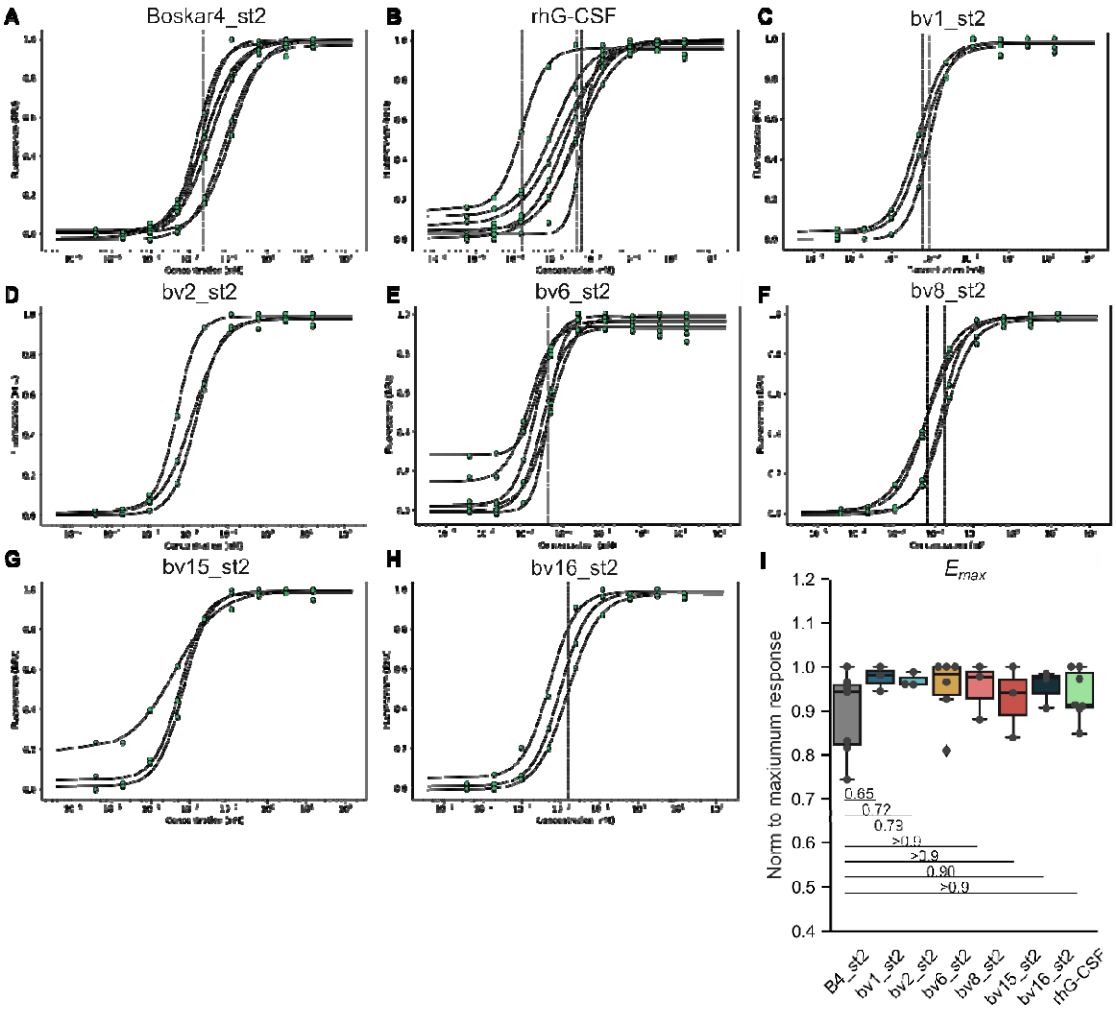

Supplementary Figure 8. (A-H) Dose-response NFS-60 cell proliferation assays to determine the half-maximal effective concentration (EC_{50}) of Boskar4_st2 variants and human recombinant G-CSF (hrG-CSF). The fits to determine the EC_{50} (pM) of at least three independent experiments per G-CSFR agonist are shown (compare also Table 1 and Fig. 2C). **(I)** Maximum proliferative activity (E_{max}) normalized to the maximum response within each independent experiment represented in (A-H). For statistical analysis, an ordinary one-way ANOVA was performed, followed by a Tukey HSD test.

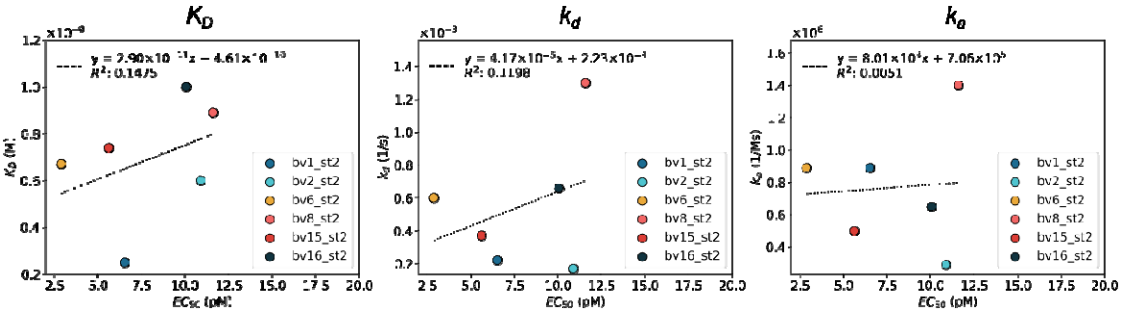

Supplementary Figure 9. Shown is the correlation of a linear fit between the apparent affinity (K_D), association rate constant (k_a) or dissociation rate constant (k_d) and the obtained NFS-60 activity (EC_{50}) for short tandem fusions of Boskar4 (B4) or the affinity-enhanced variants (bv1, bv2, bv6, bv8, bv15, bv6). The coefficient of determination (R^2) is shown in the left upper corner.

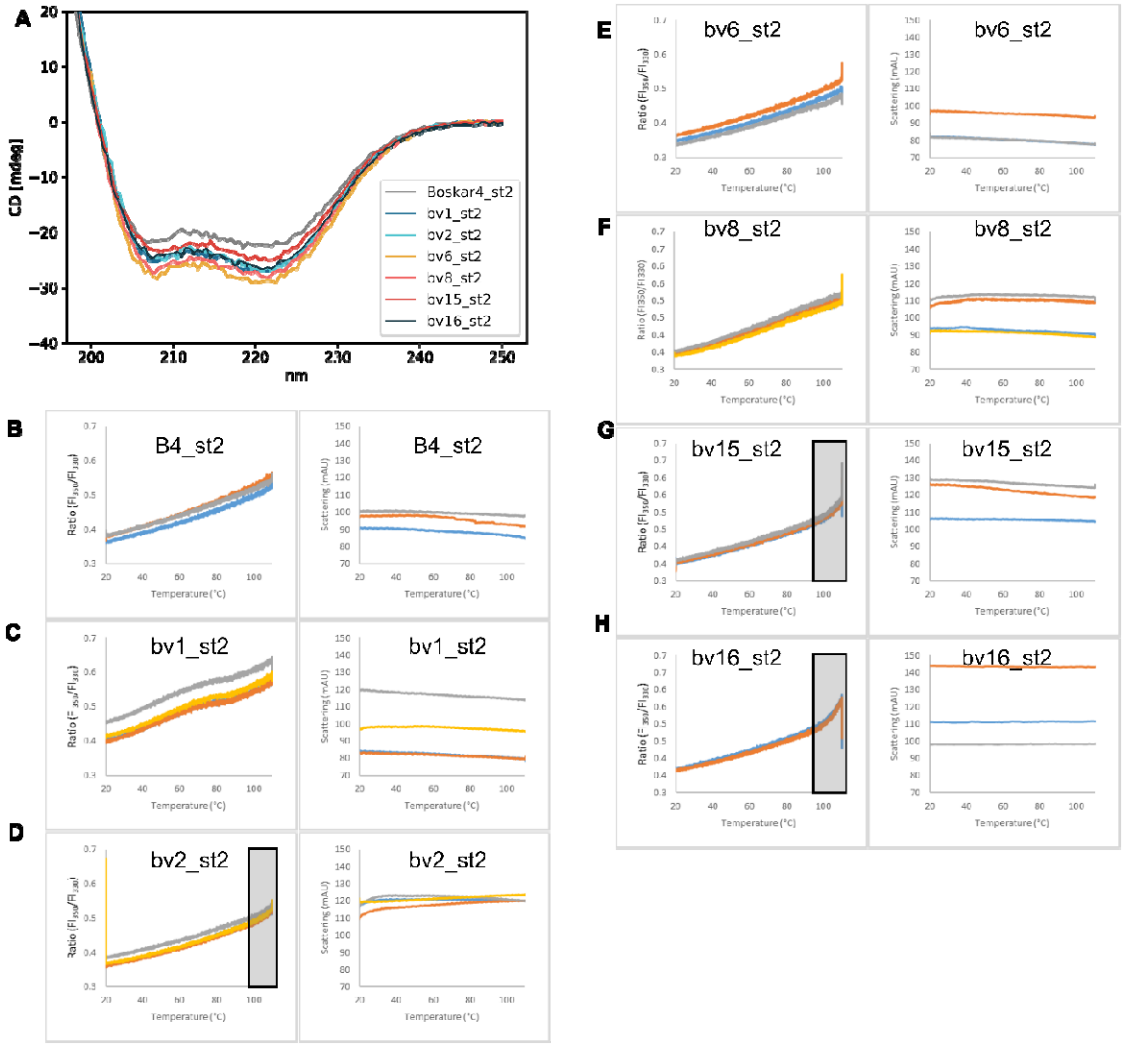

Supplementary Figure 10. (A) Circular dichroism (CD) measurement of Boskar4_st2 and variants (bv1 to bv16) in PBS at 0.1 mg/mL shows expected alpha-helical signal for all samples. **(B-H)** Thermostability measurement with nanoDSF of Boskar4_st2 (B4_st2) and variants (bv1_st2 to bv16_st2) with at least 3 technical replicates. All samples were diluted to 1 mg/mL in PBS, except for bv1_st2, which was used at a concentration 0.5 mg/ml. The gray boxes indicate areas in which a melting onset was observed.

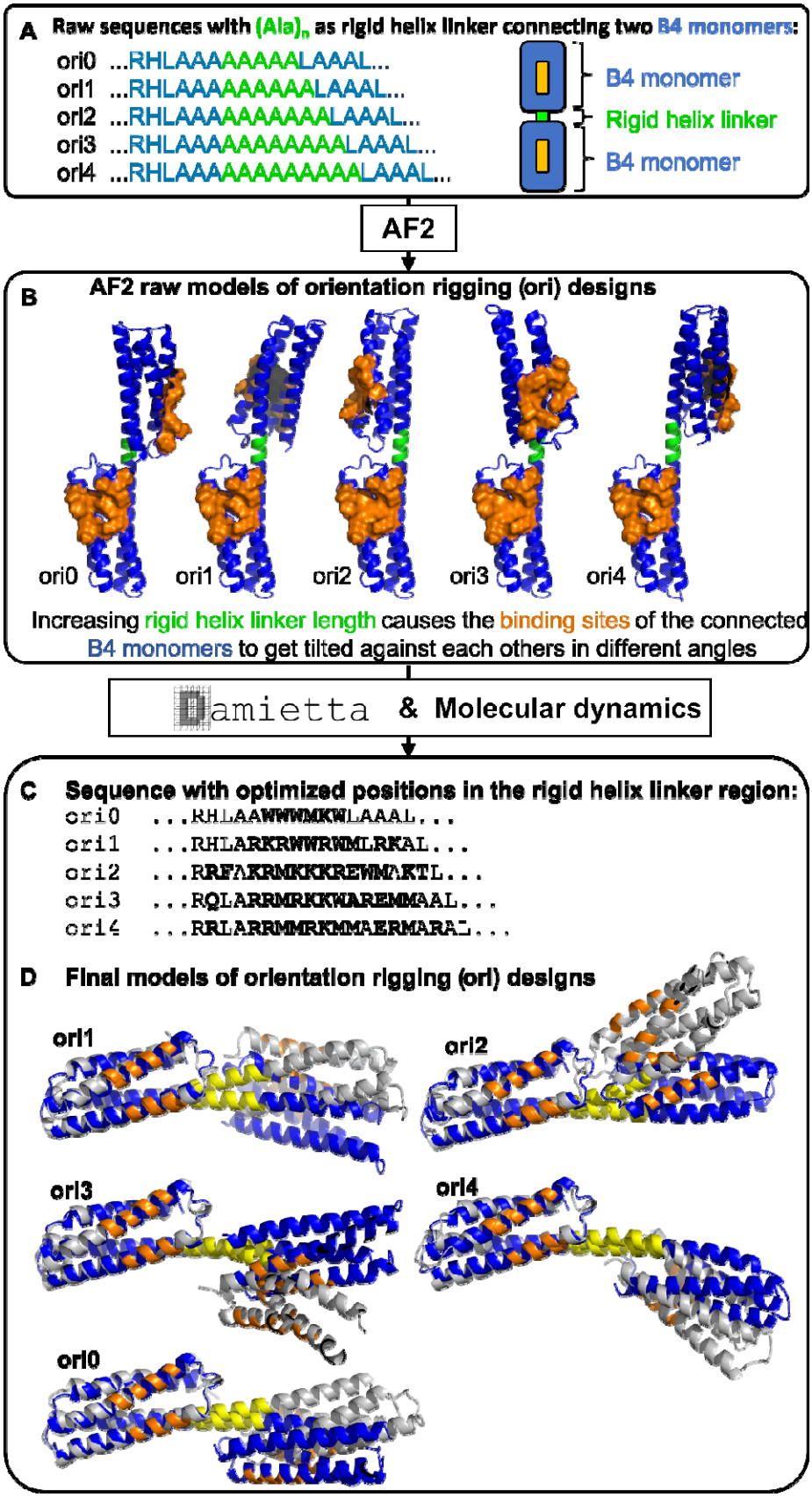
A Raw sequences with (Ala)n as rigid helix linker connecting two B4 monomers:
ori0 ...RHLAAAAAAAALAAAL...
ori1 ...RHLAAAAAAAAALAAAL...
ori2 ...RHLAAAAAAAAAALAAAL...
ori3 ...RHLAAAAAAAAAAALAAAL...
ori4 ...RHLAAAAAAAAAAAALAAAL...
B4 monomer
Rigid helix linker
B4 monomer
AF2
B AF2 raw models of orientation rigging (ori) designs
ori0
ori1
ori2
ori3
ori4
Increasing rigid helix linker length causes the binding sites of the connected B4 monomers to get tilted against each others in different angles
amietta & Molecular dynamics
C Sequence with optimized positions in the rigid helix linker region:
ori0 ...RHLAAWWWMKWLAAAL...
ori1 ...RHLARKRWWRWMLRKAL...
ori2 ...RRFAKRMKKKREWMAKTL...
ori3 ...RQLARRMRKKWAREMMAAL...
ori4 ...RRLARRMMRKMMAERMARAL...
D Final models of orientation rigging (ori) designs
ori1
ori2
ori3
ori4
ori0

Supplementary Figure 11. Generation of the orientation-rigging designs (oris) tuning G-CSFR activity. **(A)** Raw sequence design. **(B)** AlphaFold2 raw models. **(C)** Selected residues (bold) in the rigid helix linker region were optimized with Damietta, and the most stable designs were identified with molecular dynamics (MD). **(D)** The MD input structure of each top hit is displayed in blue, and the last frame of the MD-simulation is indicated in gray. The linker helix area is depicted in yellow, and the G-CSFR binding sites are highlighted in orange.

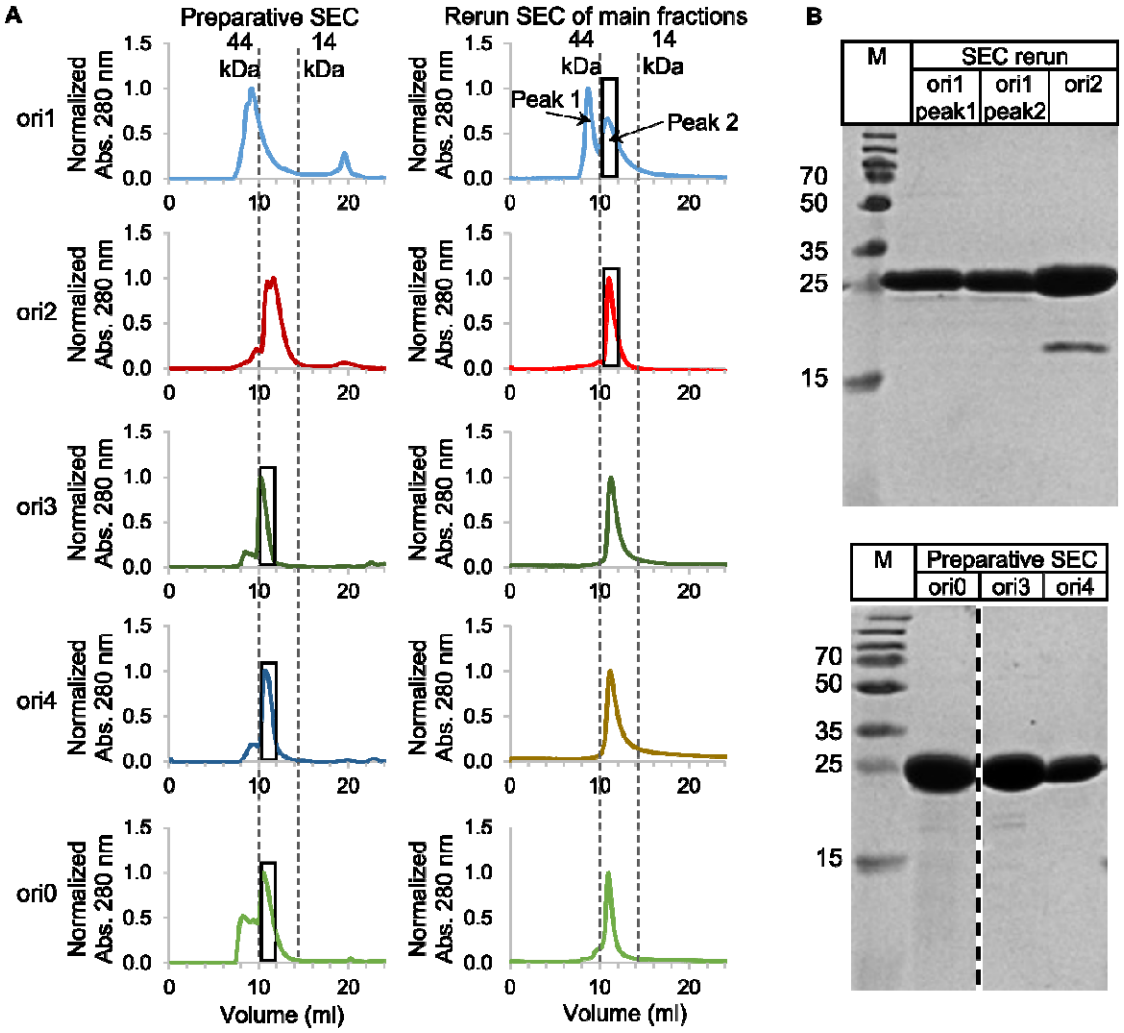

Supplementary Figure 12. (A) Size exclusion chromatography of ori0, ori1, ori2, ori3 and ori4 after Nickel IMAC was performed on a Superdex Increase 75 10/300 GL (Cytiva). The dotted lines mark the molecular weight standard for the corresponding column. All fractions of the main peak were collected and concentrated by ultrafiltration (10 kDa cut-off). Part of the collected fractions were rerun on the same column to validate the purity and correct molecular mass. **(B)** A representative sample of each fraction containing the protein as used for the subsequent experiments (black boxes in (A)) was loaded on a SDS-PAGE. The expected molecular weight of the oris (with uncleaved TEV-cleavage site and His-tag) is ~29 kDa. For ori2, the main fraction was collected after the SEC rerun and for ori1, peak 1 and peak 2 were collected separately. The main fractions after the preparative size exclusion of ori0, ori3 and ori4 were directly used for subsequent experiments.

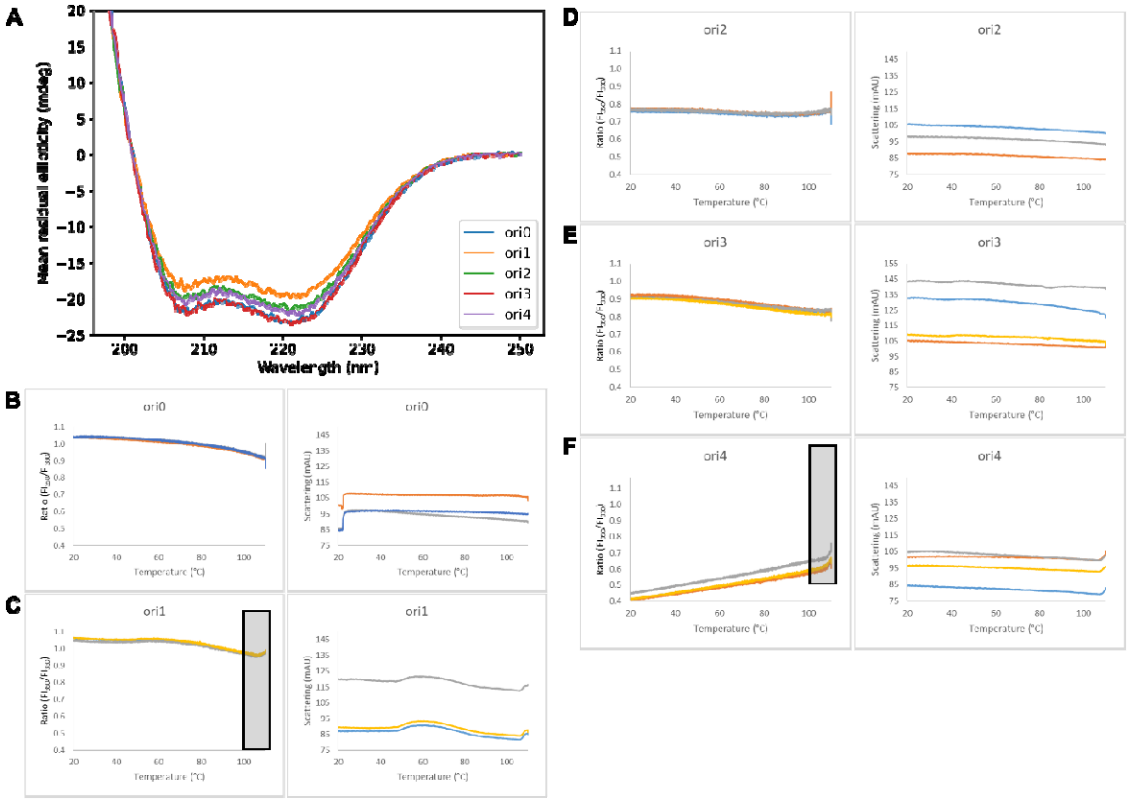

Supplementary Figure 13: (A) Circular dichroism (CD) measurement of ori0, ori1, ori2, ori3 and ori4 in PBS at 0.1 mg/mL showed the expected alpha-helical signal for all samples. **(B-F)** Thermostability measurement with nanoDSF of the rigid tandem fusions (ori0 to ori4) with at least 3 technical replicates. All samples were diluted to 1 mg/mL in PBS. The gray boxes indicate areas in which a melting onset was observed.

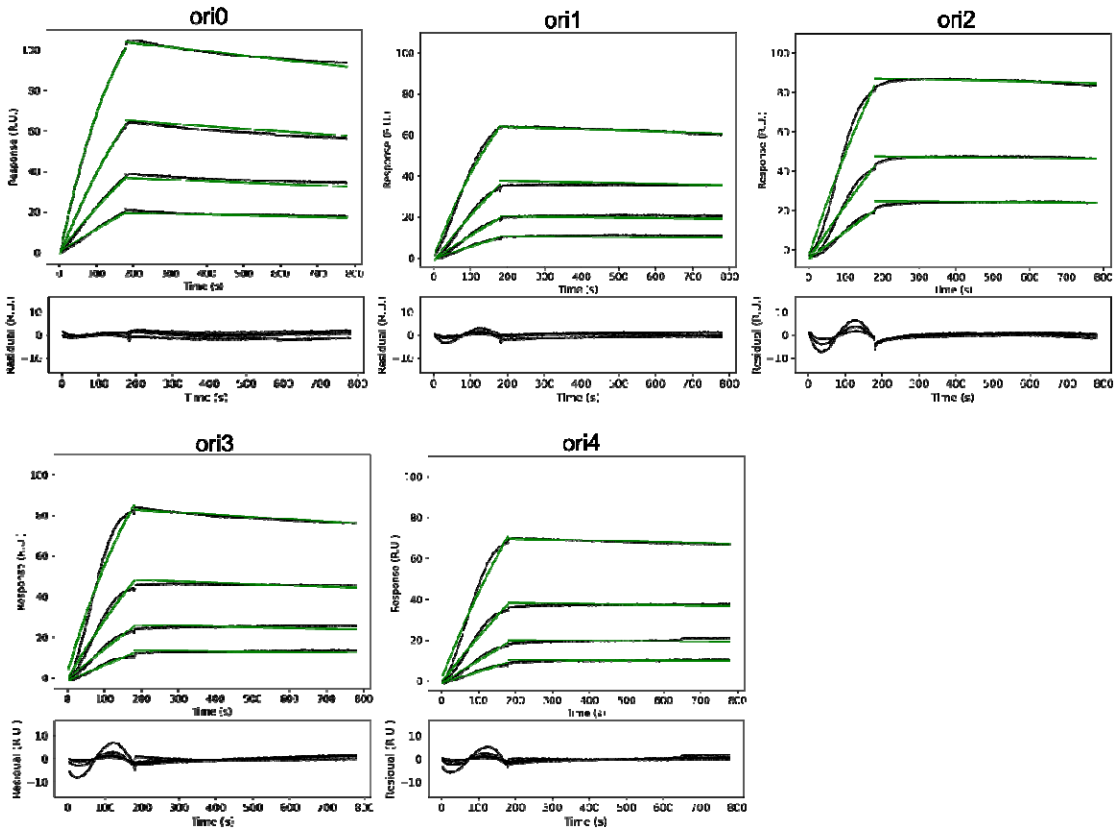

Supplementary Figure 14. Surface plasmon resonance (SPR) measurement of oris against immobilized hG-CSFR. The association rate constant (k_a), the dissociation rate constant (k_d), and the apparent equilibrium dissociation constant (K_D) were estimated from the corresponding fits (green lines) of a titration series ranging from 20 nM to 2.5 nM (compare Table 1).

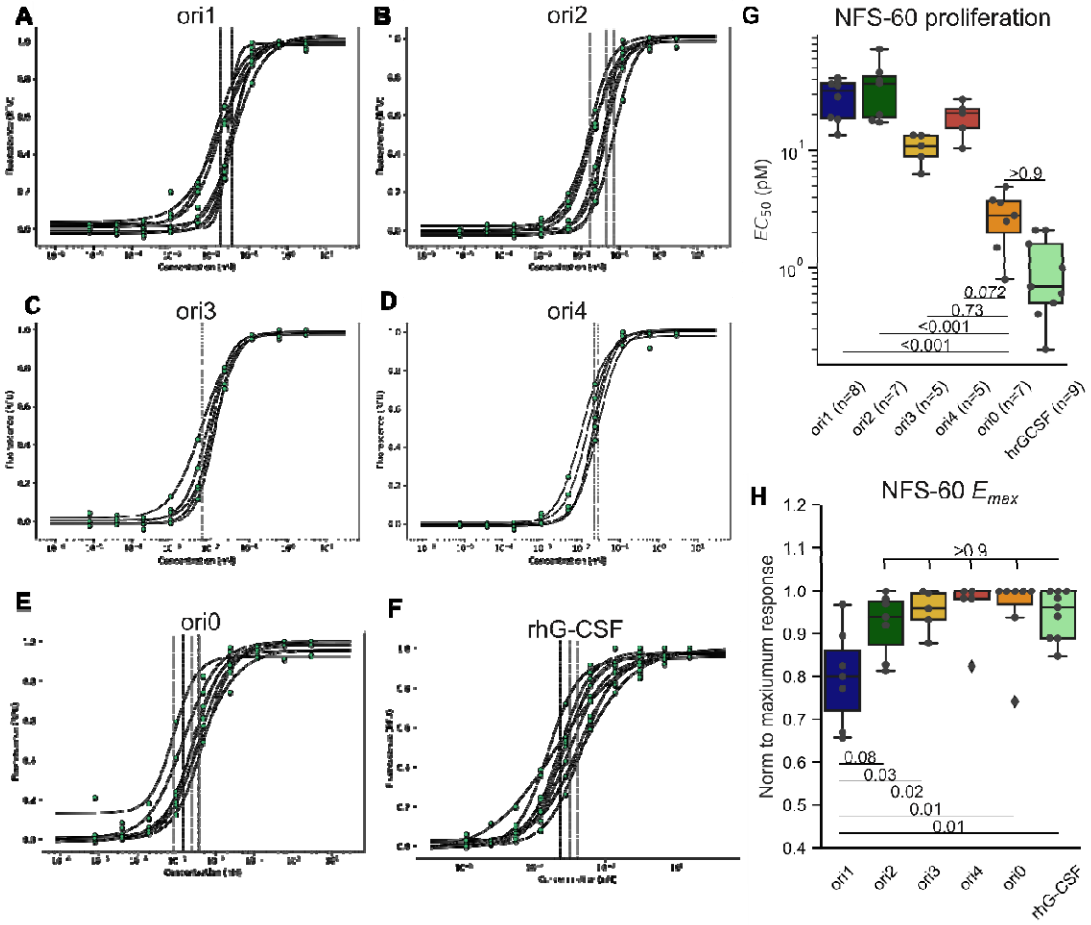

Supplementary Figure 15. (A-F) Dose-response NFS-60 cell proliferation assays to determine the half-maximal effective concentration (EC_{50}) of the oris and G-CSF (rhG-CSF, Lenograstim). Given are the fits to determine the EC_{50} of at least five independent experiments per G-CSFR agonist (compare also Table 1 and Fig. 3C). **(G, H)** Box plot of the EC_{50} (pM) values (G) and the maximum proliferative activity (E_{max}) normalized to the maximum response (H) within each independent experiment represented in (A-F). For statistical analysis in (G) and (H), ordinary one-way ANOVA, followed by a Tukey HSD test was performed.

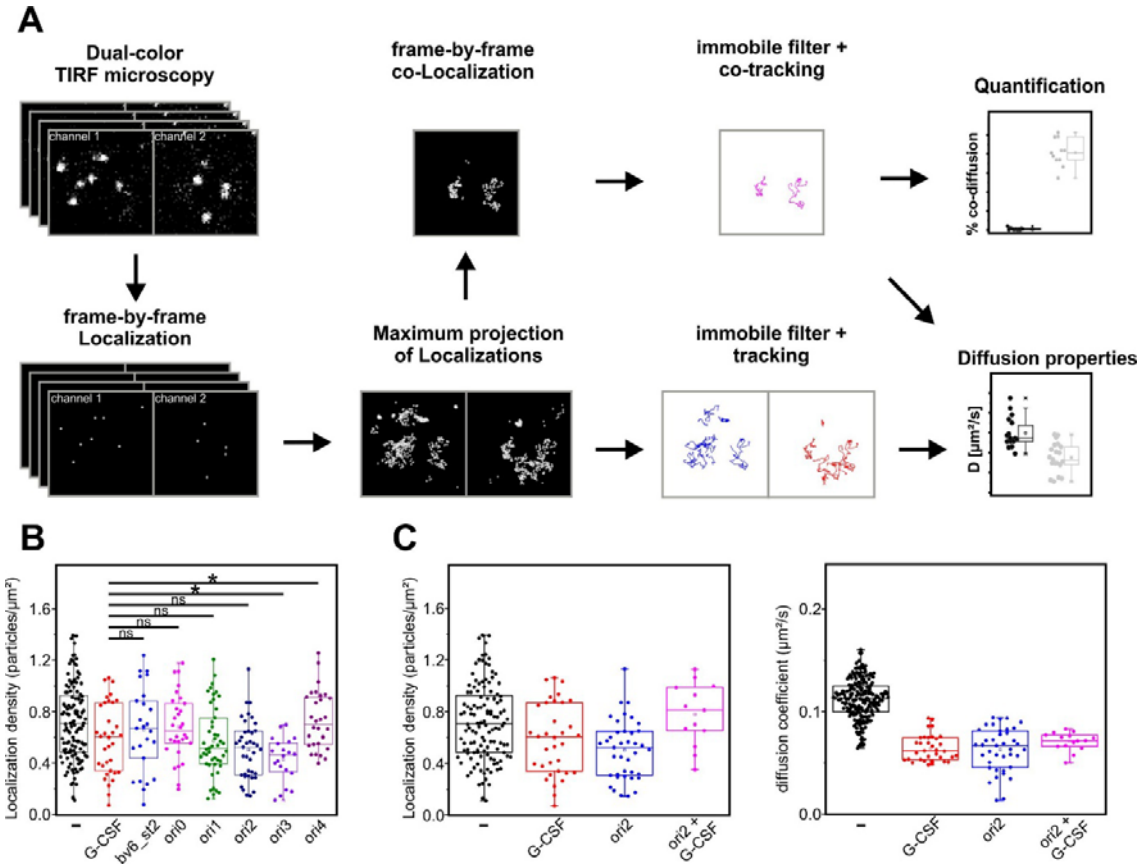

Supplementary Figure 16. The dimerization of G-CSFR was analyzed with single molecule imaging for G-CSF and the design agonists. **(A)** Workflow used for single molecule tracking and co-tracking analyses. **(B, C)** Receptor density in co-tracking experiments comparing different design agonists **(B)** and the competition between G-CSF and ori2 **(C)**. **(D)** Co-diffusion constants observed in G-CSF/ori2 competition co-tracking experiments.

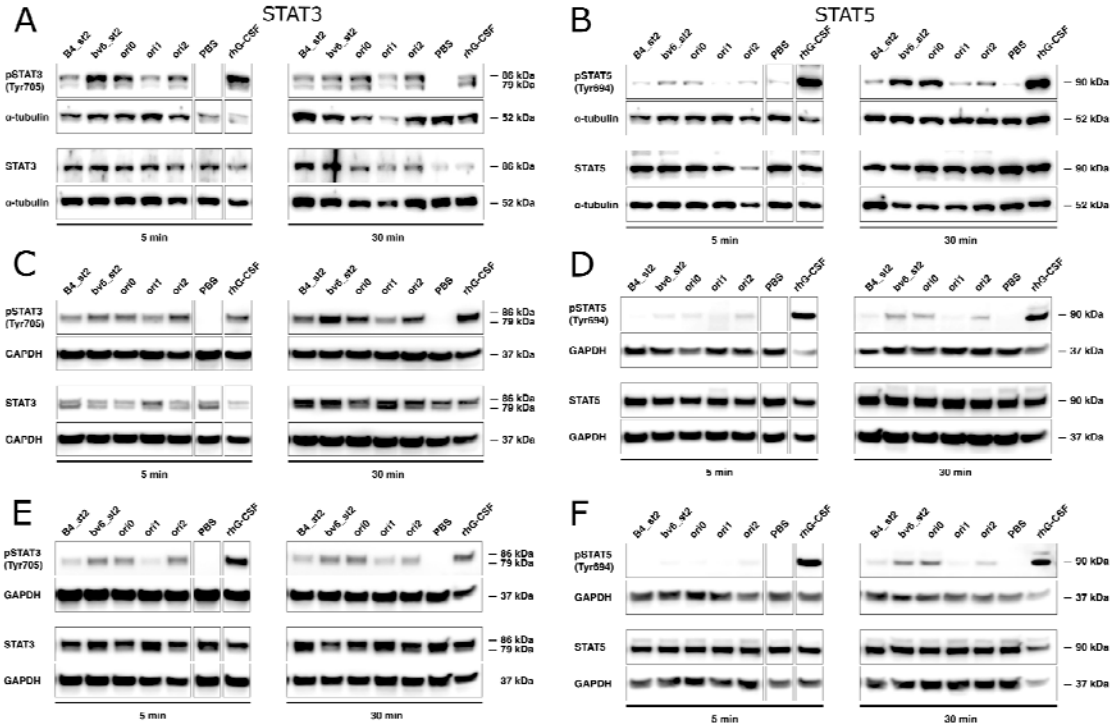

Supplementary Figure 17. (A-F) Western Blot analysis of extracts from NFS-60 cells treated with B4_st2, bv6_st2, ori0, ori1, ori2 designs, PBS, or rhG-CSF for 5 or 30 min, using phospho-STAT3 (Tyr705) (A, C, E) or phospho-STAT5 (Tyr694) (B, C, D) rabbit antibodies. As loading control, α-tubulin rabbit antibody or GAPDH rabbit antibody was used. A and B, C and D, E and F represent independent experiments.

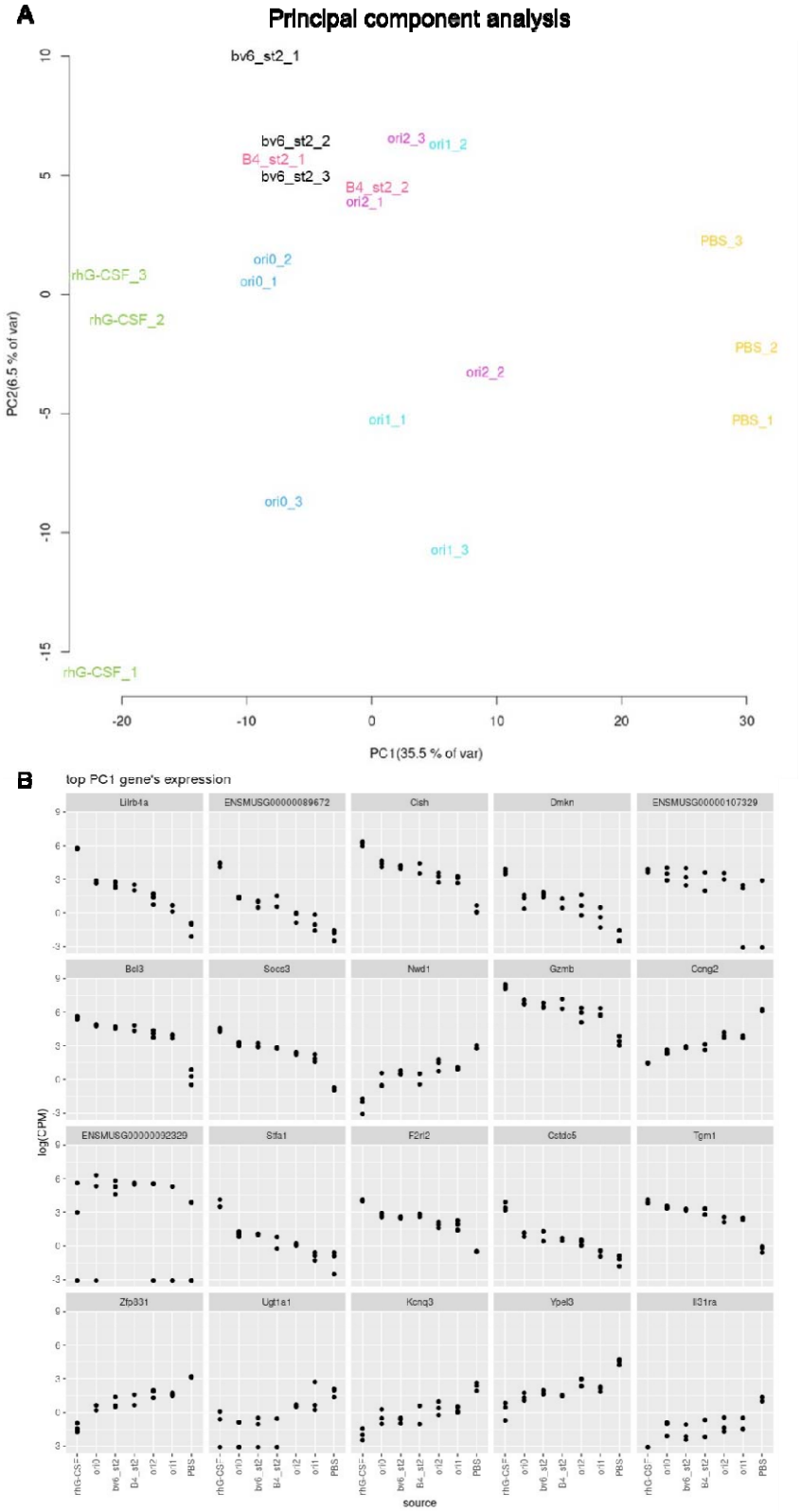

Supplementary Figure 18. (A) Principal component analysis (PCA) of groups treated with rhG-CSF, agonist designs (B4_st2, bv6_st2, ori0, ori1, ori2) or PBS and **(B)** the top 20 differentially expressed genes in PC1 of PCA.

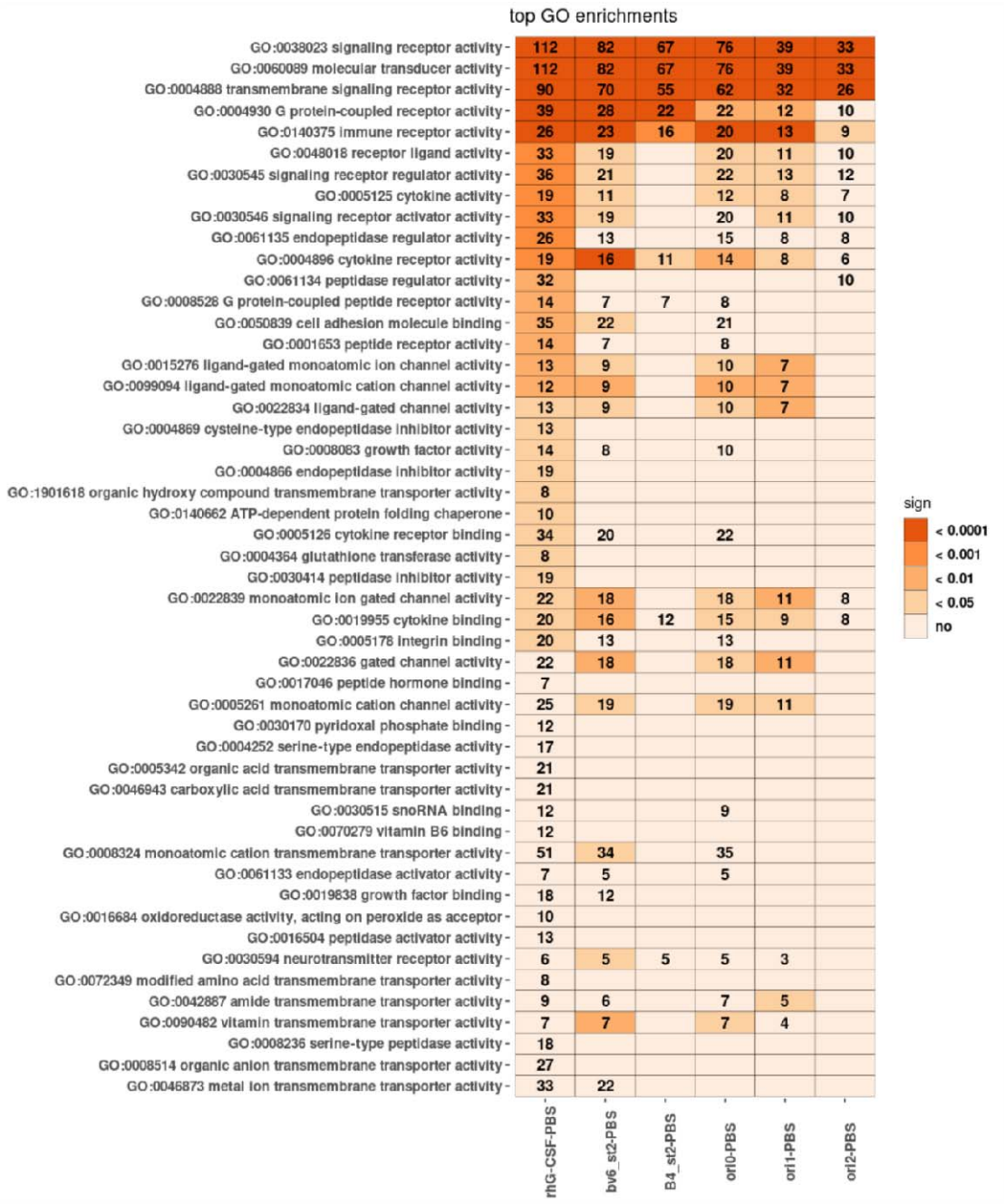

Supplementary Figure 19. Top 50 GO pathways in the groups treated with rhG-CSF or agonist designs (B4_st2, bv6_st2, ori0, ori1, ori2) compared to PBS.

Supplementary Figure 20. Top 50 MSigDB.m2 pathways in the groups treated with rhG-CSF or agonist designs (B4_st2, bv6_st2, ori0, ori1, ori2) compared to PBS.

Supplementary Tables

Supplementary Table 1. Primers used in this study.

Number	Name	Sequence
1	pN_insert_SfiI/BglI_F	gtaaggcccagccggccatggcagcactggcagcagcactggcagaaatttac
2	pN_insert_NotI_R	gtaagcggccgctgctgctgccagatgacgcaggatctg
3	B4_lib_sat_F	ggtctggatagtctgccgcagNDTtttctgNDTaaagcgctggaaVDGattcgtaaaattcaggcggacgcagcag
4	B4_lib_sat_R	ttcttccattgcctgcgccatANNANNggcaaaatctgccatatcAHNacgcagagcgtccagtgccggac
5	B4_lib_des_F1	ggtctggatagtctgccgcagNDCtttctgYNCaaagcgctggaaMWAattcgtaaaattcaggcggacgcagcag
6	B4_lib_des_F2	ggtctggatagtctgccgcagNDCtttctgYNCaaagcgctggaaRTGattcgtaaaattcaggcggacgcagcag
7	B4_lib_des_R1	ttcttccattgcctgcgccatGTYGNDggcaaaatctgccatatcTMGacgcagagcgtccagtgccggac
8	B4_lib_des_R2	ttcttccattgcctgcgccatTRWGNDggcaaaatctgccatatcTMGacgcagagcgtccagtgccggac
9	B4_lib_des_R3	ttcttccattgcctgcgccatGTYGNDggcaaaatctgccatatcGWWacgcagagcgtccagtgccggac
10	B4_lib_des_R4	ttcttccattgcctgcgccatTRWGNDggcaaaatctgccatatcGWWacgcagagcgtccagtgccggac
11	pET28_B4var_F	GGCAGCCATATGGCAGCACTGGCAGCAG
12	pET28_B4var_R	GTGGTGCTCGAGTTATGCTGCTGCCAGATGACGC
13	st2_backbone_F	taactcgagcaccaccaccaccaccactga
14	st2_backbone_R	atggctgccgcgcggcac
15	st2_fr1_F	AGCAGCGGCCTGGTGCCGCGCGGCAGCCATatggcagcactggcagcagcactggcagaaatttac
16	st2_fr1_R	GCTGGATCCGCCACCGCCtgctgctgccagatgacgcaggatctg
17	st2_fr2_F	GGCGGTGGCGGATCCAGCatggcagcactggcagcagcactggcagaaatttac
18	st2_fr2_R	TCAGTGGTGGTGGTGGTGGTGCTCGAGTTAtgctgctgccagatgacgcaggatctg
19	pN_Seq_insert_F	gaatggtcaagttgtcgac

20	pN_Seq_insert_R	Gaagaaagcgaaaggagc
21	ori1_fr1_R	CATCCAGCGCCACCAGCGTTTGCGTGCCAGATGACGCAG GATCTGG
22	ori1_fr2_F	CGCTGGTGGCGCTGGATGCTGCGCAAAGCACTGGCAGAA ATTTACAAAGGTCTGGC
23	ori2_fr1_R	TTCGCGTTTTTTTTTCATGCGTTTCGCAAAGCGACGCAGG ATCTGGTACGCTTTTTCCAG
24	ori2_fr2_F	ATGAAAAAAAAACGCGAATGGATGGCGAAAACCCTGGC AGAAATTTACAAAGGTCTGGCGGAATATC
25	ori3_fr1_R	CCATTTTTTGCGCATGCGGCGCGCCAGCTGACGCAGGATC TGGTACGCTTTTTCCAG
26	ori3_fr2_F	CGCATGCGCAAAAAATGGGCGCGCGAAATGATGGCAGCA CTGGCAGAAATTTACAAAGGTCTGG
27	ori4_fr1_R	CGCCATCATTTTGCGCATCATGCGGCGCGCCAGGCGACGC AGGATCTGGTACGCTTTTTCCAG
28	ori4_fr2_F	ATGCGCAAAATGATGGCGGAACGCATGGCGCGCGCACTG GCAGAAATTTACAAAGGTCTGGC
29	ori0_fr1_R	CCATTTCATCCACCACCATGCTGCCAGATGACGCAGGATC
30	ori0_fr2_F	TGGTGGTGGATGAAATGGCTGGCAGCAGCACTGGCAGAA ATTTAC

Supplementary Table 2: Composition of PCR reaction mix used for all reactions with the following specifications; for all reactions 5 ng/µL template was inputted but for the ones whose products were used for assembly reactions, 0.3 ng/mL were inputted. In the case of the use of multiple primers for the library backbone PCR, all F or R primers of each construct were mixed at a total concentration of 10 µM (e.g. 2.5 µM of primer 7 to 10 each). PCR program was used for all reactions either with 60 seconds extension time for all insert fragments or 340 seconds for all backbone fragments.

PCR reaction mix	Volume (µL)
dNTPs 10 mM each	1
Template 0.3 ng/µL or 5 ng/µL	1
Primer F 10 µM	2.5
Primer R 10 µM	2.5
5x Q5® Reaction Buffer (#B9027, NEB)	10
GC enhancer	10
Q5® High-Fidelity DNA Polymerase (#M0491S, NEB)	0.5
H_2O ad 50 µl	22.5

PCR program	Temperature (°C)	Time (s)	Cycle
Initial denaturation	98	30	1x
Denaturation	98	10	30x
Extension	72	60 or 340	
Final Extension	72	300	1x
Hold	8	-	1x

Supplementary Table 3: Sequence of the fusion protein between Intimin [45] and Boskar4 coded by pNB4 (colored) and sequences of all Boskar4 variants and designs (black) described in this study

Name	**Sequence**
Intimin$_{EHEC}$ (1-659)-E_tag-Boskar4-Myc_tag	MITHGCYTRTRHKHKLKKTLIMLSAGLGLFFYVNQNSFANGENYFKLGSDSKLLTHDSYQNRLFYTLKTGETVADLSKSQDINLSTIWSLNKHLYSSESEMMKAAPGQQIILPLKKLPFEYSALPLLGSAPLVAAGGVAGHTNKLTKMSPDVTKSNMTDDKALNYAAQQAASLGSQLQSRSLNGDYAKDTALGIAGNQASSQLQAWLQHYGTAEVNLQSGNNFDGSSLDFLLPFYDSEKMLAFGQVGARYIDSRFTANLGAGQRFFLPANMLGYNVFIDQDFSGDNTRLGIGGEYWRDYFKSSVNGYFRMSGWHESYNKKDYDERPANGFDIRFNGYLPSYPALGAKLIYEQYYGDNVALFNSDKLQSNPGAATVGVNYTPIPLVTMGIDYRHGTGNENDLLYSMQFRYQFDKSWSQQIEPQYVNELRTLSGSRYDLVQRNNNIILEYKKQDILSLNIPHDINGTEHSTQKIQLIVKSKYGLDRIVWDDSALRSQGGQIQHSGSQSAQDYQAILPAYVQGGSNIYKVTARAYDRNGNSSNNVQLTITVLSNGQVVDQVGVTDFTADKTSAKADNADTITYTATVKKNGVAQANVPVSFNIVSGTATLGANSAKTDANGKATVTLKSSTPGQVVVSAKTAEMTSALNASAVIFFDGAPVPYPDPLEPAQPAMAALAAALAEIYKGLAEYQARLKSLEGISPELGPALDALRLDMADFATTMAQAMEEGLDSLPQSFLLKALEQIRKIQADAAALREKLAATYKGNDRAAAAVEIAAQLEAFLEKAYQILRHLAAAAAAEQKLISEEDAAA
bv1	MAALAAALAEIYKGLAEYQARLKSLEGISPELGPALDALRYDMADFAYLMAQAMEEGLDSLPQLFLYKALEMIRKIQADAAALREKLAATYKGNDRAAAAVEIAAQLEAFLEKAYQILRHLAAA
bv2	MAALAAALAEIYKGLAEYQARLKSLEGISPELGPALDALRYDMADFACFMAQAMEEGLDSLPQIFLYKALEQIRKIQADAAALREKLAATYKGNDRAAAAVEIAAQLEAFLEKAYQILRHLAAA
bv3	MAALAAALAEIYKGLAEYQARLKSLEGISPELGPALDALRYDMADFAYFMAQAMEEGLDSLPQGFLHKALEQIRKIQADAAALREKLAATYKGNDRAAAAVEIAAQLEAFLEKAYQILRHLAAA
bv4	MAALAAALAEIYKGLAEYQARLKSLEGISPELGPALDALRYDMADFAYFMAQAMEEGLDSLPQIFLLKALEQIRKIQADAAALREKLAATYKGNDRAAAAVEIAAQLEAFLEKAYQILRHLAAA
bv5	MAALAAALAEIYKGLAEYQARLKSLEGISPELGPALDALRFDMADFAVFMAQAMEEGLDSLPQFFLFKALEQIRKIQADAAALREKLAATYKGNDRAAAAVEIAAQLEAFLEKAYQILRHLAAA
bv6	MAALAAALAEIYKGLAEYQARLKSLEGISPELGPALDALRYDMADFAILMAQAMEEGLDSLPQSFLRKALEMIRKIQADAAALREKLAATYKGNDRAAAAVEIAAQLEAFLEKAYQILRHLAAA
bv7	MAALAAALAEIYKGLAEYQARLKSLEGISPELGPALDALRFDMADFAYFMAQAMEEGLDSLPQSFLYKALEQIRKIQADAAALREKLAATYKGNDRAAAAVEIAAQLEAFLEKAYQILRHLAAA
bv8	MAALAAALAEIYKGLAEYQARLKSLEGISPELGPALDALRLDMADFARLMAQAMEEGLDSLPQRFLYKALEMIRKIQADAAALREKLAATYKGNDRAAAAVEIAAQLEAFLEKAYQILRHLAAA

bv9	MAALAAALAEIYKGLAEYQARLKSLEGISPELGPALDALRYDMADFAIYMAQA MEEGLDSLPQHFLLKALEQIRKIQADAAALREKLAATYKGNDRAAAAVEIAAQ LEAFLEKAYQILRHLAAA
bv10	MAALAAALAEIYKGLAEYQARLKSLEGISPELGPALDALRYDMADFAYFMAQA MEEGLDSLPQSFLLKALEQIRKIQADAAALREKLAATYKGNDRAAAAVEIAAQL EAFLEKAYQILRHLAAA
bv11	MAALAAALAEIYKGLAEYQARLKSLEGISPELGPALDALRHDMADFAYFMAQA MEEGLDSLPQGFLDKALEQIRKIQADAAALREKLAATYKGNDRAAAAVEIAAQ LEAFLEKAYQILRHLAAA
bv12	MAALAAALAEIYKGLAEYQARLKSLEGISPELGPALDALRYDMADFALFMAQA MEEGLDSLPQCFLLKALEQIRKIQADAAALREKLAATYKGNDRAAAAVEIAAQL EAFLEKAYQILRHLAAA
bv13	MAALAAALAEIYKGLAEYQARLKSLEGISPELGPALDALRLDMADFAFFMAQA MEEGLDSLPQSFLYKALEQIRKIQADAAALREKLAATYKGNDRAAAAVEIAAQL EAFLEKAYQILRHLAAA
bv14	MAALAAALAEIYKGLAEYQARLKSLEGISPELGPALDALRYDMADFAFNMAQA MEEGLDSLPQGFLYKALEQIRKIQADAAALREKLAATYKGNDRAAAAVEIAAQ LEAFLEKAYQILRHLAAA
bv15	MAALAAALAEIYKGLAEYQARLKSLEGISPELGPALDALRYDMADFAYNMAQA MEEGLDSLPQHFLLKALEMIRKIQADAAALREKLAATYKGNDRAAAAVEIAAQ LEAFLEKAYQILRHLAAA
bv16	MAALAAALAEIYKGLAEYQARLKSLEGISPELGPALDALRLDMADFATNMAQA MEEGLDSLPQFFLYKALEMIRKIQADAAALREKLAATYKGNDRAAAAVEIAAQ LEAFLEKAYQILRHLAAA
bv1_st2	MAALAAALAEIYKGLAEYQARLKSLEGISPELGPALDALRYDMADFAYLMAQA MEEGLDSLPQLFLYKALEMIRKIQADAAALREKLAATYKGNDRAAAAVEIAAQ LEAFLEKAYQILRHLAAAGGGGSSMAALAAALAEIYKGLAEYQARLKSLEGISP ELGPALDALRYDMADFAYLMAQAMEEGLDSLPQLFLYKALEMIRKIQADAAAL REKLAATYKGNDRAAAAVEIAAQLEAFLEKAYQILRHLAAA
bv2_st2	MAALAAALAEIYKGLAEYQARLKSLEGISPELGPALDALRYDMADFACFMAQA MEEGLDSLPQIFLYKALEQIRKIQADAAALREKLAATYKGNDRAAAAVEIAAQL EAFLEKAYQILRHLAAAGGGGSSMAALAAALAEIYKGLAEYQARLKSLEGISPE LGPALDALRYDMADFACFMAQAMEEGLDSLPQIFLYKALEQIRKIQADAAALR EKLAATYKGNDRAAAAVEIAAQLEAFLEKAYQILRHLAAA
bv6_st2	MAALAAALAEIYKGLAEYQARLKSLEGISPELGPALDALRYDMADFAILMAQA MEEGLDSLPQSFLRKALEMIRKIQADAAALREKLAATYKGNDRAAAAVEIAAQ LEAFLEKAYQILRHLAAAGGGGSSMAALAAALAEIYKGLAEYQARLKSLEGISP ELGPALDALRYDMADFAILMAQAMEEGLDSLPQSFLRKALEMIRKIQADAAAL REKLAATYKGNDRAAAAVEIAAQLEAFLEKAYQILRHLAAA
bv8_st2	MAALAAALAEIYKGLAEYQARLKSLEGISPELGPALDALRLDMADFARLMAQA MEEGLDSLPQRFLYKALEMIRKIQADAAALREKLAATYKGNDRAAAAVEIAAQ LEAFLEKAYQILRHLAAAGGGGSSMAALAAALAEIYKGLAEYQARLKSLEGISP ELGPALDALRLDMADFARLMAQAMEEGLDSLPQRFLYKALEMIRKIQADAAAL

	REKLAATYKGNDRAAAAVEIAAQLEAFLEKAYQILRHLAAA
bv15_st2	MAALAAALAEIYKGLAEYQARLKSLEGISPELGPALDALRYDMADFAYNMAQA MEEGLDSLPQHFLLKALEMIRKIQADAAALREKLAATYKGNDRAAAAVEIAAQ LEAFLEKAYQILRHLAAAGGGGSSMAALAAALAEIYKGLAEYQARLKSLEGISP ELGPALDALRYDMADFAYNMAQAMEEGLDSLPQHFLLKALEMIRKIQADAAA LREKLAATYKGNDRAAAAVEIAAQLEAFLEKAYQILRHLAAA
bv16_st2	MAALAAALAEIYKGLAEYQARLKSLEGISPELGPALDALRLDMADFATNMAQA MEEGLDSLPQFFLYKALEMIRKIQADAAALREKLAATYKGNDRAAAAVEIAAQ LEAFLEKAYQILRHLAAAGGGGSSMAALAAALAEIYKGLAEYQARLKSLEGISP ELGPALDALRLDMADFATNMAQAMEEGLDSLPQFFLYKALEMIRKIQADAAAL REKLAATYKGNDRAAAAVEIAAQLEAFLEKAYQILRHLAAA
ori1	MAALAAALAEIYKGLAEYQARLKSLEGISPELGPALDALRYDMADFAILMAQA MEEGLDSLPQSFLRKALEMIRKIQADAAALREKLAATYKGNDRAAAAVEIAAQ LEAFLEKAYQILRHLARKRWWRWMLRKALAEIYKGLAEYQARLKSLEGISPEL GPALDALRYDMADFAILMAQAMEEGLDSLPQSFLRKALEMIRKIQADAAALRE KLAATYKGNDRAAAAVEIAAQLEAFLEKAYQILRHLAAA
ori2	MAALAAALAEIYKGLAEYQARLKSLEGISPELGPALDALRYDMADFAILMAQA MEEGLDSLPQSFLRKALEMIRKIQADAAALREKLAATYKGNDRAAAAVEIAAQ LEAFLEKAYQILRRFAKRMKKKREWMAKTLAEIYKGLAEYQARLKSLEGISPEL GPALDALRYDMADFAILMAQAMEEGLDSLPQSFLRKALEMIRKIQADAAALRE KLAATYKGNDRAAAAVEIAAQLEAFLEKAYQILRHLAAA
ori3	MAALAAALAEIYKGLAEYQARLKSLEGISPELGPALDALRYDMADFAILMAQA MEEGLDSLPQSFLRKALEMIRKIQADAAALREKLAATYKGNDRAAAAVEIAAQ LEAFLEKAYQILRQLARRMRKKWAREMMAALAEIYKGLAEYQARLKSLEGISP ELGPALDALRYDMADFAILMAQAMEEGLDSLPQSFLRKALEMIRKIQADAAAL REKLAATYKGNDRAAAAVEIAAQLEAFLEKAYQILRHLAAA
ori4	MAALAAALAEIYKGLAEYQARLKSLEGISPELGPALDALRYDMADFAILMAQA MEEGLDSLPQSFLRKALEMIRKIQADAAALREKLAATYKGNDRAAAAVEIAAQ LEAFLEKAYQILRRLARRMMRKMMAERMARALAEIYKGLAEYQARLKSLEGIS PELGPALDALRYDMADFAILMAQAMEEGLDSLPQSFLRKALEMIRKIQADAAAL REKLAATYKGNDRAAAAVEIAAQLEAFLEKAYQILRHLAAA
ori0	MAALAAALAEIYKGLAEYQARLKSLEGISPELGPALDALRLDMADFATTMAQA MEEGLDSLPQSFLLKALEQIRKIQADAAALREKLAATYKGNDRAAAAVEIAAQL EAFLEKAYQILRHLAAWWWMKWLAAALAEIYKGLAEYQARLKSLEGISPELGP ALDALRLDMADFATTMAQAMEEGLDSLPQSFLLKALEQIRKIQADAAALREKL AATYKGNDRAAAAVEIAAQLEAFLEKAYQILRHLAAA

Supplementary Methods

Damietta specifications for the design of orientation-rigging ligands

Example Damietta specifications for weights, sample parameters, the mutable residues, and repackable residues for designing the rigid linker helix region of ori0 (compare Material and Methods, Design of orientation-rigging ligands):

```
# mutational targets
mut_res 124 ADEFHIKLMNQRSTVWY
mut_res 125 ADEFHIKLMNQRSTVWY
mut_res 126 ADEFHIKLMNQRSTVWY
mut_res 127 ADEFHIKLMNQRSTVWY
mut_res 128 KREQ
mut_res 129 ADEFHIKLMNQRSTVWY

# repacking targets
rpk_res 61
rpk_res 63
rpk_res 66
rpk_res 119
rpk_res 120
rpk_res 121
rpk_res 122
rpk_res 123
rpk_res 130
rpk_res 131
rpk_res 132
rpk_res 133
rpk_res 134
rpk_res 184
rpk_res 185
rpk_res 247
rpk_res 250

# sampling parameters (optional)
scramble_order        1 # default:= 0
m_mutations                 3 # default:= 3
n_paths                     7 # default:= 1
n_iters                     5 # default:= 1

# mutagenesis scoring weights (optional)
mut_max_lj                  25.0
mut_w_pp              1.0
mut_w_k               0.0
mut_w_lj              1.0
mut_w_solv                  1.0
mut_w_elec                  0.125

# repacking scoring weights (optional)
rpk_max_lj            25.0
rpk_w_pp        1.0
rpk_w_k         1.0
rpk_w_lj        1.0
rpk_w_solv            1.0
rpk_w_elec            0.125
```